Hydrodynamic effects of morphology and schooling interactions for improved performance in fish-like swimmers

---

A Dissertation

Presented to

the faculty of the School of Engineering and Applied Science

University of Virginia

In Partial Fulfillment

of the requirements for the Degree

Doctor of Philosophy in Mechanical and Aerospace Engineering

By

John Kelly

December 2024

APPROVAL SHEET

The dissertation is submitted in partial fulfillment of the
requirements for the degree of
Doctor of Philosophy

_____
John Kelly, Author

This thesis has been read and approved by the examining Committee:

_____
Haibo Dong, Advisor

_____
Frank Lagor, Committee Chair

_____
Qing Chang, Committee Member

_____
Daniel Quinn, Committee Member

_____
Matthew Reidenbach, Committee Member

Accepted for the School of Engineering and Applied Science:

_____
Jennifer L. West, Dean
School of Engineering and Applied Science

December 2024

Abstract

Fish have evolved the ability to swim with high speed, efficiency, and maneuverability and have developed specialized locomotion strategies to most efficiently interact with the surrounding fluid environment. They also leverage collective behavior via schooling to allow for better hydrodynamic performance. The undulatory motion, irregular morphologies, and strong hydrodynamic interactions from schooling create a complex fluid environment where high performance can be achieved. This research is a systematic study of large schooling effects and morphology in fish and fish-like robots. A Cartesian grid-based immersed boundary incompressible Navier-Stokes solver is used to simulate the unsteady flow around fish-like swimmers.

The study begins by evaluating a 2D swimmer in planar arrangements of large, dense fish schools. A comparison of the arrangements concludes that diamond schools balance the higher thrust benefits from longer schools with the power savings from wider schools and allow for a high-performance school with more evenly distributed performance benefits. Additionally, within the context of these dense schools, synchronous motion between fish allows for the most constructive body-body pressure interactions

throughout the school and maximizes performance gained from schooling. Classification of individual fish within the school persists as a performance and interaction predictor through each arrangement and size of the school.

Interactions between multiple schools of fish are also studied. This is done via numerical simulations of multiple diamond fish schools swimming in line. The wake interaction provides a significant opportunity for performance benefits in the follower subschool but can also be a detriment with different vortex interactions resulting from altered spacing between subschools.

Finally, morphological effects in schools of undulating swimmers are studied. Simulations begin with a single tuna-inspired robotic platform swimming. Propulsor cross-sectional shape, body thickness, kinematic effects, and median fin design are varied. Next, more fundamental shape parameters are varied using a class shape transformation method to generate undulating body shapes in both 2D and 3D. The impact of body shape is observed in single and schooled swimmers. This study shows that variations in body shape, particularly in the posterior region of the body, have a significant impact on the performance of solo and schooling swimmers.

The primary contributions of this dissertation are in the characterization of large fish schools, including the classification of individuals, characterization of performance-enhancing mechanisms of interaction, understanding of arrangements for high performance, and morphological impacts on schooling interactions. The findings from this

work will bring new insights into the future design of bio-inspired unmanned under-water vehicles.

To Madeline: for her unwavering love and support of my goals

Acknowledgements

I would first like to thank my advisor, Dr. Haibo Dong, for his guidance and support throughout my doctoral studies. He taught me not only how to conduct impactful research, but also how to connect with the scientific community and effectively communicate my research. Next, I would like to thank my committee members for their inspiring guidance, encouragement, and constructive comments on my research. I would also like to thank all of the MURI team members for their questions, feedback, and insights into the field that inspired much of my work. I would like to thank the current and past members of FSRG including Alec Menzer, Jiacheng Guo, Zihao Huang, Dr. Yuchen Gong, Dr. Yu Pan, Dr. Junshi Wang, Dr. Pan Han, Dr. Wei Zhang, and all former members of FSRG for their advice, technical advancements, and examples set by their own research that made this work possible. I would especially like to thank Dr. Yu Pan, whose insights and mentorship have been critical to my growth as a researcher. I want to thank the many undergraduates who have joined our lab and assisted with this research, including Jackson Wray, Harrison Bobbit, and Genevieve Forrer. I am very grateful to the many people who supported me outside of research, especially my parents, grandparents, and siblings who instilled in me curiosity and the confidence that I can achieve anything I set my mind to from a young age. Finally, thank you to

my fiancée Madeline, who has supported me immensely as I pursue my goals.

This work was supported by the Office of Naval Research MURI N00014-14-1-0533, MURI N00014-15-1-2234, STTR SRA00001652, National Science Foundation CNS-1931929 and National Research Traineeship. I would also like to thank the University of Virginia Research Computing Group for the availability of the Rivanna supercomputing cluster.

Contents

List of Figures

List of Tables

1 Introduction

1.1 Motivation

Fish have evolved the ability to swim with high speed, efficiency, and maneuverability over hundreds of millions of years, and have developed specialized locomotion strategies to most efficiently interact with the surrounding fluid environment. In addition to their impressive individual performance, fish also leverage collective behavior via schooling. This allows better predator avoidance [1], reproductive opportunities [2], higher foraging efficiency [3], and hydrodynamic speed and efficiency [4].

These high-performing natural swimmers are of particular interest in the design of underwater robotics. For example, the propulsive efficiency of a standard marine propeller is around 70%, whereas a pitching and heaving citation fluke can reach over 90% [8]. Underwater robotics occupy a large span of applications, including surveillance, search and rescue, and environmental monitoring. Bio-inspired underwater robots allow for more maneuverability, efficiency, and a decreased impact on the local environment during these missions. To that end, research focus has been given to the

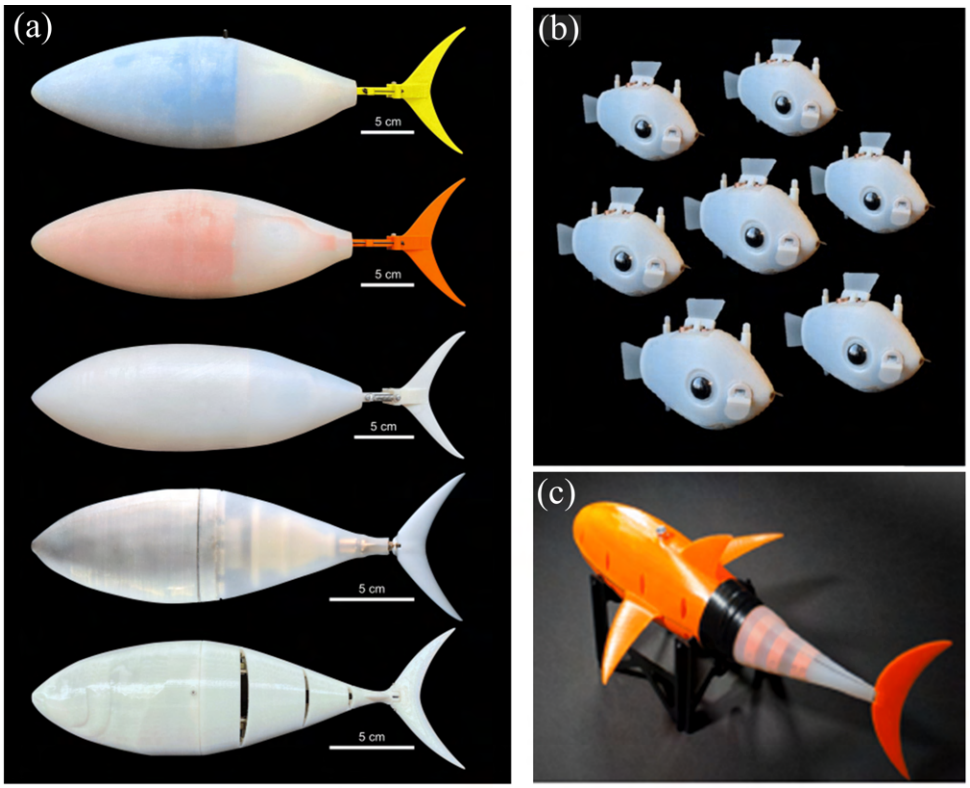

FIGURE 1.1: Fish-inspired underwater robots. (a) Multiple generations of Tunabot, UVA [5], (b) Blueswarm, Harvard [6], (c) OpenFish, Delft U. [7].

hydrodynamics of these performance gaps and understanding how biological swimmers can achieve such high performance while remaining agile. Significant progress has been made in optimizing these vehicles for both speed and efficiency [9]–[12], but a performance gap still exists between biological swimmers and their robotic counterparts. Some of these gaps have been closed via replicating features like morphology and kinematics of fish swimming as shown in Fig. 1.1. However, these platforms are still significantly behind their biological counterparts, and many features are still missing. Another difficulty in learning the flow physics of fish swimming from nature comes from the vast range of key parameters such as morphology demonstrated by

biological swimmers, as shown in Fig. 1.2. Elucidating what is important for high performance from biological examples is very difficult, as the biological realm occupies a large range of morphologies, and not all evolutionary traits can be attributed to purely hydrodynamic performance. This necessitates further research into the morphological effects of fish and fish-like swimming. While some investigations have been previously published, a thorough understanding of body shape effects in a solo swimmer is yet to be reached.

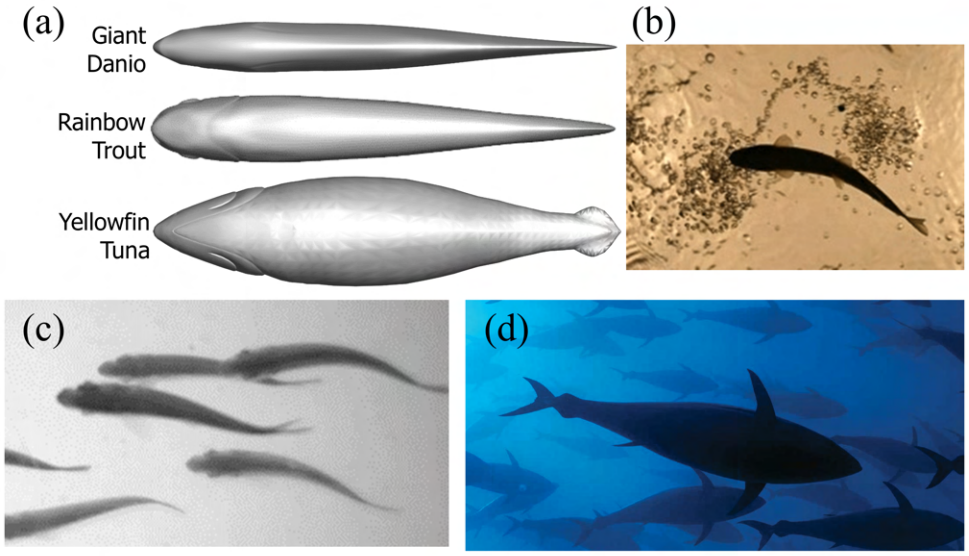

FIGURE 1.2: Reconstructed model (a) and image of the body of giant Danio (c) [13], rainbow trout (b) [13], Yellowfin Tuna (d) [14].

Additionally, the ability to school is significantly lacking from most of these platforms. Despite recent progress on fish-inspired underwater robot swarms [6], there is no involvement of hydrodynamics, and the beneficial hydrodynamic interactions leveraged by real fish are not present in their robotic counterparts. This is due to the high complexity of multiple unsteady bodies interacting in a flow coupled with a limited understanding of how interactions can be made beneficial to the robotic platform. The

unsteady nature of a fish undulating its entire body, compared to a traditional rigid oceanic vessel, provides complicated flow physics alone. Adding in the interaction between many bodies independently interacting within the flow significantly increases the complexity of the flow. Some efforts have been made to understand the physics of schooling fish, however, these investigations are limited to two categories. First, studies frequently utilize only two fish as a representative of an entire fish school, even though fish schools can number into the millions. Second, simplified models use lower-order methods to approximate interactions, rather than directly observing the fluid interactions and vortex dynamics. Very few studies extend beyond a basic four-fish structure when studying fluid dynamics in a school. Additionally, results from Kelly et al. [15] have shown that increasing the school size beyond four-fish yields previously unexplored physics that is not accounted for in the simplified four-fish models. Directly studying larger schools is essential for a full understanding of fish school hydrodynamics.

Finally, no significant attention has been given to how body shape affects the interactions within a fish school. For fish-like robotics, body shape selection may play a critical role in the physics of interactions. A better understanding of how body shape affects these interactions is important to best leverage the flow physics of schooling interactions.

1.2 Hydrodynamics of Fish Swimming

In order to achieve high-efficiency swimming, fish take advantage of unsteady hydrodynamics with their body and fins. They undulate and pass a traveling wave from their head to their caudal fin. As the traveling wave passes the the amplitude increases, culminating at the caudal fin where most of the thrust production occurs [16]. The body's motion accelerates the surrounding flow, contributing to the propulsion. The caudal fin of the fish acts as a flapping foil, taking advantage of lift-based propulsion. The fish then accelerates forward, leaving behind a structured wake. Numerical [17] and particle image velocimetry (PIV) [18] studies have shown that a single fish swimming produces a von Karman vortex street. In three dimensions, this often appears as interconnected vortex rings, with a slice through the center representing a von Karman street and the tip vortices from the caudal fin closing the structure into distinct rings. This wake is demonstrated in 2D and 3D in Fig. 1.3. The caudal fin leading edge vortex, which has proven to be critical in the flapping flight of insects and birds [19], [20], has also been shown to be critical to fish thrust generation at the caudal fin in swimming [21] and schooling [22]. This allows study of the thrust production to be completed using a model of only the caudal fin.

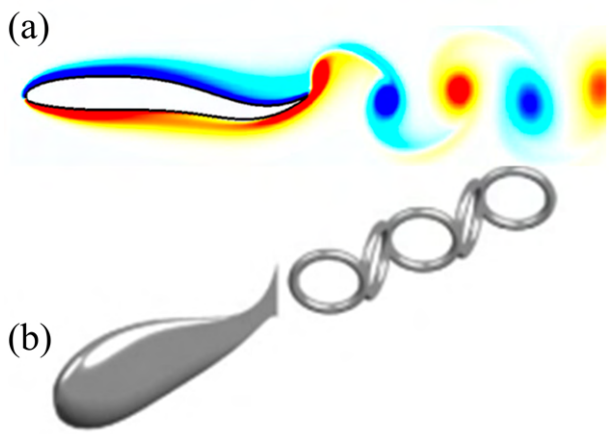

FIGURE 1.3: (a) von Karman street behind a 2-dimensional undulating swimmer, reproduced from Pan and Dong [23]. (b) Interconnected vortex rings behind a 3-dimensional fish-like swimmer, reproduced from Muller et al. [24]

1.3 Fish Schooling Hydrodynamics

Fish schooling has been proven to serve many functions for individual fish, including improved predator defense, reproductive success, socialization, and hydrodynamic benefits [25]–[27]. Recent studies using oxygen consumption and tail-beat frequency metrics have proven that individuals gain significant energy conservation from schooling interactions [28]–[30]. As engineers, we are most interested in the hydrodynamics interactions that allow these large energy savings, and replicating them in unmanned underwater vehicles. To understand fish schooling from a hydrodynamics perspective, many studies have utilized two-fish systems, employing two-dimensional (2D) computational simulations and experiments to investigate energetic, thrust, and stability benefits in flags [31], flapping foils [32]–[39] and undulating foils [40]–[46]. Utilizing side-by-side, in-line, and staggered arrangements, some mechanisms for hydrodynamic benefit from schooling were uncovered. In flapping foils, Broering et

al. [33] showed that a large thrust benefit is gained by the upstream foil when two foils are flapping in-line. Enhancements to the downstream foil efficiency and thrust were also observed for some spacing and phase combinations in multiple studies [34], [35]. In undulating foils, hydrodynamics and wake classification of two fish swimming side-by-side were investigated by Dong et al. [40], showing that in-phase swimming provided power saving for the system, while anti-phase swimming enhanced the forward forces generated. Maertens et al. [46] show that hydrodynamic benefits can be achieved via interaction with incident vortices from upstream fish. Khalid et al. [43] found that in-line swimming led to an enhancement in performance for the upstream fish due to wake splitting by the rear fish increasing the pressure behind the upstream fish. A drafting effect benefiting the trailing fish is also observed for some conditions. These two fish studies establish some of the hydrodynamic fish-fish interactions, in addition to unique performance for leader and follower fish. However, significant progress is still required to understand hydrodynamics within larger fish schools.

Significant work has been done in extending two-fish fluids studies into larger schools using more robust fluids models, including infinite school approximations [47]–[50] and multiple fish models [15], [23], [51]–[57]. Saadt et al. simulated an approximation for infinite foils utilizing a periodic boundary condition at the inlet, finding that hydrodynamic benefits of schooling in-line come from leading-edge suction on the trailing foil and added-mass push on the leading foil [47]. While valuable for sparse schools, the infinite school approximation prevents close proximity of the fish due to the boundary condition set up, requiring more fish in a single domain to observe larger

dense schools. Lin et al. [55] and Peng et al. [56] found stability in self propelled foils in dense arrangements. Becker et al. [50] and Park and Sung [57] show that interactions with the vortex wake from previous fish can enhance performance in subsequent fish within a school. In Dai et al., numerical simulations of 2D fish were leveraged to investigate energetics in schools with two, three, and four fish [51]. Their results suggest that more compact arrangements achieve a lower cost of transport. Additionally, Pan and Dong investigated spacing and phase in a diamond school arrangement [23], [52]. They found that the dense diamond school maximized interaction between fish and attributed hydrodynamic benefits from schooling to a block effect, wall effect, body-body suction, and vortex capturing. They also identified distinct interactions for the front, edge, and back fish, with both edge fish in the diamond behaving similarly.

Hydrodynamic interaction in large fish schools has received limited attention in literature, however, some progress in understanding has been made using lower-order models of a large number of fish in a school [58], [59]. Gazzola et al. utilized a coupled reinforcement learning optimization of control of fish in large schools with a finite-width dipole method to model the interactions between swimmers [58]. Their work evaluated various arrangements of 100 swimmers, concluding that elongated school shapes allow for drafting and pushing to occur, improving the school's performance. It was also found that densely packed swimmers within the school gave the best opportunity to leverage interactions for performance benefit. Filella et al. published work that similarly uses a dipole method to approximate hydrodynamics for schools

of 100 swimmers. They concluded that individuals in the school reached higher swimming speeds when including hydrodynamic interactions with the fish around it in the school [59]. These studies provide valuable groundwork for understanding larger fish schools, however, the dipole method used in these studies is low fidelity and more work is needed to understand the details of flow interactions for the hydrodynamic benefits of schooling to be fully leveraged.

In addition to typical fish school models, some biologists have demonstrated that fish do not act as one large school. In this work, they have uncovered that fish in a larger school tend to act as smaller subgroups, behaving and moving similarly to the fish within their subgroup but often varying across the larger school as a whole [60]–[62]. These formations have never been studied from a hydrodynamics perspective, but a few insights can be gained from understanding them further. Schools swimming through fully turbulent flow have been shown to gain added benefits from schooling compared to a solo swimmer [63] by acting as a filter for the later fish in the school to experience a more structured flow. A fish school interacting with a complex structured wake, rather than turbulent flow, has not been studied previously. Additionally, subgroups offer a much simpler model for the control of large systems of fish-like robotics. If the hydrodynamic interactions allow similar benefits to a single larger school, swimming in multiple smaller subgroups can provide an attractive option for robotic swam control.

1.4 Morphological Effects in Fish-like Swimmers

In flapping airfoil studies, the shape of the foil has been shown to be a significant parameter to consider. Previous studies have been conducted investigating the foil thickness effect in flapping foils [64]–[70]. In each of these studies, which occur over a range of methodologies and Reynolds number regimes, changes in the foil shape are shown to have a significant impact on the performance of the foil in a flapping motion. Furthermore, the wake produced by the foil during flapping is shown to change as the shape changes.

Similar studies have been conducted in undulating swimmers, also concluding that body shape is a significant factor in solo swimmer performance [71]–[75]. In addition to performance changes, an alteration in the wake produced for a single swimmer is found, and it is predicted that body shape will also be an important parameter in schooling.

Biological inspiration of schooling fish offers little conclusive insight into the topic. Schooling swimmers take a large variety of body shapes [25], making it difficult to draw conclusions about the best body shape for optimal interactions that can be used for unmanned underwater robot swarms. Additionally, the current body of schooling literature proposes many interaction mechanisms via studies of arrangement, phase, and kinematics. However, these studies all utilize a large range of body shapes, including thin filaments [Cong 2019], hydrofoils [76], NACA0012 [77], NACA0015 [38],

and NACA0020 [78] as well as the more biological-based giant danio [79], [80], zebrafish [81], tuna [82] and mackerel [22] body shapes. Despite this, no focus of these investigations has been on the effect of body shape on schooling interactions. Each one has built upon the previous, but this body of literature lacks considerations of how body shape may impact a comparison of their results.

To further explore hydrodynamics in schooling interactions, it is essential to understand the effects that body shape has on performance and wake generation within a school. Determining the influence of body shape is critical to reaching a more unified view of schooling hydrodynamics, and offers insight for the design of unmanned underwater vehicles.

1.5 Objectives

To further understand hydrodynamics in fish like swimmers, the roles of morphology and schooling, and the opportunities they give to future robotic platforms, more fundamental research questions need to be addressed. This thesis aims to systematically study these problems, and sets out to answer the following questions:

1. What are the hydrodynamic mechanisms of interaction within large fish schools, and how do they change based on the arrangement of these schools? Is there a general rule for the best arrangements for an increased school size? Do the classifications shown in elongated schools still apply to other arrangements of schools?

2. Do fish gain benefits via interactions between dense subgroups? Are they sensitive to particular spacing between groups? Is this a viable option for robotic control to still gain most of the benefits of a larger school?

3. What about biorobotic fish platforms? How do typical biological swimmer parameters alter their performance? Are their parameters that can be easily adjusted in the robotic setting for enhanced performance?

4. How does the body shape impact hydrodynamics within a fish school? Are benefits from schooling gained or lost by altering body shape? How do three-dimensional effects play a role?

The above questions are explored using comprehensive two-dimensional and three-dimensional high-fidelity numerical simulations. Fish motion is modeled after carangiform swimmers and robotic fish motion is reconstructed directly from videos of the robot swimming. A class shape transformation shape method for foils forms the basis for multiple methods of controlling body shape in propulsors, two-dimensional undulating swimmers, and three-dimensional undulating swimmers. The performance and hydrodynamics will be analyzed to uncover underlying mechanisms.

Objective 1: Study the effects of swimming in large fish schools

To study the effects of swimming in large schools, two-dimensional undulating swimmer models using a standard NACA foil controlled by traveling wave kinematics are

used. This study compares increasing school size via longer, wider, and balanced diamond schools up to 25 fish. The effects of a phase stagger are also studied within the 25 fish schools. The resulting performance and hydrodynamics are analyzed in detail to uncover fundamental flow mechanisms present in the large school.

In addition to the dense school arrangements, the impact of subschooling is studied via similar swimmer models. Two base units of a dense diamond school are set up to interact in-line and the spacing between them is varied. The lateral spacing of the back subgroup is also varied to capture the wake from the front group. The simulation results are analyzed for performance and fundamental flow mechanisms that bring insight to the multi-subschool system.

Objective 2: Study morphological effects of bio-robotic swimming

This research utilizes a high-speed video reconstruction method to virtually recreate the motion from the Tunabot Flex platform. A 3D skeleton-based reconstruction provides a platform for altering body shape and kinematics for simulation while maintaining true robotic-like motion. Body shape, maximum body joint angles, and the presence and design of median fins are studied to assess the impact on biorobotic swimming, investigating the feasibility of improvements to the platform while uncovering fundamental flow mechanisms directly pertinent to improving the robotic design. Additional investigations into the cross-sectional shapes of the propulsor are completed using a 2D model of flapping foil, varying foil shape parameters.

Objective 3: Investigate the impacts of body shape on schooling swimmers

To study the effects of body shape in schools, two-dimensional body shapes are constructed using a class-shape transformation method that allows for independent altering of fundamental foil shape parameters. This varies the maximum thickness, maximum thickness location, boattail angle, and leading-edge radius of foils that are then prescribed by traveling wave equations in a diamond school. Performance and flow are closely analyzed to uncover fundamental mechanisms that are altered by the changing body shapes.

Additionally, the three-dimensional effects are studied. To achieve this, the class shape transformation methodology is extended to three dimensions by adding both top and side foil profiles that can be altered. A biological study is completed by digitizing available fish CT scan data to determine the range of parameters needed for the study. Finally, each parameter is varied in separate cases, and undulation kinematics are applied. The resulting swimmers are studied in solo swimming and staggered swimming arrangements, and the underlying flow mechanisms changed by the body shape are studied.

1.6 Outline of Chapters

To understand the impacts of morphology and large schooling arrangements on the hydrodynamics and performance in fish like swimmers and robots, this dissertation presents numerical simulations of fish-like and fish-robot-like models. The organization of the thesis is as follows:

Chapter 2 outlines the numerical simulation methodology utilized in this work. Section 2.1 details the immersed boundary method-based flow solver and local mesh refinement blocks used in the simulations. Section 2.2 describes the calculation of forces and force coefficients. Section 2.3 presents validation studies where the forces and flow generated from the solver are compared with experimental results, validating the use of the solver for multiple bodies interacting in an unsteady flow environment at similar Reynolds numbers.

Chapter 3 presents numerical simulations of 4-25 fish schools, exploring the impact of increasing school size via increasing the length of the school, width of the school, or maintaining a diamond formation. The methodology for school arrangements and undulation motion is presented in section 3.1.1. Section 3.1.2 details the grid and setup of the flow simulation. The results are presented in 3.1.3, and the discussion of the results and underlying hydrodynamic mechanisms in 3.1.4. Finally, a brief summary of the section is provided in 3.1.5. The results of this chapter form the basis for the following publications:

- **J Kelly**, Y Pan, A Menzer, H Dong (2023) "Hydrodynamics of body-body interactions in dense synchronous elongated fish schools," Physics of Fluids 35(4), 041906

- **J Kelly**, H Dong, "Large planar fish school arrangements for enhanced hydrodynamic performance." (**under preparation**) Target: Journal of Fluids and Structures

Chapter 4 investigates the effects of schooling via multiple subgroups of swimmers from a hydrodynamic perspective. Section 4.1 presents the arrangement of the dense diamond-based subgroups and parameters G and D used throughout the study. Section 4.2 details the setup for the numerical simulations. Section 4.3 presents the results for subschooling hydrodynamics and details the wake capture by observing changes with parameters G and D. Finally, a brief summary of the section is provided in section 4.4. The results of this chapter form the basis for the following publications:

- **J Kelly**, Y Pan, H Dong (2023) "Wake interactions between groups of undulating foils," AIAA SCITECH 2023 Forum, 2292.

- **J Kelly**, H Bobbit, H Dong, "Planar interactions between subgroups of diamond fish schools." (**under preparation**) Target: Physical Review Fluids

Chapter 5 details the results of a numerical study on the hydrodynamics and performance in the Tunabot Flex through different body sizes, maximum joint angles, and median fin designs, and the propulsor. Section 5.1 details the cross sectional propulsor morphology study completed with a flapping foil model. The class shape transformation method used in the study to vary foil shapes with a few parameters in presented in section 5.1.1, along with the kinematics for the flapping motion. Section 5.1.2 details the setup of the simulations. The numerical results and hydrodynamics mechanisms are presented in section 5.1.3. Finally, a brief summary of the section is provided in section 5.1.4. The results of the reconstructed Tunabot motion with morphological and kinematic parameter changes are presented in section 5.2. Section 5.2.1 details

the reconstruction method used to virtual replicate the Tunabot motion, as well as the parameters changed in the study. Section 5.2.2 details the setup for the simulations. Section 5.2.3 presents the results and analysis of each study. Finally, a brief summary of the section is provided in section 5.2.4 The results of this section form the basis for the following publications:

- **J Kelly**, M Khalid, P Han, H Dong (2023) "Geometric Characteristics of Flapping Foils for Enhanced Propulsive Efficiency," Journal of Fluids Engineering 145(6), 061104.

- **J Kelly**, J Zhu, H Bart-Smith, H Dong (2024) "Computational study of morphokinematic effects in tuna-inspired robots," ASME IMECHE 2024 142816.

- **J Kelly**, P Han, T Van Buren, H Dong (2021) "Wake structures and effect of hydrofoil shape in efficient flapping propulsion," ASME FEDSM 2021 85307.

- **J Kelly**, J Guo, G Forrer, J Zhu, H Bart-Smith, H Dong "Hydrodynamics of body flexibility in tuna-inspired robotics," (**under preparation**) Target: Bioinspiration and Biomimetics

- Blake Wiese, **J Kelly**, J Zhu, H Dong, H Bart-Smith "Connecting computational and experimental methodology for hydrodynamic performance in flexible tuna-inspired swimming" (**under preparation**)

Chapter 6 discusses the results from simulations on the effects of body shape on 2D and 3D undulating swimmers. Section 6.1 details the study of morphology effects in

a 2D diamond-arranged fish school. Section 6.1.1 details the class shape transformation method used to generate body shapes with independently controlled fundamental shape parameters and details the kinematics and configuration of fish in the school. The setup of the simulation is presented in section 6.1.2. Section 6.1.3 presents the results for each body shape in a solo and schooling simulation, and section 6.1.4 discusses the hydrodynamics involved in these results. Finally, a brief summary of the section is provided in section 6.1.5. Section 6.2 presents a new methodology for generating three-dimensional fish-like body shapes, a study of shape parameters in biological swimmers, and the results of numerical simulations of solo and stagger arrangement swimmers utilizing a variety of body shapes. Section 6.2.1 details the method used for generating body and tail shapes. It then discusses the digitization of CT scans of fish bodies and the resulting parameter range used for the parametric study. The undulating kinematics and stagger arrangements, along with the final shapes used in the study, are then provided. The simulation setup is presented in section 6.2.2. The results from the single and staggered swimmer study, along with a discussion of the hydrodynamics, are presented in section 6.2.3. Finally, a brief summary of the section is provided in section 6.2.4. The results of this chapter form the basis for the following publications:

- **J Kelly**, H Dong (2024) "Effects of body shape on hydrodynamic interactions in a dense diamond fish school," Physics of Fluids 36(3).

- **J Kelly**, Y Pan, H Dong (2022) "Body shape effects on the hydrodynamic performance of bio-inspired undulating swimmers," ASME FEDSM 2022 85833.

2 Methodology

2.1 Immersed Boundary Method Flow Solver

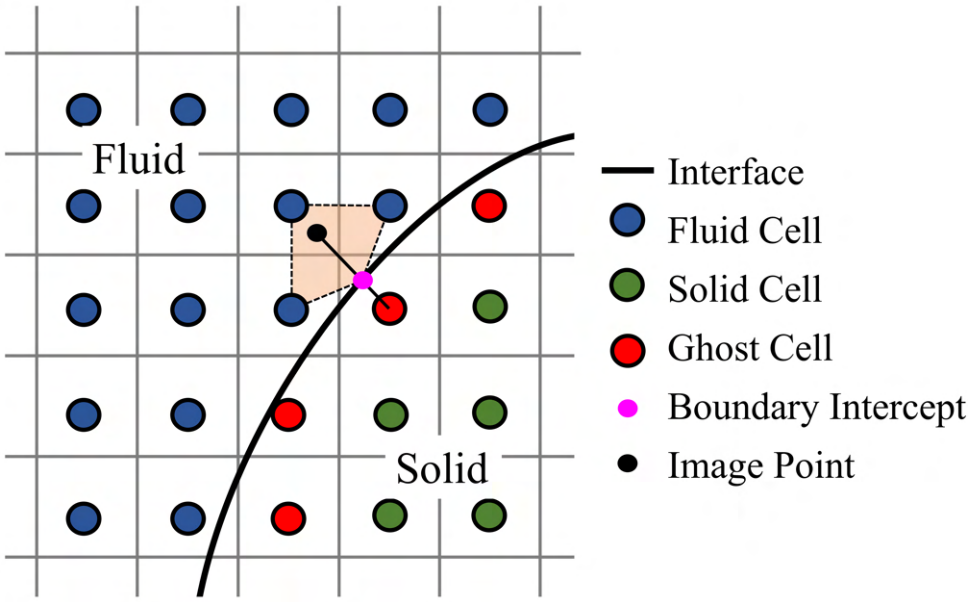

FIGURE 2.1: Schematic of Ghost Cell Immersed Boundary Method

In this study, the 2D and 3D unsteady viscous incompressible Navier-Stokes equations, written in index form as

$$\frac{\partial u_i}{\partial x_i} = 0; \quad \frac{\partial u_i}{\partial t} + \frac{\partial u_i u_j}{\partial x_j} = -\frac{\partial p}{\partial x_i} + \frac{1}{Re}\frac{\partial u_i^2}{\partial x_j \partial x_j}, \tag{2.1}$$

govern the flow. In the equations, p is pressure, u_i denotes Cartesian velocity components, and Re is the Reynolds number, given by the equation $Re = \frac{U_\infty c}{\nu}$. An in-house immersed boundary method-based finite difference flow solver is employed to solve the equations, which are discretized spatially using a cell-centered collocated arrangement of the primitive variables and integrated in time using a fractional step method, which is second-order accurate in time. The convection and diffusion terms are solved using an Adams-Bashforth scheme and implicit Crank-Nicolson scheme, respectively. The immersed boundary method utilizes a ghost-cell method to employ a complex interface boundary over a stationary Cartesian grid. A schematic is shown in Fig. 2.1. The process begins with identifying each cell on the Cartesian grid. Fluid cells are cells with the center outside the body, and solid cells are made of cells completely inside the body and not adjacent to the boundary. Ghost cells have a cell center inside the body and have neighboring cells outside the body. In order to preserve the boundary condition and maintain second order accuracy, a line is extended from the ghost cell through the boundary normal to the interface. An image point is defined as equidistant to the boundary intercept as the ghost cell center. An interpolation process is then used to calculate the values at the image point from the surrounding fluid cells, which is then used to obtain the value on the ghost cell. This method allows for simulation of complex moving boundaries on a stationary grid, without the computationally expensive re-meshing required by commercially available CFD solvers. It has been successfully employed in previous biological swimming studies [83]–[86] and bio-inspired canonical problems [70], [71], [77], [87], and has been previously validated extensively [85], [87], [88]. More details can be found in previous works [89]–[91].

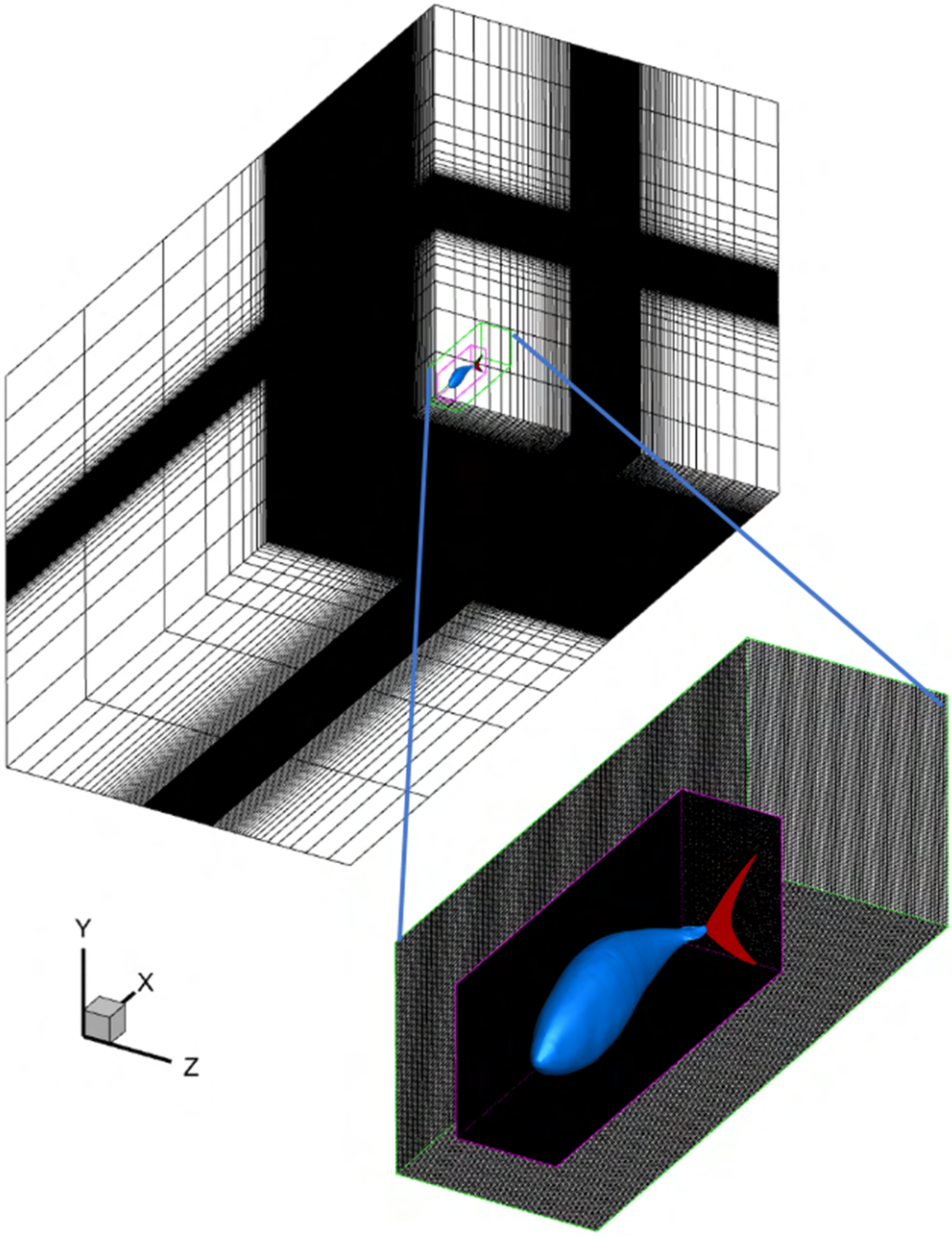

FIGURE 2.2: Grid and two layers of mesh refinement blocks around a single fish

To efficiently allocate mesh in a Cartesian grid and enable parallel computation on distributed memory, a tree-topological block-based mesh refinement method is utilized. The refinement block structure around a single fish is shown in Figure 2.2. More details of the mesh refinement can be found in Zhang et al. [91].

2.2 Force Calculations

To calculate the hydrodynamic forces on a body, F_x and F_y, the solver directly integrates the projected surface pressure and shear force over the body, expressed as:

$$F_x = -\int_S \Big(-pn_x + \tau_{ix} n_i \Big) dS, F_y = -\int_S \Big(-pn_y + \tau_{iy} n_i \Big) dS \tag{2.2}$$

where the indices i=1,2,3 represent the x, y, and z direction, τ_{ij} is the viscous stress tensor, and n_i represents the ith component of the unit surface normal on element dS. Note that F_x is in the -x direction such that a positive F_x indicates net thrust and a negative F_x indicates net drag. In a two-dimensional undulating swimmer, the thrust and drag producing parts of the body are combined into a single surface. To separate these forces, the net force in x can be further deconstructed into thrust and drag components, F_x=F_T+F_D. The thrust is computed as:

$$F_T = \frac{1}{2}\Big(-\int_S -pn_x dS + \left|\int_S -pn_x dS\right| \Big) + \frac{1}{2}\Big(-\int_S \tau_{ix} n_i dS + \left|\int_S \tau_{ix} n_i dS\right| \Big) \tag{2.3}$$

The power required for the undulating motion P_u is calculated as follows:

$$P_u = \int_S (-pn_i + \tau_{ij} n_j) \Delta u_i dS \tag{2.4}$$

where Δu_i is the velocity of an element dS relative to its surrounding fluid in the ith direction. The forces and undulating power can then be normalized by body length and swimming speed, giving the following coefficients:

$$C_{x,y,T} = \frac{F_{x,y,T}}{\frac{1}{2}\rho U_\infty^2 l} \tag{2.5}$$

$$C_{pw} = \frac{P_u}{\frac{1}{2}\rho U_\infty^3 l} \tag{2.6}$$

2.3 Validation

To validate the computational solver for multiple bodies interacting in a flow, the experimental work of Boschitsch et al. [76] is reproduced using the solver to verify its accuracy. In this experiment, two flapping foils are studied in an in-line configuration, varying the phase with a fixed streamwise distance between foils. The foils span the depth of the channel, mitigating 3D effects and allowing a close comparison between the experiment and a 2D simulation. A frictionless air bearing system is used alongside a load cell to measure the net thrust, used to calculate the thrust coefficient given in the results. PIV is also used to produce a vortex field and cycle-average velocity.

The results from the experimental data along with the computational comparison from our solver are shown in Fig. 2.3. In part (a) and (b), the thrust coefficient for experimental data is given by the points and the computational data shown by the lines.

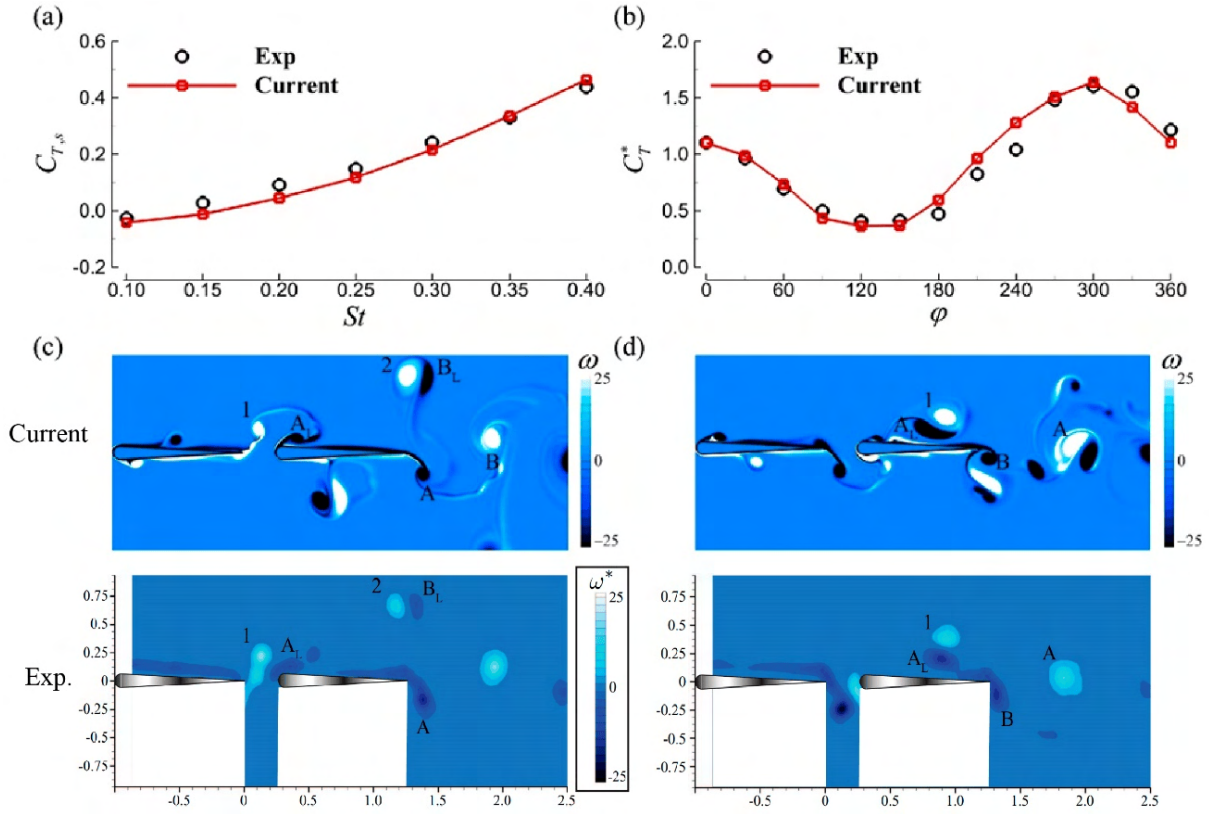

FIGURE 2.3: (a) Thrust coefficient $C_{T,s}$ of solitary foil pitching at different St and (b) normalized cycle-averaged thrust coefficient C_T^* of downstream foil in a two in-line foil configuration pitching at St=0.25, Re=4700 from the current flow solver and experimental (Exp) measurements. Vorticity contours of two in-line foils pitching at St=0.25, Re=4700 with streamwise distance s/C=0.25 and phase difference (c) $\phi = 180°$ and (d) $\phi = 0°$ obtained from the current flow solver (Upper) and the experiments (Lower).

The forces show a very close match for both the single-foil and multi-foil interaction at each phase. This confirms the validity of our solver in calculating the hydrodynamic performance in multi-foil interacting systems. Parts (c) and (d) contain the vorticity and time-averaged velocity from the experimental and computational data. From the figure, both the vortex structure and the jets of the experimental and computational data match very closely, further validating our computational solver for wake analysis in multi-body interacting flows.

To further validate the computational solver for body-body interacting flows, the experimental work of Dewey et al. [92] is reproduced using the solver to verify its accuracy. In this experiment, Dewey studies two flapping foils in a side-by-side configuration, varying their phase and spacing at the Strouhal number of maximum efficiency (0.25). The foils span the entire depth of the water channel, mitigating their 3D effects and allowing a 2D computational approximation to compare closely with their results. A frictionless air bearing system is used alongside a load cell to measure the net thrust, used to calculate the thrust coefficient given in the results. PIV is also used to produce a vortex field and cycle-average velocity.

The results from the experimental data along with the computational comparison from our solver are shown in Fig. 2.4. In part (a) and (b), the thrust coefficient for experimental data is given by the points, along with the computational data shown by the lines. From this, we see that almost every data point is within the experimental error. The forces show a very close match for both the single-foil and multi-foil interaction at each phase. This further confirms the validity of our solver in calculating the hydrodynamic performance in multi-foil interacting systems. Parts (c) and (d) contain the vorticity and time-averaged velocity from the experimental and computational data. From the figure, both the vortex structure and the jets of the experimental and computational data match very closely, further validating our computational solver for wake analysis in multi-body interacting flows.

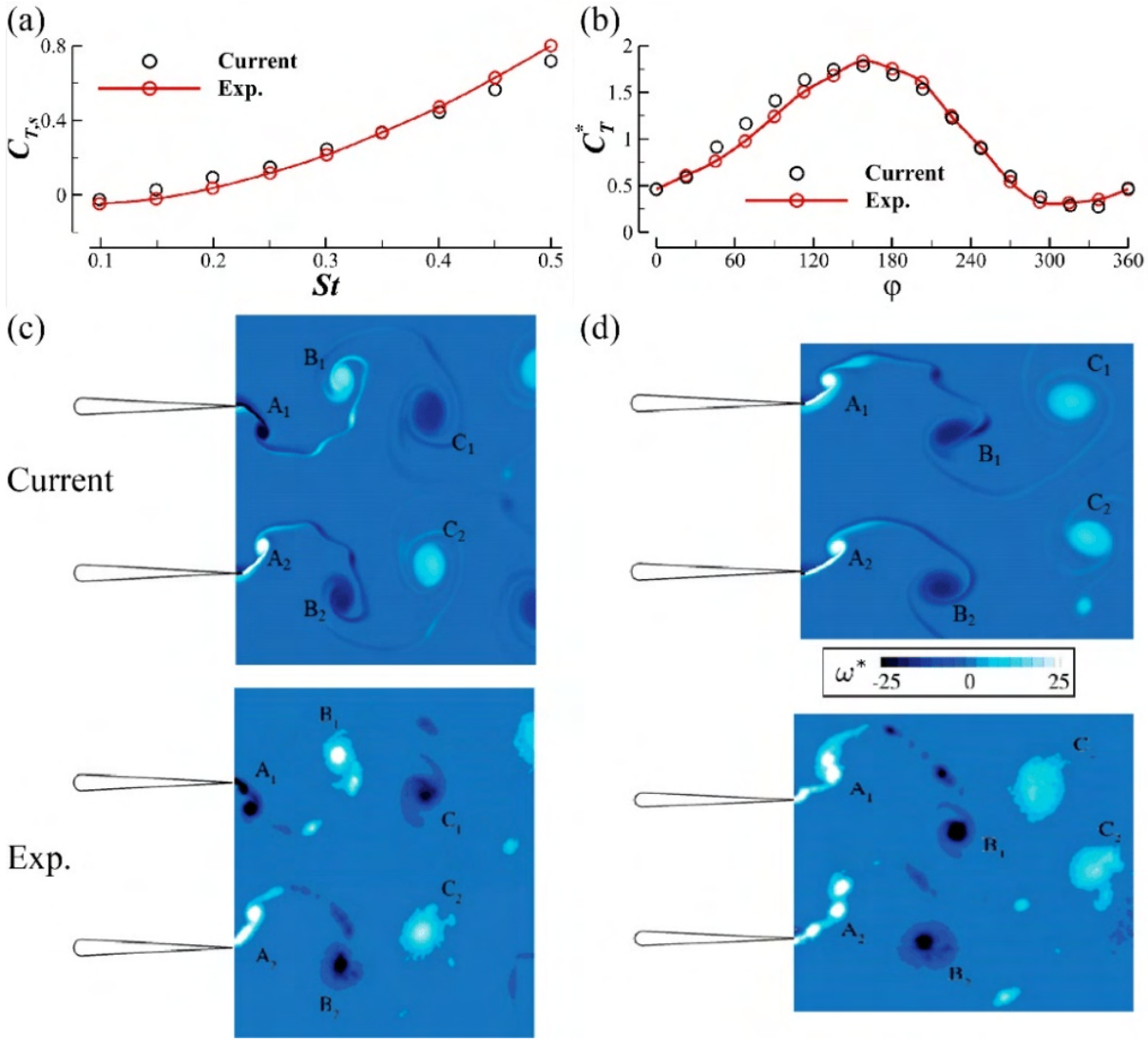

FIGURE 2.4: (a) Thrust coefficient $C_{T,s}$ of solitary foil pitching at different St and (b) normalized cycle-averaged thrust coefficient C_T^* of downstream foil in a two side-by-side foil configuration pitching at St=0.25, Re=4700 from the current flow solver and experimental (Exp) measurements. Vorticity contours of two in-line foils pitching at St=0.25, Re=4700 with streamwise distance s/C=0.25 and phase difference (c) $\phi = 180^\circ$ and (d) $\phi = 0^\circ$ obtained from the current flow solver (Upper) and the experiments (Lower).

3 Arrangements of Large Fish School

To examine the effect that swimming in large schools of varying arrangements has on the interactions and performance of fish schools, fish-like undulating foils are studied numerically in high-density planar arrangements. The study varies the formation of the schools, which are built based on the dense diamond, into long, wide, and diamond-based schooling formations. An immersed boundary method-based flow solver is used to resolve the flow around the fish bodies in different schooling arrangements, phase lags, and school sizes. In the large school, the school averaged efficiencies increased by more than 40% over a single swimmer, an additional 18% increase over the diamond school formation. Individual fish within the large schools have efficiency increases of over 90% compared to a solo swimmer. The results find consistency with the mechanisms and classification of prior studies of elongated schools and find that as schools grow significantly larger, critical pressure interactions due to synchrony determine much of the performance scaling of the arrangement. Analysis of the wake shows that the spacing in the 2S core correlates with the thrust production in the arrangement within these schools. Changes to phase reveal that synchronous arrangements are critical to maintaining high-performing schools despite these limitations. Finally, the diamond schools are found to provide the highest performance and balance the benefits

of the high-thrust long schools and the low-power wide schools. They also most successfully distribute the benefits of schooling throughout all the fish in the school rather than a select few.

3.1.1 Problem Statement

To determine the arrangement of fish within the school, the basic dense diamond school is utilized. The diamond school shape has been identified by previous studies to be the most energy efficient for a small number of fish [26], [93], [94]. Most recently the dense school has been identified as the highest efficiency [58], particularly for the diamond configuration [23]. To enable studies of many fish in a school, we utilize the dense diamond as a basic sub-unit of the larger school. This allows us to observe the most efficient arrangements of fish. Additionally, the highly compact dense diamond maximizes interaction between fish within the school. Utilizing this configuration, we capture all the fish-fish interactions experienced by schooling fish. This method has been used previously for studies of large dense fish schools [15].

In keeping with the findings of the previous study, the dense diamond is defined in Fig. 3.1 as $D = 0.4$ and $S = 0.4$. Larger schools are constructed in the long, wide, and diamond configurations. To construct larger schools, additional sub-units of the dense diamond are appended to the previous school. The effect of increasing the school size in this manner is shown in Fig 3.1(a-c), with additional dense diamond sub-units added to each in blue and orange.

To define the fish-like motion for the study, a NACA0012 foil shape is used for the

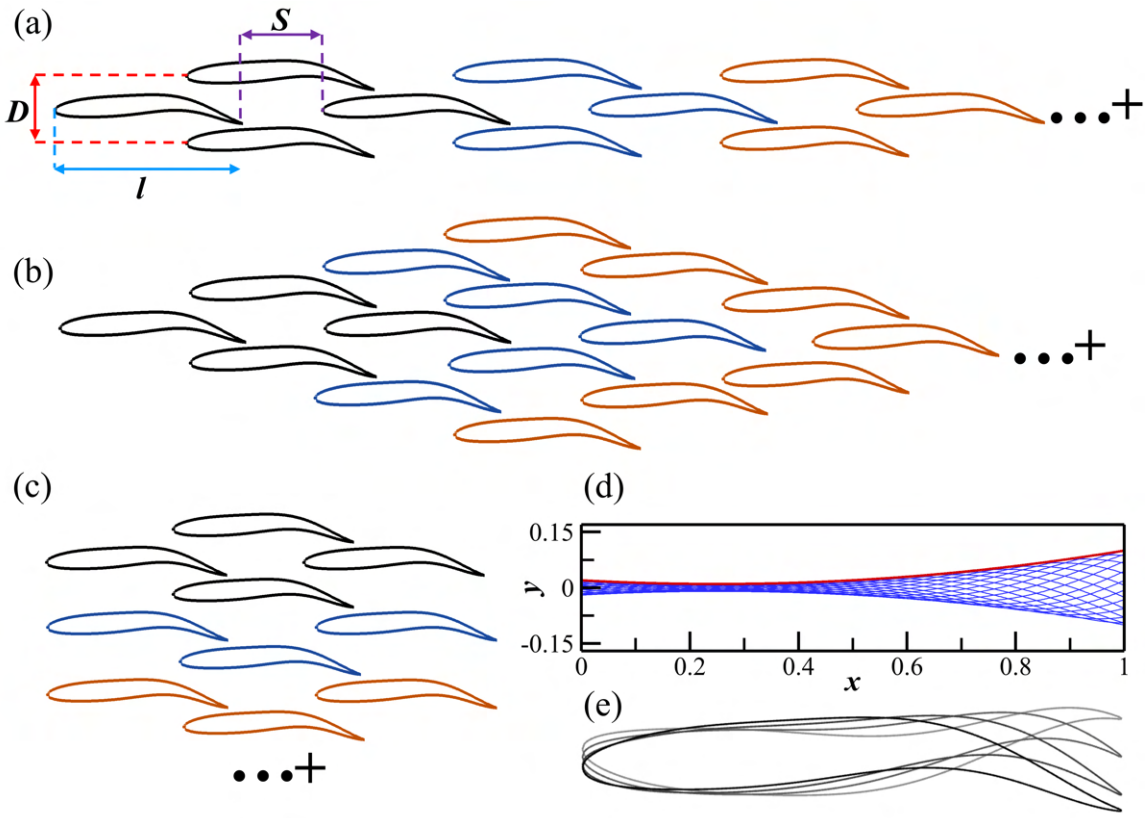

FIGURE 3.1: Schematics of construction for the long (a) wide (b) and diamond (c) schools. The base unit is shown in black, with each subsequent unit shown in blue, then orange. (d) Traveling wave amplitude of carangiform motion in red and the motion of the body midline in blue. The resulting motion through a cycle is demonstrated in (e).

equilibrium state of the fish body. Traveling wave kinematics are then imposed on the foil, giving a resulting undulatory motion that mimics a top-down view of typical carangiform swimming. The body length is scaled to $l = 1$, and the lateral displacement is given by the equation:

$$y(x,t) = A(x)\sin\left(\frac{2\pi}{\lambda}x - \frac{2\pi}{T}t\right), \tag{3.1}$$

where the position variables, x and y, are normalized by the body length such that

at the equilibrium state the midline of the fish body is a flat line at $y = 0$ spanning from $x = 0$ to $x = 1$. $y(x,t)$ represents the lateral deviation from this midline position during the undulating motion. T is the wave period of the traveling wave, and λ is the wavelength, both of which are set to one. $A(x)$ denotes the amplitude of the lateral wave, and is expressed by the following quadratic polynomial:

$$A(x) = a_2 x^2 + a_1 x + a_0, \tag{3.2}$$

where the coefficients are determined to be $a_0 = 0.02$, $a_1 = -0.08$, and $a_2 = 0.16$. These were determined by previous experimental data [95] and have been used in previous 2D computational studies of fish swimming [23], [77]. The wave amplitude envelope and resulting midline sequence through a cycle of motion are given in Fig. 3.1(d), and the resulting motion in Fig. 3.1.

3.1.2 Simulation Setup

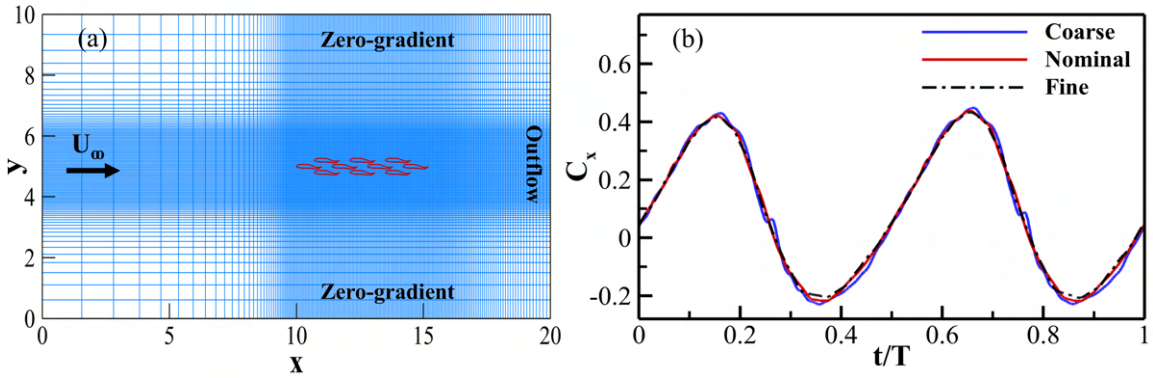

FIGURE 3.2: (a) Schematics of the computational domain, Cartesian grid, and boundary conditions, with a detailed inset of the grid density on the body. (b) Comparison of the instantaneous net force coefficient of the last fish in the long 10-fish school between the coarse, medium, and fine mesh.

A representative Cartesian grid is shown in Fig. 3.2(a) for the 10-fish long school. The domain employed is $10l \times 20l$, with the domain length growing for each longer school. Around the body, a fine mesh region is employed with a minimum grid spacing of $0.0035l$. The resulting grid is 1696×704 and has approximately 1.2 million total grid points. The boundary conditions are also shown, with the velocity boundaries defined by an inlet boundary condition with U_∞ from the left, an outlet boundary condition on the right to allow vortices to exit the domain without reflection, and zero gradients upper and lower boundaries with U_∞ to enforce free stream conditions. A grid independence study was completed on this grid, shown in Fig. 3.2(b). In the figure, the net force in the -x direction is shown for the back fish using each of the grid sizes, where the coarse mesh has a minimum grid size of $0.0051l$ and the fine mesh has a minimum grid size of $0.0025l$. The average and peak C_x values, calculated as $C_x = \frac{F_x}{0.5\rho U_\infty^2 l}$, are within 2 percent for the nominal and fine grids, so the nominal grid is determined to be sufficient for the study. This grid density was tested for increasing school width and length and found to be sufficient. Throughout the study, the dense region of the grid and domain size are scaled to maintain distance from the boundary to the school to keep grid independence.

For the study, the undulating swimmers remain in a fixed position with no translational or rotational degrees of freedom. We find the steady-swimming condition by obtaining the flow parameters that result in a cycle-averaged net force of 0 for the single swimmer. The Reynolds number Re is chosen to be 1000. This is consistent with previous literature [23], [71] and corresponds to a higher Reynolds number in three

dimensions [93]. In this Reynolds number regime, the viscous effect is small while coherent vortex structures are still maintained [81]. The effect of changing the Reynolds number in large schools has been investigated in Kelly et al. [15]. With a fixed Re, we simulate a range of flow velocities to find the steady-swimming condition. This results in a steady-swimming Strouhal number ($St = 2fA/U_\infty$) of 0.43. We summarize all flow and kinematic parameters in Table I. A is a result of the equations given in Fig. 3.2. The body length l and the wavelength λ are both set to one.

Re	A	λ	l	St
1000	0.1	1.0	1.0	0.43

TABLE 3.1: Parameters used in this study

For the parameters chosen in this work, the time-averaged thrust of a single fish is $\overline{C_T} = 0.22$, the undulating power coefficient is $\overline{C_{Pw}} = 0.28$, and the associated propulsive efficiency is $\eta = 0.44$. Specifically, the swimmer suffers drag at the snout, while the tail generates most of the thrust and power consumption. The shedding vortices behind the fish form a 2S wake. More details about a single swimmer's hydrodynamic performance and flow field can be found in Pan and Dong [23], [52].

3.1.3 Results

To begin the study, simulations are completed for the long, wide, and diamond schooling arrangements varying from 4 to 25 fish. Following Kelly et al. [15], classifications of individual fish based on the spatial arrangement within the school are utilized to help visualize the data. Individual fish are categorized into the front, edge, middle,

and back swimmers in the school. The net force and efficiency for each swimmer in all of these schools are plotted in Fig. 3.3.

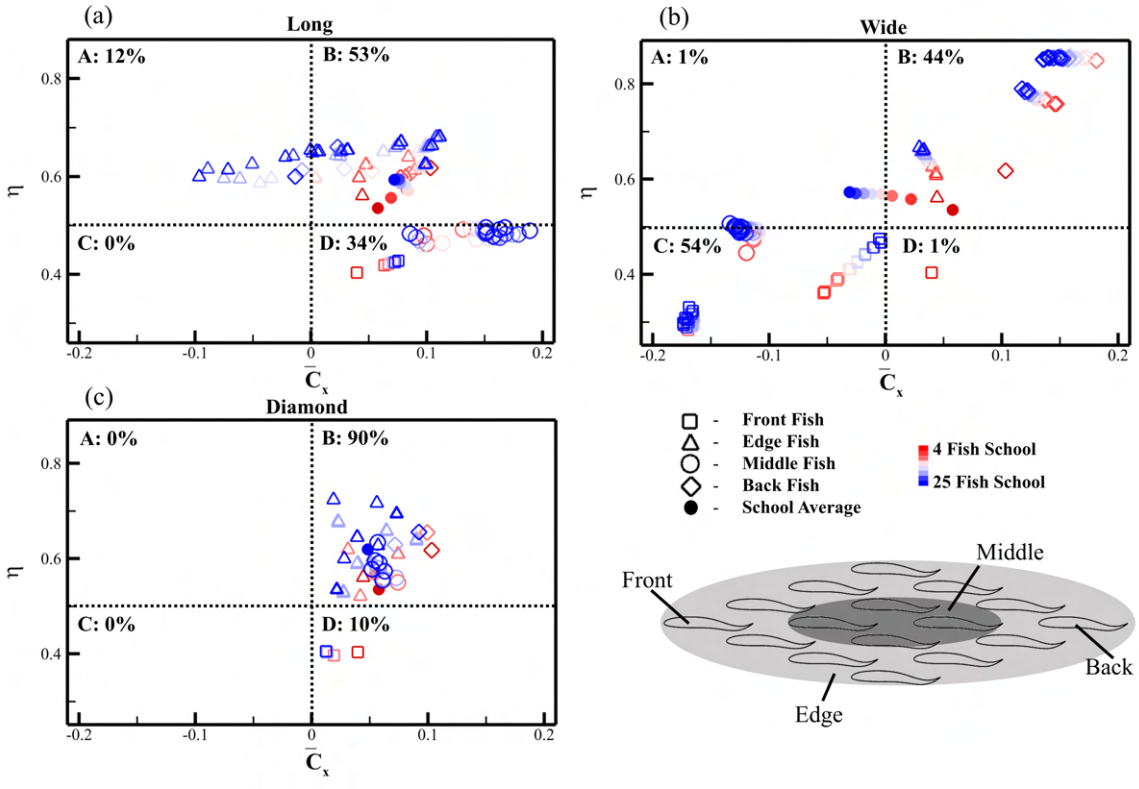

FIGURE 3.3: Cycle averaged force coefficient and efficiency for each individual fish in the long (a) wide (b) and diamond (c) schools. Fish are colored based on school size according to a red (small) blue (large) color gradient. The shape of each data point depends on the location of the fish within the school. (a).

In the figure, the data is broken up into long, wide, and diamond school constructions. Each fish is labeled based on the shape of their classification and the color of their school size. To further ease the interpretation of this data, fish are divided into four quadrants. Quadrant A includes fish with high efficiency ($\eta > 0.5$), and low net force ($C_x < 0$); quadrant B indicates high efficiency and high net force; quadrant C indicates low efficiency and low net force; and quadrant D indicates low efficiency, and high net force. The total number of fish in each performance region is summed and shown as a

percentage at the top left of each region.

The figure shows that the largest percentage of fish gaining advantage from schooling in the high efficiency, high net force region, occur in the diamond schools. Long schools generally include high net force swimmers, at the cost of the front and middle swimmers gaining less efficiency. Wide schools occupy a large range of performance, with the back fish gaining large efficiency and net force benefits while the front fish suffer large efficiency and net force drops.

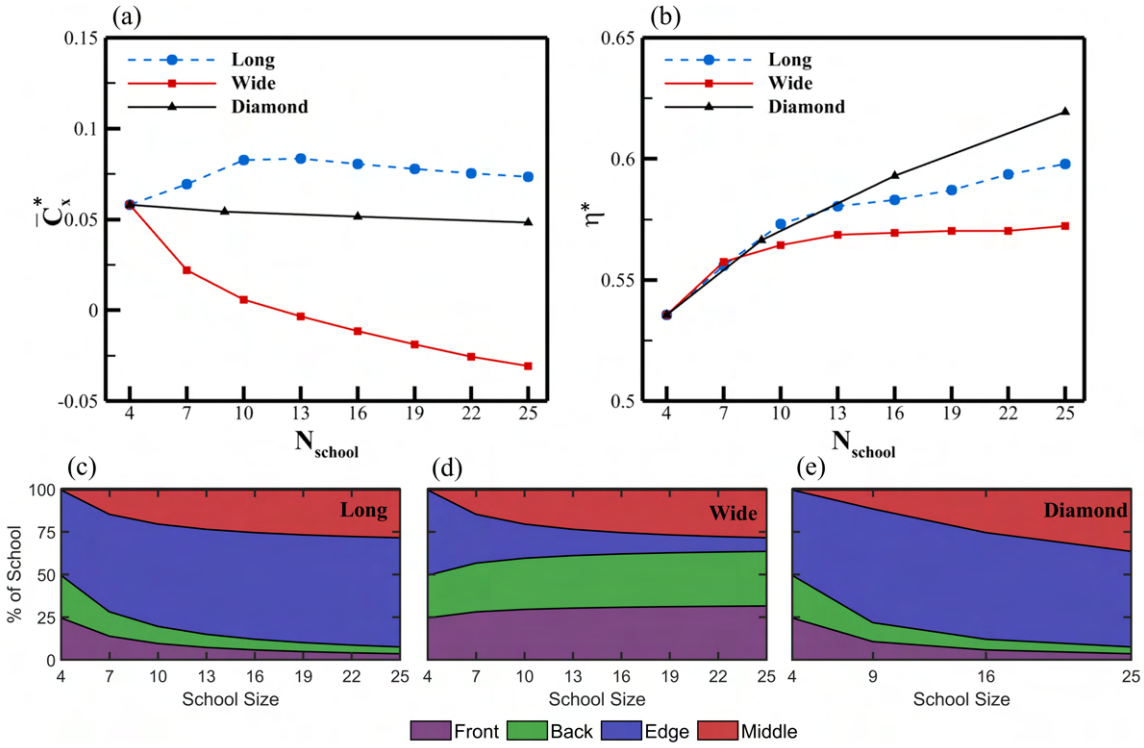

FIGURE 3.4: School averaged and cycle averaged net force (a) and efficiency (b) for the long, wide, and diamond schools from 4 to 25 fish large. School composition, broken into front, edge, middle, and back fish, is shown for the long (c), wide (d), and diamond (e) schools.

To understand the overall trends for each method of increasing school size, the school averaged net force and efficiency results are provided in Fig. 3.4(a-b). In the figure,

results are shown for each school from 4 fish to 25 fish with all three growth methods. In the figure, it is evident that the long school provides the highest benefit in terms of net force, while the diamond schools provide the most benefit in terms of efficiency. Particularly of note, the net force average in the wide schools crosses below zero, suggesting that the schooling interaction serves as a detriment to the force produced by swimming in these wide schooling arrangements.

Finally, the composition of each school in terms of the spatial position as shown in Fig. 3.3 is shown in Fig. 3.4(c-e). The results show that increasing the width of the school quickly adds to the number of front and back fish present, while shrinking the portion of edge fish. Increasing the length of the school or in the diamond increases the number of edge fish significantly, with a slight increase in the middle fish and a shrinking portion of front and back fish as the school grows.

3.1.4 Discussion

In this section, the hydrodynamics behind the performance for each schooling arrangement is discussed in depth. Next, a comparison between arrangement methods is given. Finally, the effect of phase in each arrangement is discussed.

3.1.4.1 Long Schools

The hydrodynamics in a long school are investigated in the thesis of Kelly [96] and summarized below:

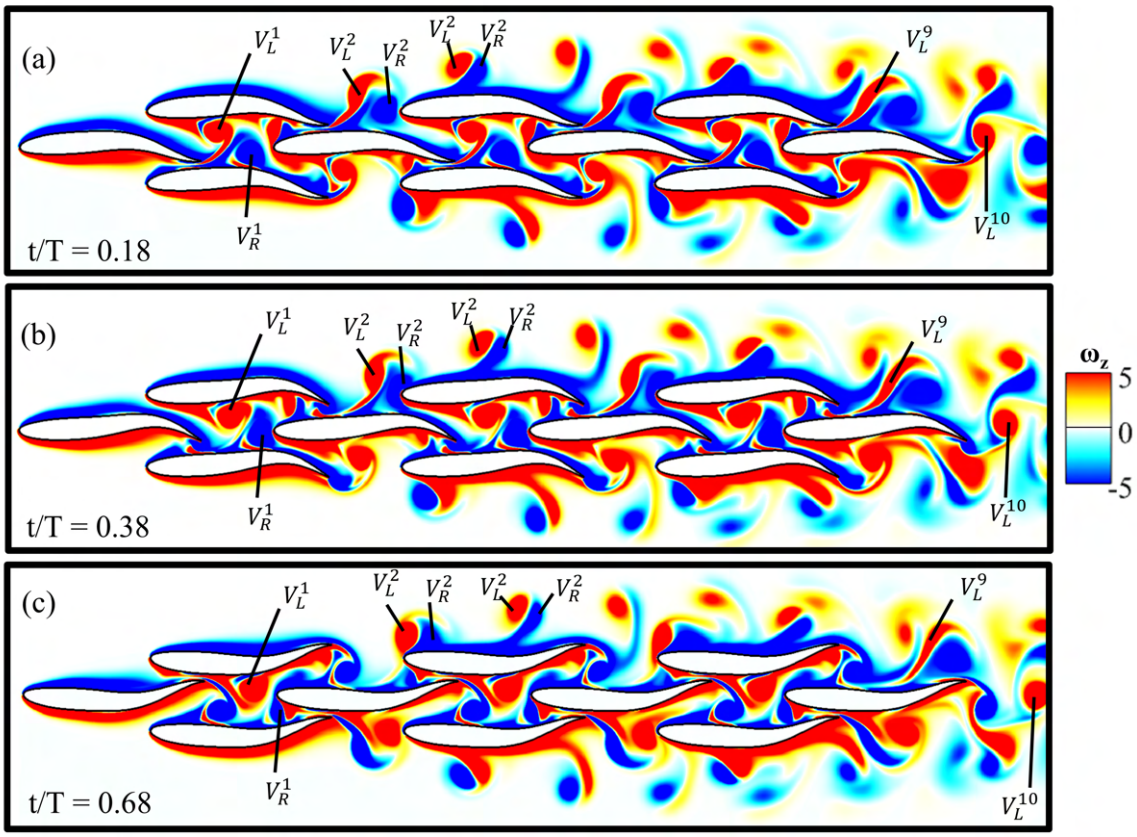

FIGURE 3.5: Vorticity (a-c) at $t/T = 0.18$, 0.38, and 0.68 in the long 10 fish school. Key vorticies are noted.

To investigate the flow within the school the vorticity for the maximum and minimum C_x is given in Fig. 3.5. Major vortices are labeled using $V_{L/R}^{\#}$, where the top number indicates the fish where the vortex originates, and the letter on the bottom indicates that it is generated during the left or right stroke. During each half stroke, the trailing edge vortex is shed off the tail region of the fish. For all but f_{10}^{10}, the tail also interrupts the shear layer of the next fish in the school, causing a small induced vortex which has been discussed at the back of diamond schools [52]. The shed vortex then advects downstream. An example is shown by V_L^1 and V_R^1, where each is seen advecting along the body of the next fish after shedding from the trailing edge vortex of f_1^{10}. The induced vortices can be seen along the body of f_2^{10} and f_3^{10}. For the fish along the

mid-line, the vortex is then captured by the channel of surrounding fish and intercepts the head of the next fish behind it. On the edges of the school, the vortices form a pair and advect laterally outside the school after intercepting the next fish in line, as shown by V_L^2 and V_R^2. For f_{10}^{10} at the back of the school, a single vortex (V_L^{10}) is shed in each half stroke with no subsequent interactions.

The flow mechanisms within the school have been broken down into three major components summarized as the wall effect, block effect, and anterior body suction effect, which are summarized in the following sections. Each of these have been demonstrated in prior work, and appear in a modified form within the context of larger schools.

Anterior Body Suction

The anterior body suction effect is shown in Pan and Dong [52] to occur from the low-pressure suction that is generated on the tail of one fish interacting with the head of the fish behind it. In the paper, the effect is discussed within the context of the back fish of the diamond, which saw a moderate suction force on its head when the body phases are matched. To investigate the effects of this throughout the school, the anterior portion of the body, defined as the first 30% of the body length, is observed through the cycle of motion. The net force is plotted in Fig. 3.6, with the superscript a denoting the anterior portion of the body only. Note that only the top edge fish are included in the figure, as it has already been shown that the bottom-edge have the same results due to symmetry. Additionally, the pressure contour is shown at $t/T = 0.25$(a)

and $t/T = 0.75$(b). The mid-line fish all show two peaks and two troughs in f_x^a, whereas the fish along the edge of the school have a single peak and trough of significantly higher magnitude.

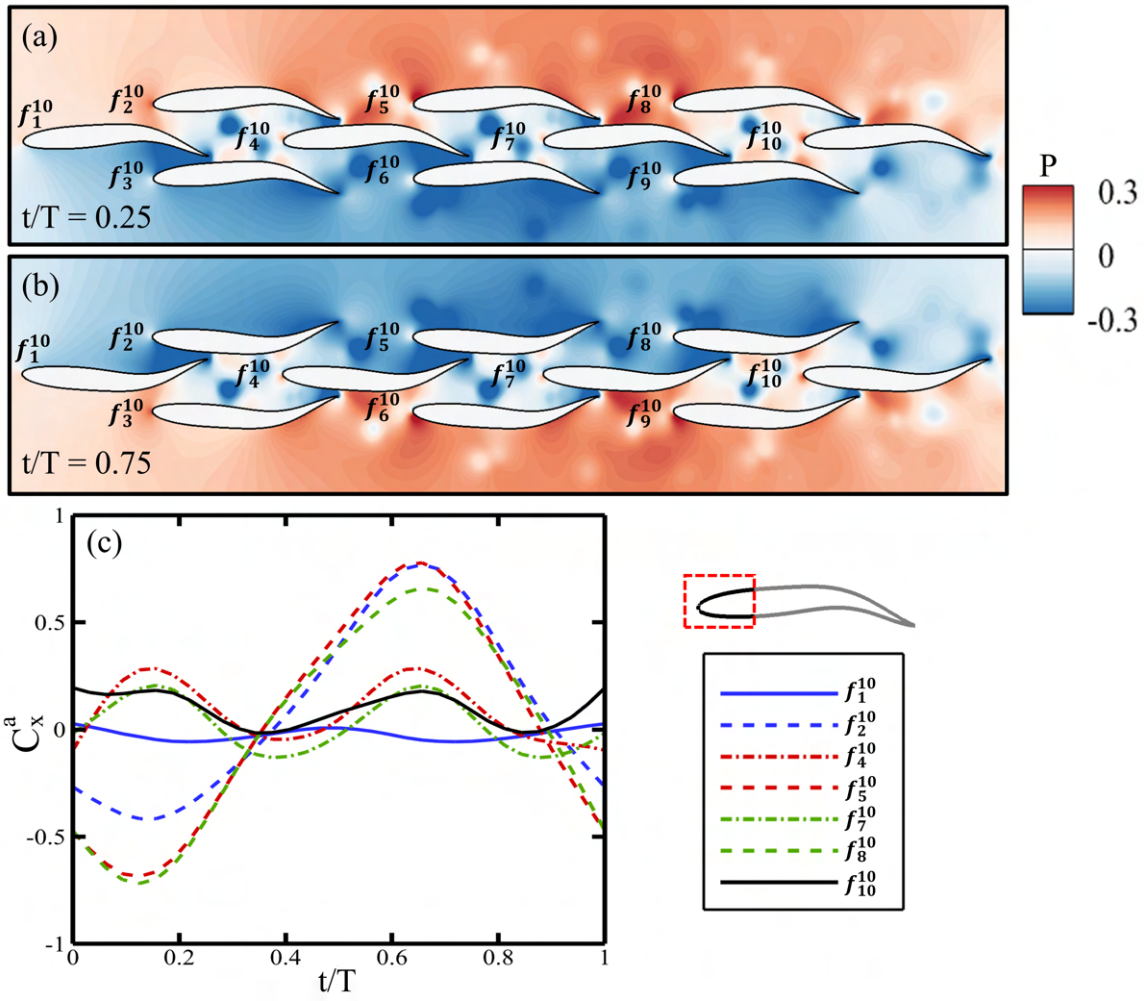

FIGURE 3.6: Anterior body suction effect in the 10 fish long school shown via pressure contour (a-b) and anterior net force (c) over a cycle of motion for each fish. Anterior fish body is defined as the first 30% of the body, as shown.

The reason for this can be seen in Fig. 3.6(b). In this time step, the top-edge fish are experiencing peak thrust from the anterior body suction. The bottom-edge fish, on the other hand, are near the lowest point in their anterior net force. This can be seen using the example of the front fish (f_1^{10}). The front fish tail has created a low-pressure suction

and high-pressure pushing on each side of its tail. On the suction side, the top-edge fish (f_2^{10}) is benefiting heavily from interacting with this low-pressure suction zone, gaining a large net forward force on its anterior. On the other side, the high-pressure side of the front fish also interacts with f_3^{10}, creating a large drag on its anterior portion. This effect also explains the high-thrust zones at the head seen in Fig. **??** where the mid-line fish have two small thrust and drag zones and the edge fish has one large thrust zone and one large drag zone on its anterior. This effect can be seen all along the edge fish on the top and bottom of the school in Fig. 3.6(a) and is expected to occur any time the suction side of a tail is near the head of another fish. In the middle fish, some net suction on the anterior is still observed, similar to the back fish in the diamond school noted by Pan and Dong [52]. This occurs due to similar suction and pushing as the edge fish, but because it has a fish on either side of it, the effects occur simultaneously. The low and high-pressure regions on the anterior largely cancel out, leading to a much smaller net effect. The net effect is still suction on the anterior because the low-pressure tail is much nearer to the head of the fish than the high-pressure tail. This allows the low-pressure zone to be more dominant around the anterior, leading to the smaller net suction observed in the middle and back fish. An example of this is seen in Fig. 3.6(a), where f_4^{10} has mostly low-pressure around its head but is not as dominant as the previously discussed edge fish. The low-pressure from f_3^{10} and high-pressure from f_2^{10} are largely canceling out, but the head of f_4^{10} is significantly closer to the tail of f_3^{10}, meaning the low-pressure is more dominant on the body. The mid-line fish are all experiencing moderate anterior body suction, focused around the top-edge of the fish. The bottom-edge fish are in a high anterior body suction state with high net force

around the head, and the top-edge fish are in the opposite state, with high drag around the head resulting from high-pressure in front of them. Throughout this motion, the power consumption remains similar between groups on the anterior, but the front and edge fish consume less than the middle and back. Because of this, the edge fish have a more distinct cycle of high and low net force on the anterior. The low anterior thrust occurs when the tail is flapping into the school where the anterior is low net force, and subsequently low efficiency. The high anterior thrust occurs when the tail is flapping away from the school, where the net force is high and the power consumption has not significantly increased, so the efficiency is significantly higher.

Block Effect

The block effect is shown in prior research [23] to occur when the flow behind a fish body is blocked by another body, leading to an increase in pressure between the fish and increasing the performance of the front fish. In the context of their dense diamond school, it was demonstrated in the front fish when adding the back fish to the school, with the channel of edge fish present to block the flow from propagating laterally. Also, it was shown that in the blocking effect the flow of the vortices is prevented in the downstream. Within the context of the large school, the block effect is also observed. From the observations of the vortex structure in Fig. 3.5, we know that the vortices behind f_1^{10}, f_4^{10}, and f_7^{10} are blocked in their downstream propagation and f_2^{10}, f_3^{10}, f_5^{10}, and f_6^{10} also have partial blocking of the vortex pairs from the downstream.

To investigate the effects further, the cycle-averaged pressure distribution is given in

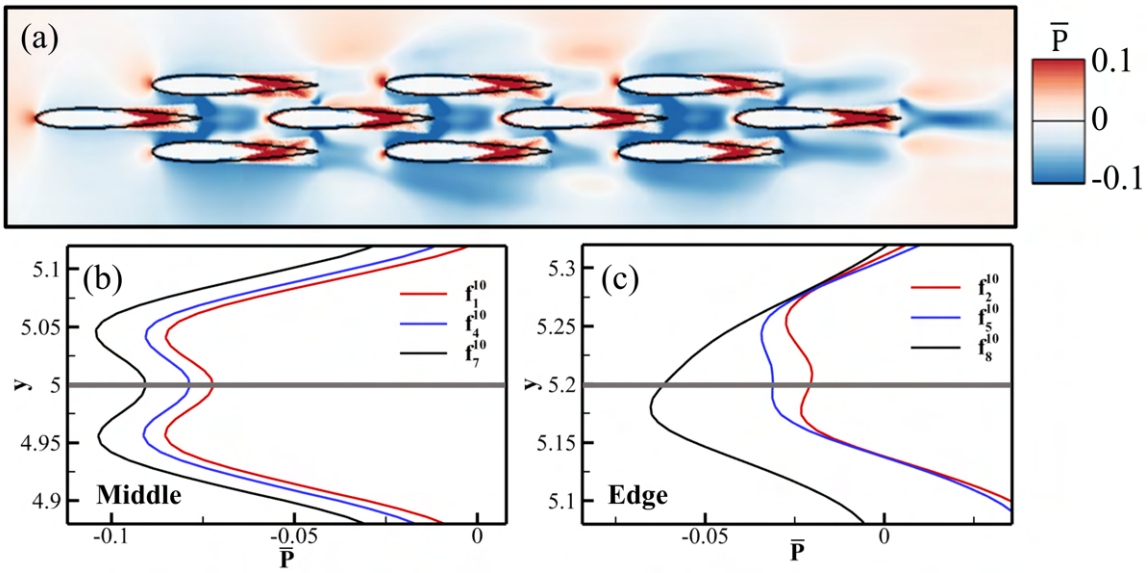

FIGURE 3.7: Demonstration of the block effect in the long 10 fish school utilizing the cycle-averaged pressure (a). The cycle averaged pressure at $0.1l$ behind each fish tail for the mid-line fish (b) and top-edge (c) fish are also shown, with the y position of the fish marked in grey.

Fig. 3.7(a). Along the edges of the school, an increased pressure in between is observed when a fish is behind another, giving evidence of a partial block effect along the edges of the school. Additionally, the same interrupted pressure zone shape observed in Pan and Dong [23] is observed in the channel behind the front and middle fish. Unsurprisingly, the block effect continues to occur in the channel for each of these fish. Unexpectedly, this effect is not limited to blocking by a single fish. This is shown more clearly in Fig. 3.7(b-c), where the cycle averaged pressure profile at $0.1l$ behind each fish along the mid-line and top edge of the school. The pressure continues to rise going from the back of f_7^{10} to f_4^{10} to f_1^{10}. This can be explained by the further blocking of the fluid flowing down the channel. For f_4^{10}, there is both f_7^{10} and f_{10}^{10} in the channel behind it, leading to a further increase in pressure compared to just one fish blocking the flow. This enhanced block effect is observed along the middle channel, but also

in a much weaker form for the edge fish where the pressure behind f_2^{10} is increased slightly compared to f_5^{10} because of the presence of more fish behind it. The effect of this is significantly lessened, however, because of the lack of a channel containing the flow, so much of the fluid flows laterally around the subsequent blocking fish.

Wall Effect

Many previous studies [92], [97]–[99] have shown that foils oscillating near a solid boundary or next to another foil in anti-phase, providing a wall-like boundary in the other foil body leads to an increase in thrust with only a slight increase in power consumption. Additionally, this effect was observed in Pan and Dong [23] for a dense diamond fish school, with the tail edge of the fish breaking the stability of the shear layer on the "wall" fish. The same pattern of vortex pairs shedding reported by Pan is seen in the flow behind edge fish within the 10-fish school. This is shown along the edge of the school in Fig. 3.5(a), where the vortex pair V_L^2 and V_R^2 are very similar to the flow structure of the wall effect in the dense diamond reported previously. The wall effect occurs any time the tail of a fish flaps close enough to the body of another fish for the fish body to create the effect of a "wall" near the tail of the previous fish. This occurs during half of the strokes for fish along the edge of the school, and both strokes along the mid-line, except f_{10}^{10}. Along the edge, the wall effect only occurs when the tail flaps towards the center of the school. By flapping near a wall, the lateral momentum generated by the tail motion is redirected by the wall downstream. To demonstrate this effect, the normalized x-velocity is shown in Fig. 3.8(a). At this time step, the bottom-edge fish are flapping away from the school and the top edge fish are flapping towards

the school. From this, we expect the top-edge fish to experience a wall effect while the bottom-edge fish do not. This is evident from the velocity zones behind each of the fish, where the top edge fish have a temporary jet of fluid flow downstream, indicating high momentum gained by the fish via Newton's third law. The fish along the bottom, on the other hand, have no high momentum region.

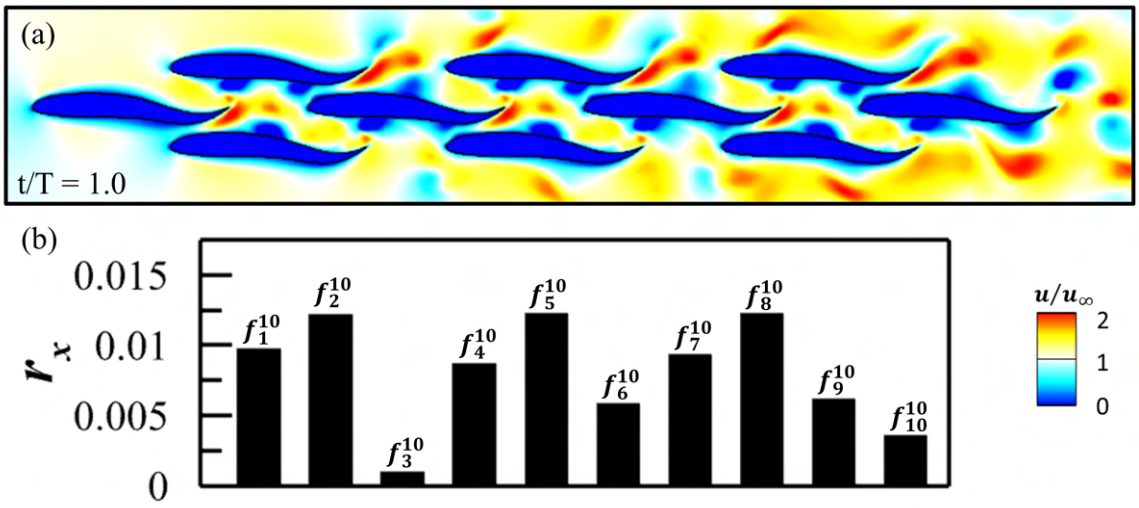

FIGURE 3.8: Normalized x-velocity (a) in the 10-fish long school at $t/T = 1.0$, along with the total streamwise momentum in the temporary jet formed behind each fish (b).

To compare wall effects among the fish, the total momentum of the instantaneous jet behind the tail, r_x, is summed, and the results are given in Fig. 3.8. From the figure, the fish without any wall effect (f_3^{10}, f_6^{10}, f_9^{10}, and f_{10}^{10}) have significantly less momentum at the tail. As expected, the top edge fish (f_2^{10}, f_5^{10}, and f_8^{10}) have the highest momentum, and the fish with smaller momentum jets due to blockage from the middle channel (f_1^{10}, f_4^{10}, f_7^{10}). The discrepancy between the top and bottom edge fish explains the single high thrust region on the edge fish tail, while all the other fish had two zones

of similar thrust at the tail. Behind the front (f_1^{10}) and middle (f_4^{10}) fish, similar high-momentum jets are observed, however, they are interrupted by the subsequent body inside the channel. Because of this, the benefit from the wall effect is lessened for these front and middle fish compared to the edge fish.

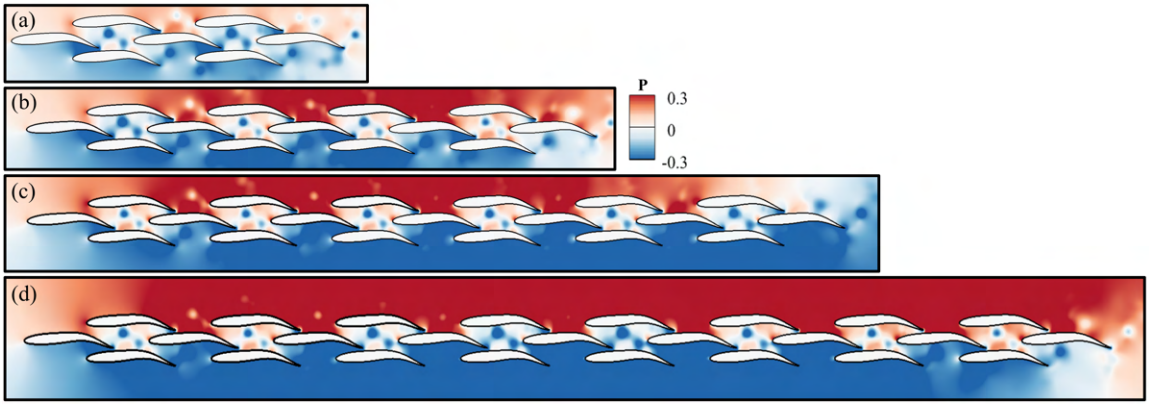

FIGURE 3.9: Instantaneous pressure at t/T = 0.25 for the 7, 13, 19, and 25 fish long schools.

Finally, to summarize the effects of length increase in a dense fish school, the instantaneous pressure of the 7, 13, 19, and 25 fish long schools is plotted at t/T = 0.25 in Fig. 3.9. At this timestep, the undulation motion of the body has generated a low pressure on the lower side of the body and high pressure on the upper side of the body. The tail is angled downwards such that each of these pressures provides some force component in the forward direction. The tail is moving upwards, fighting against this pressure gradient. The synchrony of the school means that all fish are generating the same pressures on their upper and lower surface, and in this long arrangement, those surfaces align closely in space. This results in larger and larger pressure gradient generation during the undulating motion. While this should provide some benefit to the thrust generated from the motion, it also creates more power-consuming gradients to

fight against to achieve that motion. Additionally, the gradient begins to dominate the school as a whole, and in the schools above 16 fish it is seen that the bottom edge fish do not achieve a positive pressure on the back portion of their tail. This runs counter to the forward force, and the net force on the edge fish begins to suffer.

These results correspond well with what is seen in Figures 3.3 and 3.4. In the largest schools, the edge fish occupy the low-thrust, high-efficiency region limiting the performance gain available from long schools.

3.1.4.2 Wide Schools

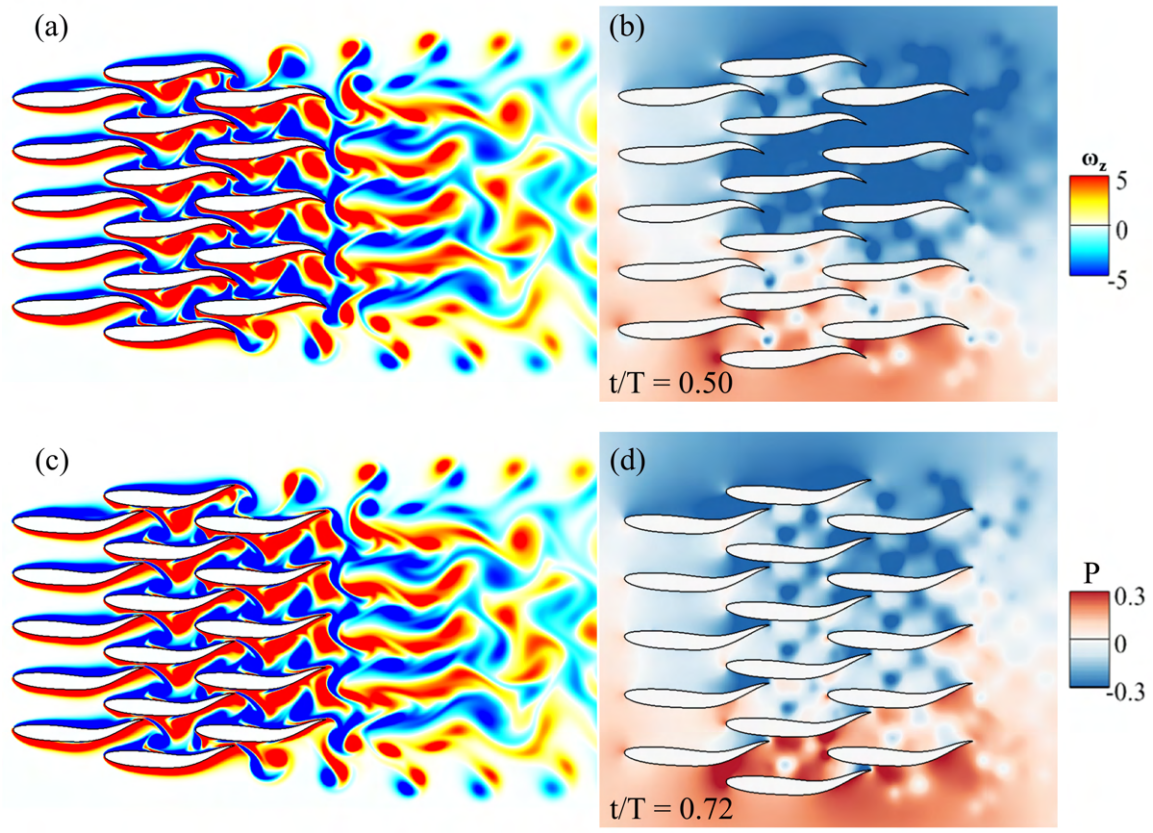

FIGURE 3.10: Vorticity (a,c) and instantaneous pressure (b,d) for the 16 fish wide school at t/T = 0.5 (a,b) and 0.72 (c,d).

Next, the hydrodynamics in the wide schools are analyzed. Unlike the long school, the hydrodynamics within the wide school changes very little with size, as evident by the neat groupings of the individual fish in Fig. 3.3. This makes intuitive sense, as unlike the other formations, the wide school fish do not interact with additional wake created from adding additional fish to the school. Therefore it is logical that outside of their immediate neighboring fish, adding and subtracting fish from the school has little impact on their hydrodynamics. With this information, we can observe only the 16 fish wide school and still gain an understanding of each wide school size in the present study.

To observe the hydrodynamics within the 16 fish school, the vorticity, and instantaneous pressure are plotted at two time instances in Fig. 3.10. In the figure, the dense lateral packing of the fish restricts any lateral advection of the flows that are typical in the diamond and long schools [15], [23]. This limit continues to the wake, which forms combined regions of positive and negative vorticity rather than breaking off into individual vortices each half stroke as is typical in fish-like swimming. This effect continues approximately 1.5 body lengths behind the school before dissipating into individual vortices.

In the pressure, a destructive interaction occurs between swimmers. As a low-pressure region is created on one side and a high-pressure region on the other in order to begin generating thrust, each laterally neighboring fish is generating similar regions. Because of the synchrony of the schools, however, these occur at the same time. Thus, as one fish creates a low-pressure region on its left side, each fish to its left creates a

high-pressure region on their right side, facing the first fish. These pressure regions negatively interact, and the net effect is that with many fish side-by-side in these wide schools, the amount of pressure differential that can be generated is limited. Thus, the thrust generation is limited within these arrangements. This does maintain more favorable pressure gradients for the swimming motion, however, and leads to an overall reduction in the power consumed to generate the swimming motion. This is the opposite of the effect shown in Fig. 3.9.

	Front	Edge	Middle	Back
4 fish C_{x-pr}	0.055	0.077	-	0.126
16 fish C_{x-pr}	0.045	0.161	0.032	0.238
4 fish C_{x-s}	-0.049	-0.046	-	-0.046
16 fish C_{x-s}	-0.156	-0.147	-0.125	-0.091

TABLE 3.2: Pressure and viscous components of the 4 and 16 fish wide schools

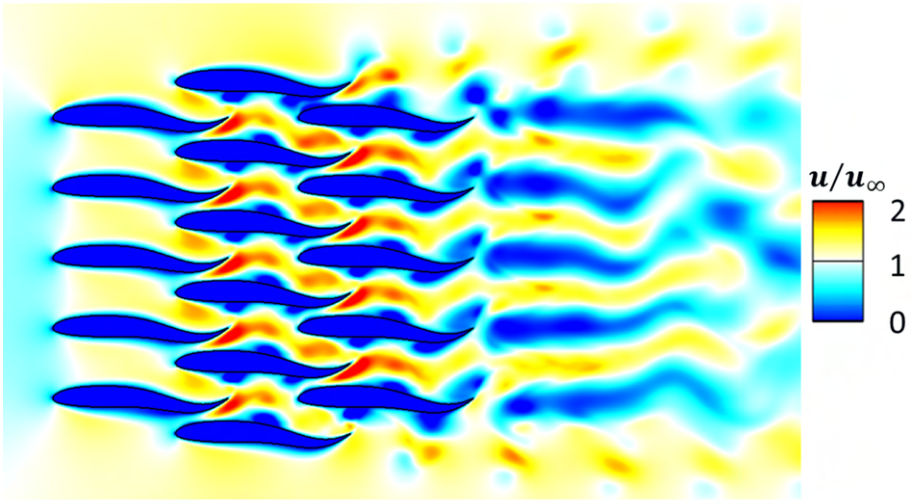

FIGURE 3.11: Instantaneous streamwise velocity for the 16 fish wide school at t/T = 1.0

To better understand the effects of swimming in a wide school, the streamwise body forces are further decomposed into their pressure and shear components in Table 3.2. In the table, the limiting pressure thrust generation in the middle of the 16 fish school

is observed. Additionally, a significant increase in the shear components of the force in the front and edge fish is observed in the 16 fish school. To understand better, the instantaneous streamwise velocity is plotted in Fig. 3.11. In the figure. the wall effect jet is shown colliding within the channel. Unlike the long school wall effect shown in Fig. 3.8, the jet is immediately contained within the wide school, increasing the near body velocity and increasing shear drag. Finally, the anterior body suction benefits shown in Fig. 3.8 are significantly increasing the pressure force component that is generating thrust at the back of the school.

These effects explain the performance in Fig. 3.3, where the wide schools have low net force for all but the back fish and the power consumption throughout is generally lessened, allowing for moderate efficiency benefits despite huge losses in thrust generation.

3.1.4.3 Diamond Schools

Next, the diamond school hydrodynamics are studied. The vorticity and instantaneous pressure are plotted at multiple time instances in the 16-fish diamond school in Fig. 3.12. The flow shows a similar overall structure to the 4 fish diamond school, with complex vortices trapped in the channels between fish bodies and a wake composed of a 2S core with paired vortices around it. One major difference, however, is that each layer of fish adds two pairs of vortices to the wake each cycle, resulting in a 2S + 6P wake. The part of each of the middle pairs combines a body length behind the school with the vortices around them, forming a 2S + 2P wake with single signed vortex streets

on each side.

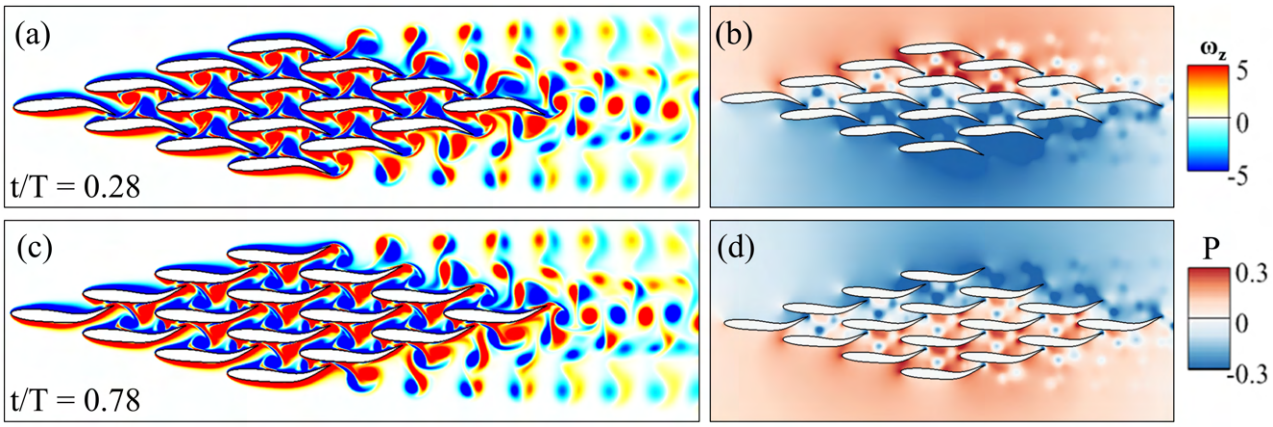

FIGURE 3.12: Vorticity (a,c) and instantaneous pressure (b,d) at t/T = 0.28 (a,b) and 0.78 (c,d) in the 16 fish diamond school.

In looking at the pressure, some smaller effects from the like sign pressure interaction from streamwise nearby swimmers are demonstrated in the long schools that appear to be present. In addition, the opposite sign pressure cancellation from spanwise nearby swimmers demonstrated in the wide schools is also present, particularly in the center of the school. This manifests in more successful positive and negative pressure differential generation throughout the school, without the dissipation of pressure in the wide school or over-combining of pressure differentials in the longer school that become problematic for power consumption. This results in the performances shown in Fig. 3.3(c). The middle fish in the school do not suffer the high power consumption costs from a long school, moving them into the high efficiency high net force zone B. Additionally, the scaling of the school is more successful without the detriment to the net force on the edges of the school present in the long schools in Fig. 3.3(a).

3.1.4.4 Comparison of Arrangements

Finally, a comparison is made between each arrangement method to draw some conclusions about the physics and results presented. The forward force along the body, averaged over a cycle and averaged between the fish within each classification (front, edge, middle, and back) are presented for the 25 fish long, wide, and diamond schools in Fig. 3.13. In the figure, each body is segmented into 10 parts, and the force is summed over a cycle for each part. Positive, thrust-producing forces are shown in red, and negative, drag-producing forces are shown in blue. The forces are plotted along the body length, shown on the x-axis.

In the figure, the thrust generation benefits at the tail portion of the body are immediately apparent in the long school. This persists through the front, edge, middle, and back fish, each receiving the constructive pressure interaction benefit brought about by the synchrony and formation of the school. The opposite is also true for the wide schools, where the latter half of the bodies of each fish produce significantly less thrust compared to the long and diamond schools. The pressure reduction from the synchrony and lateral formation reduces the thrust generation at the tail. The wide schools end up with much lower net force despite the significant increase they experience in the anterior body suction. This results in the largest performance gap within a school formation, because only the middle, edge, and back fish benefit from anterior body suction, the front fish still suffer lower thrust production in the wide school and end up with significantly reduced net force, even compared to a solo swimmer.

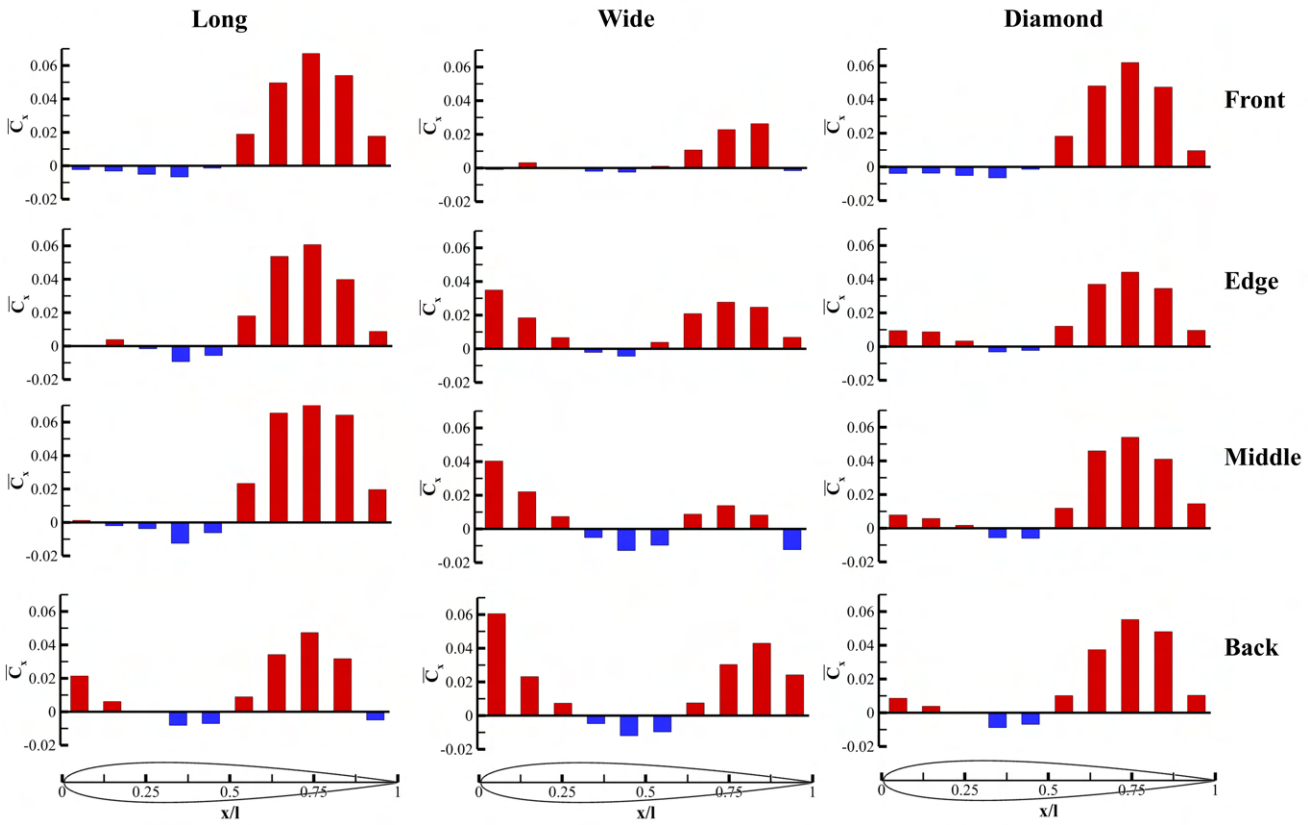

FIGURE 3.13: Cycle averaged forward force ($\overline{C_x}$) for the long, wide, and diamond 25 fish schools. Forces are averaged over all fish in the same classification and results are grouped in 10% body length increments. Thrust-producing forces are shown in red and drag-producing forces are shown in blue.

The wakes of each school formation are significantly different, with varying degrees of paired vortices shed off from the sides of the school before reaching the back fish where single vortices are formed. At the back of each school, however, a 2S pair (or in the wide school a continuous street) is shed. The individual wakes can be observed in Figs. 3.5, 3.10, and 3.12. A schematic of the 2S wake core from each school is shown in Fig. 3.14. The figure shows a wake schematic using red for counterclockwise rotating vortices and blue for clockwise rotating vortices at the back of the schools. In the schematic, the long school presents a classic thrust-indicating reverse von Karman

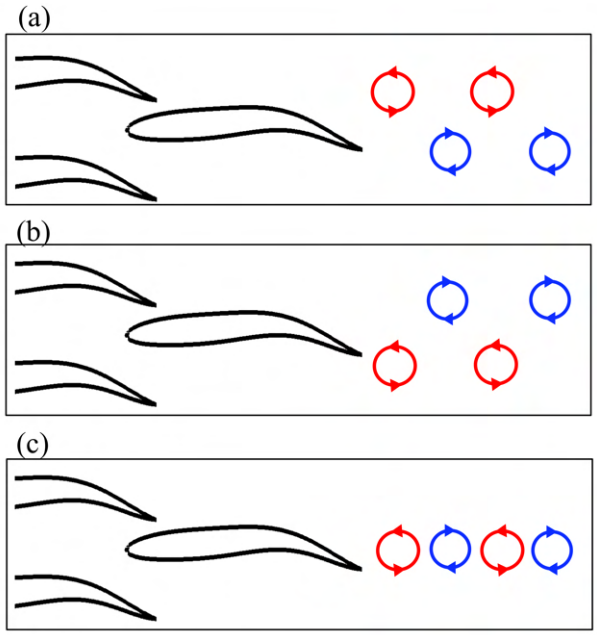

FIGURE 3.14: Schematic of the 2S wake core from the long (a), wide (b), and diamond (c) schools.

vortex street, where the channel directly behind the fish has vortex components pointing downstream, indicating net momentum transfer in that direction. The wide school presents a drag-indicating von Karman vortex street, where the channel behind the fish has vortex components pointing upstream, suggesting the opposite. Finally, the diamond school has a balanced 2S wake where the vortices appear approximately in line. These wakes correspond with the performance of the schools, where the long school is the most thrust-producing and the wide school is drag-producing. Interestingly, the wake is not indicative of the performance of the back fish in each school. The back fish of the wide schools produce the most thrust, whereas the back fish of the long school produces the least thrust of the three. This suggests that in the case of these schooling arrangements, the 2S wake shape is more indicative of the school performance as a whole than it is of the individual fish from which it shed.

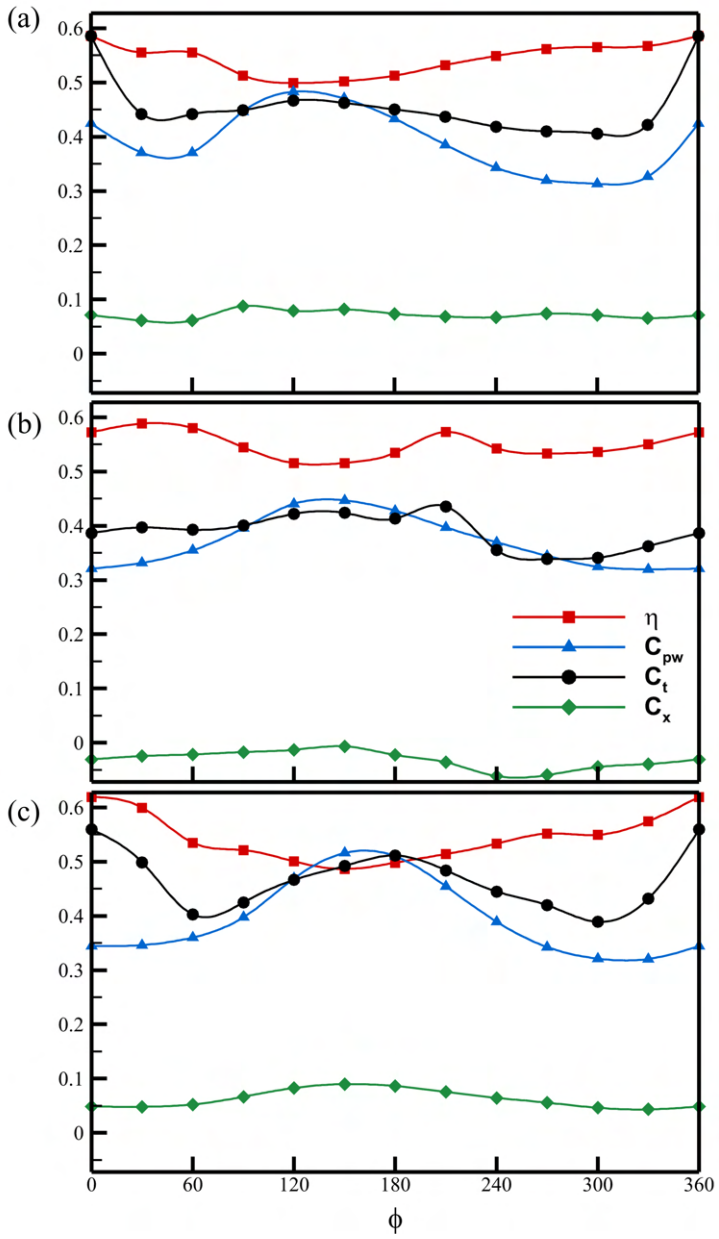

FIGURE 3.15: η, C_{pw}, C_t, and C_x for each phase lag (ϕ) in the 25 fish long (a), wide (b), and diamond (c) schools.

Much of the discussion has focused on the effect that synchrony has in limiting the performance of long and wide schools in different ways. To ensure our study encapsulates the highest performance schools, a phase study is completed using the 25 fish long, wide, and diamond schools. To define a phase that can be studied simply with a system with 25 swimmers, a phase lag is used. To apply the phase lag, the fish in each

subsequent layer of fish in the school gain some phase lag ϕ compared to the layer before. This means all fish with the same streamwise head position will still be in-phase, but each drop back in the school in streamwise position incurs a phase of $+\phi$ compared to the current streamwise head position fish. The results from this study are presented in Fig. 3.15. From the figure, it is immediately evident that for each formation changing the phase is not a viable option for improved performance in the larger schools. Despite causing limitations based on pressure interactions, the beneficial dense synchronous schooling interactions from prior research [15], [23] are no longer present as the schools move to less synchronous arrangements. This is particularly evident in the power consumption, which is at a minimum in all three schooling formations when the motion is in synchrony, ie, $\phi = 0$. The relative gain from the thrust increase that occurs for the wide school in antiphase arrangements is thwarted by the increase in drag, resulting in lower overall body force along with the increased power consumption making the phase-changed arrangements a less optimal schooling option.

Overall, the diamond arrangement provides the most balanced benefits throughout the school. The net force stays within a small range for the diamond arrangements, indicating a formation that requires less total force from outside control to maintain formation in a free swimming setting. Additionally, the efficiency benefits are observed for 90% of the schooling swimmers, as opposed to 66% in the long school and 45% in the wide school. In the wide and long formations, some fish must sacrifice their performance for the performance of the overall school. For applications where the efficiency of each fish in the school is important, the large diamond offers the most

efficiency and the most balanced performance throughout the school.

3.1.5 Section Summary

The effects of swimming in large schools with different arrangements of the school, school size, and synchrony are studied in this chapter. Our results find that the mechanisms from the elongated school in Kelly et al. [15] of the block effect, wall effect, and anterior body suction effect are still present in alternate arrangements of these large schools. Additional analysis of the long schools revealed a thrust-enhancing but power-expensive mechanism that occurs due to the synchrony of the school in the elongated arrangement. The high and low-pressure sides in each fish interact constructively with these regions generated by other fish, leading to a large buildup of high and low-pressure on each side of the school over each cycle. The wide schools find the opposite effect, where the synchrony and lateral arrangement lead to opposite sign pressure interactions that provide a lower force production, compensated by a boost in power savings. The diamond school suffers each of these effects, which cancel out well enough to provide some increase in thrust production without a significant increase in power consumption. Finally comparing the wakes, forces, and efficiencies from each arrangement. The shape of the 2S wake core is found in these arrangements to be indicative of the school's performance as a whole more than the performance of the individual fish it is shed from. Finally, it is concluded that the diamond formations offer the highest average performance as well as the most distributed benefits throughout the school where all fish gain from the schooling interaction.

4 Hydrodynamics of Multiple Fish Subgroups

To examine the hydrodynamic impacts of fish swimming in multiple smaller subgroups, fish-like undulating foils are studied numerically in in-line formations of dense subschools. Each of these subgroups are made up of synchronous diamond schools. The interaction with the complex wake generated by the front subgroup is varied by changing the streamwise spacing between the subgroups and by changing the lateral spacing in the second subgroup. Maximizing beneficial wake and body interaction allows for up to 25% increase from the diamond school average. The school average efficiency improves by as much as 7% over the diamond school. Disadvantageous interaction is still possible. Some arrangements cause a drop in efficiency and forward force production. The interaction between subgroups is found to have three main components for enhancing or destructing performance. First, capturing the central 2S core of the front diamond's wake by the front of the second group is critical. Constructive interaction with the body shear layer enhances school performance. Next, increasing the pressure between schools via a block effect allows for some performance benefits for the front subgroup. Benefits must be balanced with the destructive effects to the

second subgroup. Finally, capturing the 2P pairs on the edge of the front diamond's wake allows for high efficiency despite the lower density of the following subgroup.

4.1.1 Problem Statement

To arrange the fish in each subgroup in a basic schooling configuration that maximizes interaction, a dense diamond formation is utilized. The diamond formation has been utilized in a large range of schooling studies for its high energy efficiency [15], [26], [52], [94]. Additionally, Pan et al. [23] show that the dense spacing with 0.4l spacing between fish maximizes the beneficial interactions within the school and produces a complex 2S+2P structured wake. This allows it to be used as a generator for complex wakes in this study of subgroups interacting with fish school wakes. The basic dense diamond arrangement is shown in Fig. 4.1 for each subgroup. The fish in each subgroup are numbered to facilitate discussion. The spacing between the subgroups (G), along with the lateral spacing of the back subgroup (D), are varied in this study as the wake capture from the front subgroup is observed. These parameters are also labeled in Fig. 4.1.

The base subgroup shape of a four-foil dense diamond is shown in Fig. 1b, where c is the chord length, S is the streamwise spacing, G is the streamwise gap between groups, and D is the lateral spacing. Keeping consistent with the previous work of Pan et al. [6], we use a c value of 1, an S value of 0.4, and D and G values of 0.4 initially. In this study, both G and D are varied in the second subgroup, along with changing the orientation of the second subgroup.

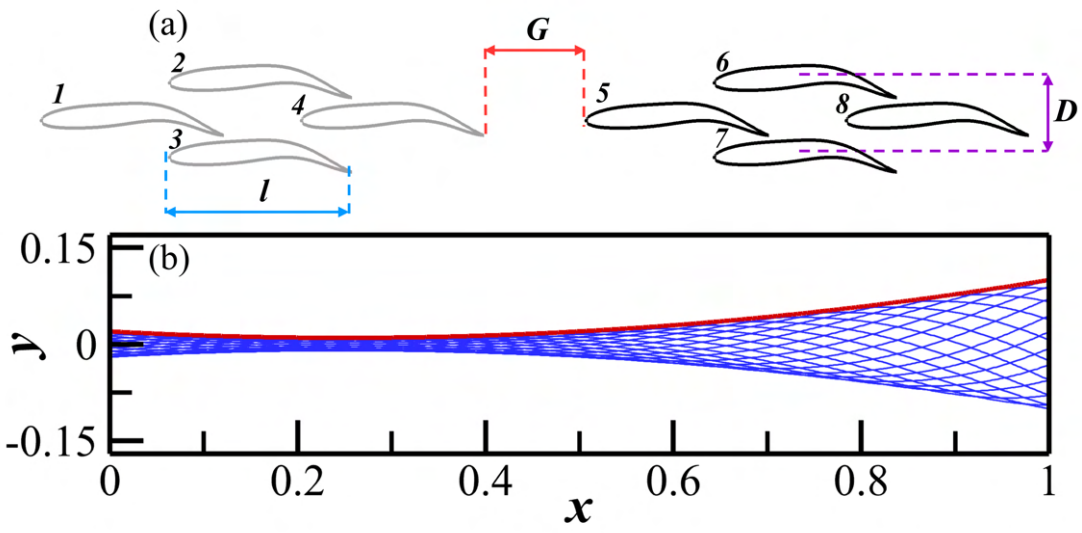

FIGURE 4.1: (a) Schematic of the fish arrangement, with the body length (l), gap between subgroups (G) and lateral spacing of back subgroup (D) indicated. Fish-like swimmers are numbers are indicated.

Continuing with typical two-dimensional fish swimming studies, the standard NACA0012 foil shape will be utilized as a baseline shape for fish-like carangiform swimmers [23], [77]. Traveling wave kinematics are imposed on the foil to give carangiform undulatory motion. The motion follows the equation:

$$y(x,t) = A(x)\sin(\frac{2\pi}{\lambda}x - \frac{2\pi}{T}t) \tag{4.1}$$

where x and y are normalized by the body length of the foil, giving the head of the fish at $x = 0$ and the tail at $x = 1$. The value of $y(x,t)$ corresponds to the lateral deviation of the body of the foil from the original foil chord. T is the period of the traveling wave, and λ is the wavelength of the wave. $A(x)$ denotes the amplitude of the lateral motion and is expressed as a quadratic polynomial given by:

$$A(x) = a_2 x^2 + a_1 x + a_0 \tag{4.2}$$

where the coefficient values are chosen to be $a_2 = 0.02$, $a_1 = -.08$, and $a_0 = 0.16$, matching the carangiform swimimng motion found in Vidler et al. [95]. This method has been used extensively for reproducing biological swimming motion [100]. The resulting amplitude and midline motion can be seen in Fig. 4.1(b).

4.1.2 Simulation Setup

A schematic of the non-uniform Cartesian grid and boundary conditions used in the simulation is presented in Fig. 4.2. The computational domain size is chosen to be $20l \times 10l$ with 1696×704 grid points, approximately 1.2 million in total. The minimum grid spacing is 3.5×10^{-3}l around the fish bodies. This grid spacing is consistent with section 3, and a grid independence study for this grid spacing is shown in Fig. 3.2. The fish are swimming to the left, with a constant incoming flow velocity of U_∞ at the left-hand boundary. An outflow boundary condition is assigned to the right-hand side and zero gradient boundary conditions on the lateral boundaries. All boundaries are treated with a homogeneous Neumann boundary condition for pressure.

In this work, two key dimensionless parameters, Reynolds number (Re) and Strouhal number (St) describe the hydrodynamic characteristics of the flow. Reynolds number is defined as $Re = U_\infty l/\nu$ where ν denotes the kinematic viscosity. For this study, the Reynolds number is set to Re=1000, consistent with prior studies of 2D carangiform

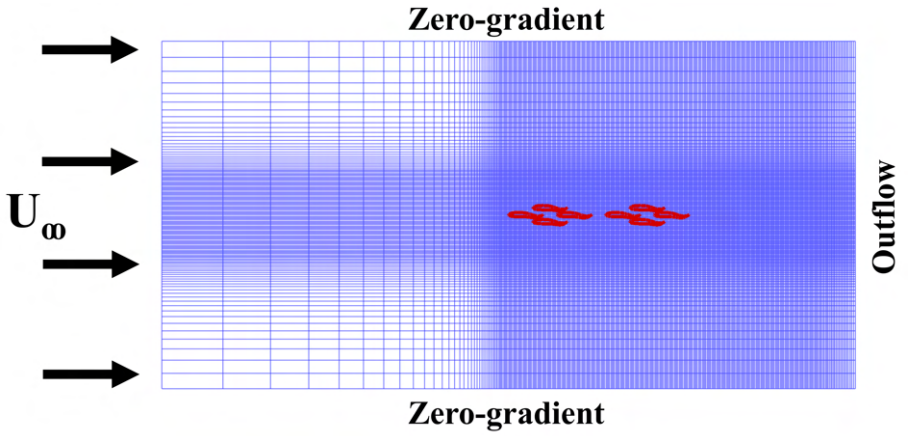

FIGURE 4.2: Schematic of the computational domain, Cartesian grid, and boundary conditions with 2 dense diamond subgroups.

swimming [15], [23], [77] and corresponding with higher Reynolds numbers in three dimensions [93]. In this flow regime, the viscous effects are small while still maintaining coherent vortex structures [81]. Additionally, it was shown in Kelly et al. [15] that in dense planar schooling, the wake structures and performance remain similar as the Reynolds number is increased. The Strouhal number is defined as $St = 2fA/U_\infty$, where $f = 1.0$ is the tailbeat frequency. The Strouhal number is set to St=0.43, which balances the thrust and drag to achieve a steady swimming condition of a net-zero force over a cycle of motion. This gives an incoming velocity of $U_\infty = 0.465$ l/cycle. Details on the Strouhal number selection can be found in Pan and Dong [23].

4.1.3 Results and Discussion

4.1.3.1 Diamond School

To understand the performance changes in the second diamond subgroup and the wake that it interacts with, the study begins with a review of the diamond school performance and wake. The performance is presented in Table 4.1 compared to the solo swimmer.

	$\overline{C_x}$	$\overline{C_t}$	$\overline{C_{pw}}$	η
single fish	0.004	0.22	0.27	0.44
diamond school	0.056	0.37	0.33	0.53

TABLE 4.1: Forces, power consumption, and efficiency for a single swimmer and diamond school. Results are averaged over a cycle of motion, and the diamond school is averaged between all four fish.

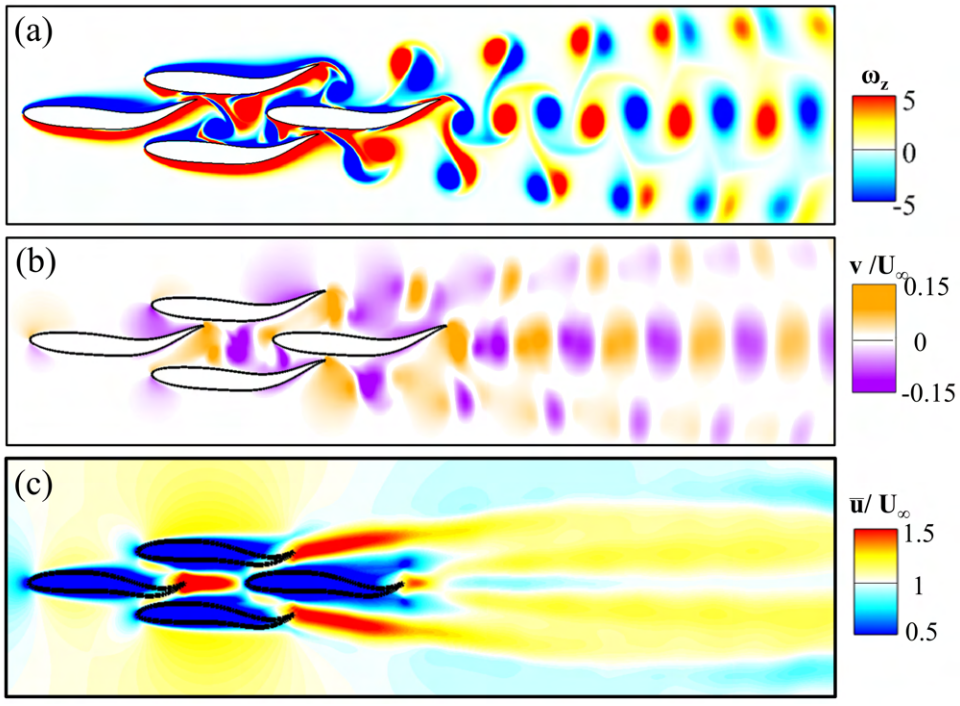

FIGURE 4.3: Vorticity (a), lateral velocity (b), and cycle averaged streamwise velocity (c) behind the 4 fish diamond school.

In the table, the benefits of swimming in a dense diamond school can be observed. The thrust produced increases by 68%, and the efficiency increases by 20%. These results serve as a baseline to compare each subgroup's performance. To better understand the wake created by the diamond school, the vorticity, lateral velocity, and cycle averaged streamwise velocity are plotted in Fig. 4.3. The wake has a von Karman wake core coming from the back fish of the school, typical of a solo fish swimming. Each of the fish on the edges of the school form a wake made of paired vortices. This results in a 2S + 2P wake, with two single vortices and two paired vortices shed each cycle of undulation. The cycle averaged velocity shows two short high-velocity angled jets coming from the edges of the school. These findings are consistent with the synchronous diamond school showed in Pan and Dong [23], [52] and serve as a baseline to understand the wake interactions in the sub-grouped schooling swimmers.

4.1.3.2 Subschooling Hydrodynamics

	$\overline{C_x}$	$\overline{C_t}$	$\overline{C_{pw}}$	η
front subgroup	0.065	0.38	0.33	0.54
back subgroup	0.057	0.38	0.32	0.55

TABLE 4.2: Forces, power consumption, and efficiency for the front and back subgroup of fish. Results are averaged over a cycle of motion and between all four fish.

First, the baseline case is compared to the diamond school. In this case, G = 0.8 and D = 0.4. The values for the cycle average force, power, and efficiency are given in Table 4.2. In the table, there is a 4% increase in the efficiency for the second subgroup and a 16% increase in the net force for the front subgroup. The thrust is not significantly changed,

suggesting that the addition of the second subgroup decreased the body drag in the first subgroup.

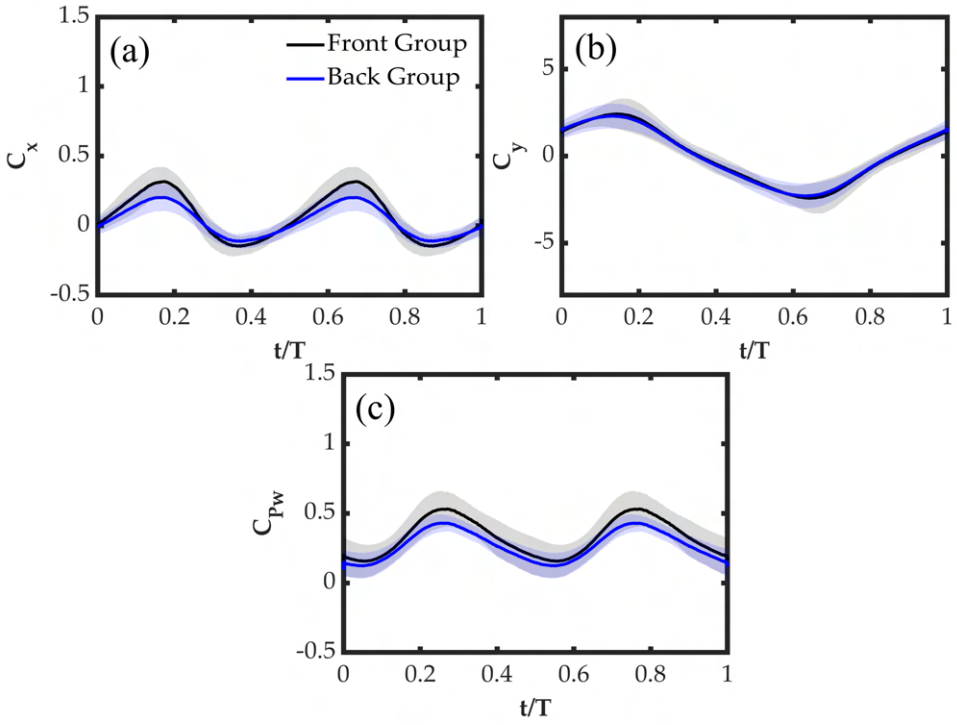

FIGURE 4.4: Forward force (C_x), lateral force (C_y), and power consumption (C_{pw}) for G = 0.8 and D = 0.4. Forces and power are averaged with each subgroup and the standard deviation is shown by the shaded regions.

The continuous forces in the x and y directions in addition to power consumption are plotted in Fig. 4.4. Typical of synchronous fish schooling, 2 distinct peaks in power and forward force are observed in each flapping cycle, along with one positive and one negative peak in lateral force. In the figure, similar lateral forces are observed between each group. However, the front group has a higher net force and higher power consumed. The standard deviation is much larger for the front subgroup in each of the three metrics.

Next, the vorticity is shown in Fig. 4.12 for t/T = 0.63, 0.81, and 1.0. In comparing

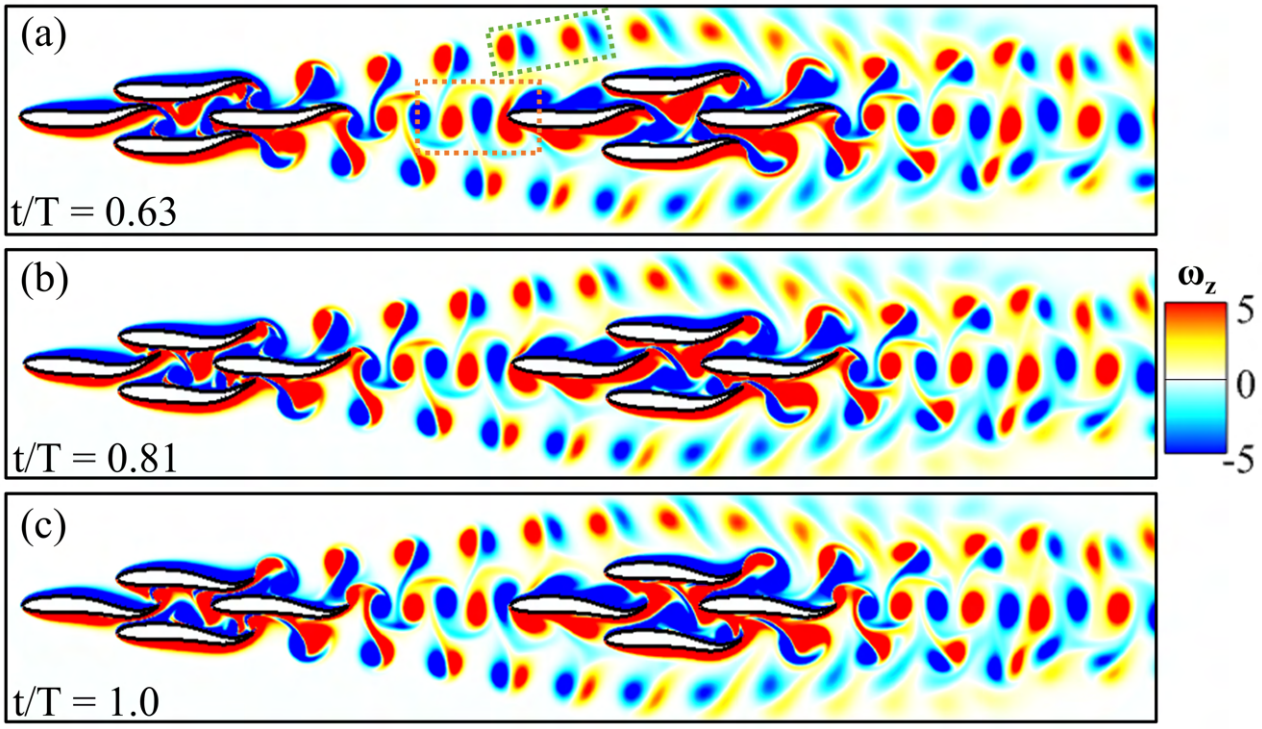

FIGURE 4.5: Vorticity around the school for G = 0.8 and D = 0.4 at t/T = 0.63 (a), 0.81 (b), and 1.0 (c).

the vortex wake with the diamond school in Fig. 4.3, we see a similar wake structure behind ths school with a 2S center wake and a 2P wake on the edges. In part (a), we note that the vortices in the 2P pair noted in green shed by the front subgroup are not captured by the back subgroup, giving evidence that a wider back subgroup may be able to better utilize the energy from the vortices shed by the front subgroup. The 2S core, however, is fully intercepted by fish 5 noted in the orange box. The shear layer along the body of fish 5 is significantly stronger and larger due to this interaction, as the time series shows the motion of fish 5's head corresponding with the interception of each vortex. This head motion synchronizes with each lateral motion of the wake (4.3(b)), maintaining a like-sign vortex interaction with this portion of the wake. Finally, the cycle averaged velocity is plotted in Fig. 4.6. In the figure, additional high

velocity jets are observed originating around the head of fish 6 and 7, where the higher velocity from the diamond school wake (4.3(c)) is interrupted by the presence of the second subgroup. Additionally, the lower velocity region directly following fish 4 is extended to reach the start of the second subgroup.

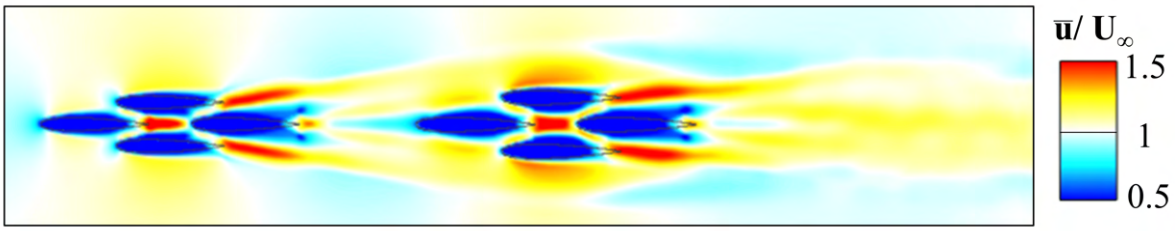

FIGURE 4.6: Cycle averaged streamwise velocity for the school G = 0.8, D = 0.4.

4.1.3.3 Variation of G and D

Next, the spacing between subgroups (G) is varied, along with the lateral spacing of the back subgroup (D). Varying the lateral spacing will manipulate the interaction with the front school wake to capture the wider spacing of the front subgroup's 2P vortex pairs. Changing the spacing between the subgroups will change the interaction with the 2S wake core. The results are presented in Fig. 4.7.

In the figure, the efficiency of the front subgroup and the net force of the front subgroup are shown to be dependent almost entirely on G. The net force increases significantly at low G values, and drops to the diamond school value at large G. The range of front subgroup efficiency values is also very small, indicating that the addition of a second subgroup has little effect on the efficiency in the first. This is consistent with Table 4.2 indication that the benefit to the front subgroup occurs due to a decrease in body drag.

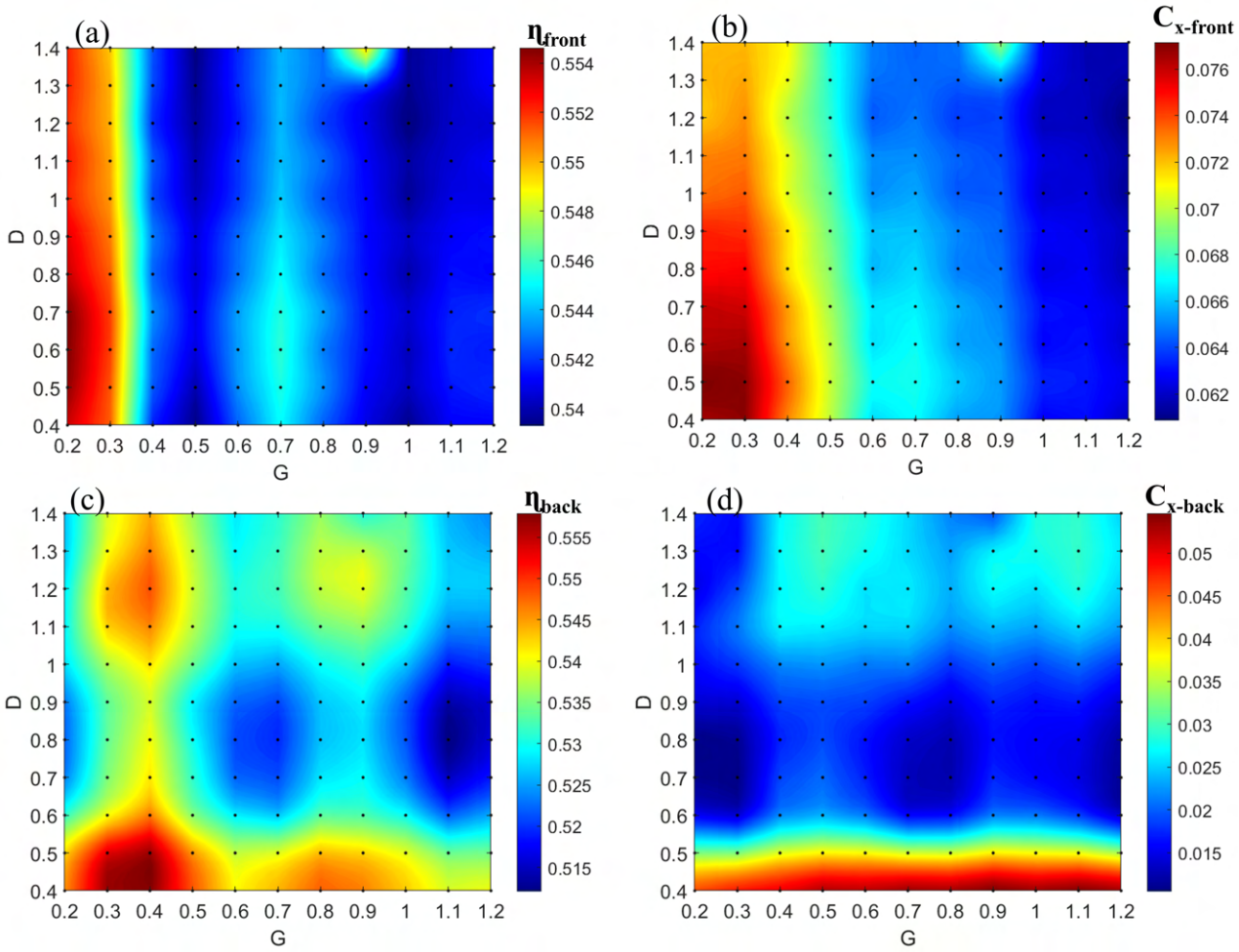

FIGURE 4.7: Front (a-b) and back (c-d) subgroup efficiency (a,c) and net force (b,d) with each case indicated by a black dot.

Next, it is seen that both D and G have a significant impact on the efficiency in the second subgroup, with a range of 8% in the efficiency occurring from small changes in the spacing. The highest efficiency occurs when both G and D are 0.4. The densest spacing provides the most beneficial interaction within a dense school, via the wall, block, and body-body suction effects detailed by Pan and Dong, and the spacing is consistent with the most beneficial found in their study [23], [101]. The next highest efficiency zones, however, occur around a D value of 1.2, where it is expected that the beneficial dense school interactions are at a minimum within the back subgroup.

Additionally, there is another pair of higher efficiency zones at G = 0.8 to 0.9 at D values of 0.4 and 1.2, creating another vertical band of increased performance. Finally, the net force in the back subgroup is mostly dependent on D. This is consistent with the lateral spacing results from Pan et al. [101]. In addition to this highest net force zone, there are multiple regions of much lower net force around D values of 0.7 at G values of 0.3, 0.8, and 1.2. The figure indicates that subgroup interactions can increase the school average efficiency by as much as 26% over a single swimmer, and by 7% over the diamond school average. Disadvantageous interaction is still possible, however, with a 4% drop in school average and 17% drop in a single fish efficiency possible compared to a diamond school average. Similar drops in the net force produced in a school are also possible.

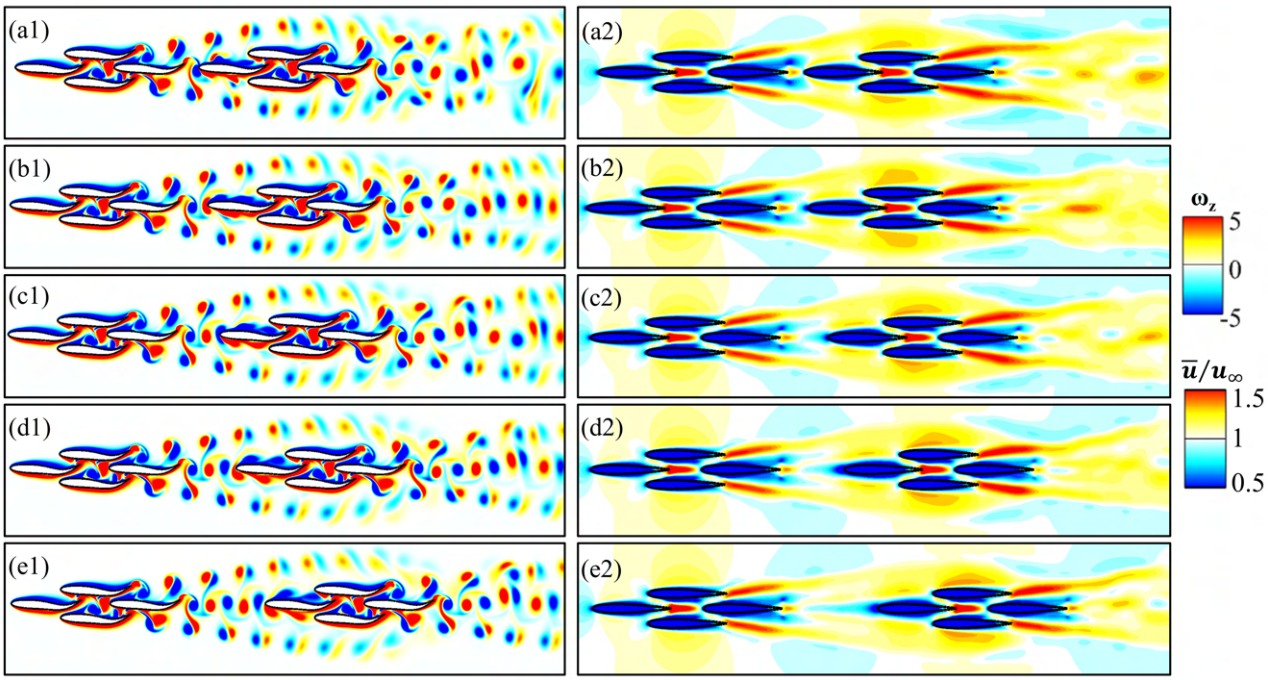

FIGURE 4.8: Vorticity (1) and cycle averaged streamwise velocity (2) for G = 0.2 (a), 0.4 (b), 0.6 (c), 0.8 (d), 1.2 (e) at D = 0.4.

The vorticity for G = 0.2, 0.4, 0.6, 0.8, and 1.2 along D = 0.4 is shown in Fig. 4.8, including the efficiency peaks at 0.4 and 0.8, and the lower performing cases between. Across each of the cases, the typical 2S core and 2P vortex pairs are observed in the wake, corresponding to short jets on the edge of the school in the velocity average. The primary difference in the near-body vortices with the change in G is observed along the shear layer of fish 5. As the 2S wake core from fish 4 intersects with the body of fish 5, there is constructive and destructive interference with the shear layer depending on the spacing. In the highest performing cases (b1, d1), there is primarily constructive interaction and subsequent enhancement in the shear layer of fish 5 from the wake of fish 4. With the lower-efficiency spacing, there are significant amounts of destructive interaction and interruption of the shear layer along the body of the fish. The effect of this can be seen in Fig. 4.9, which shows the net force and power consumption over a cycle of motion for G = 0.4 and G = 0.6 at D = 0.4 in fish 5. Both the thrust enhancement and power reduction are seen, particularly at t/T = 0.25 and 0.35 respectively, along with t/T = 0.75 and 0.85 due to symmetry.

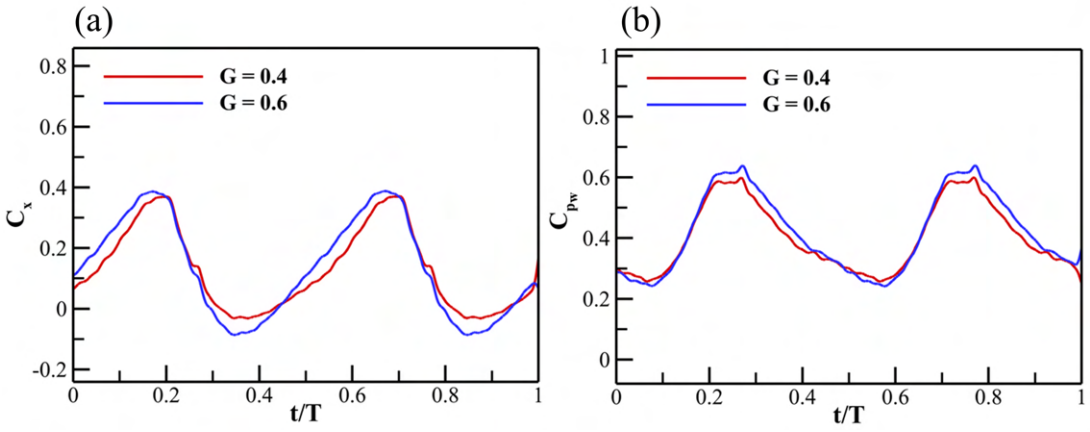

FIGURE 4.9: Coefficient of forward force (a) and power (b) for G = 0.4 and 0.6 at D = 0.4.

The performance benefit due to this interaction occurs because the wake from fish 4 is repeated, such that the oncoming vortices are similar by moving the second subgroup back by the distance between two of the same sign vortices in the wake. For an incoming flow speed of 0.46l and a frequency of 1, this corresponds to a spacing of 0.46l. The vertical bands in Fig. 4.7 are attributed to this, and the spacing of 0.4l in the figure is very close to the 0.46l attributed to the wake. Should the study continue to G = 1.4 and beyond, it is predicted that the pattern repeat as the constructive wake interaction continues. Streamwise spatial changes resulting in a banded structure in the efficiency from similar interactions with a repeating wake have also been observed in the interaction of multiple foils, as presented in Boschitsch et al. and Pan et al. [52], [76].

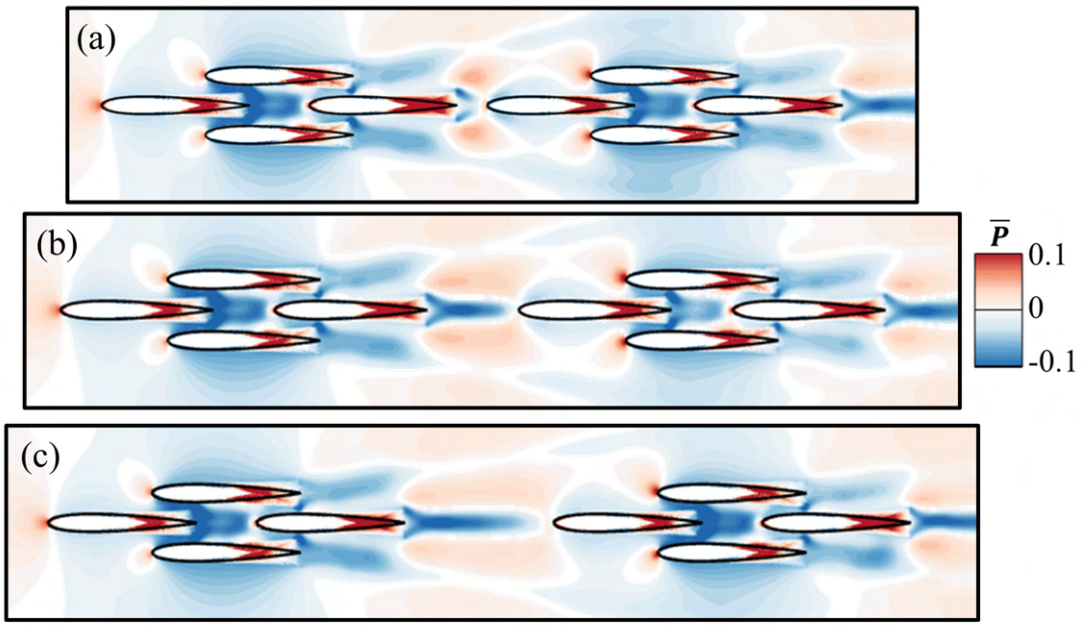

FIGURE 4.10: Cycle averaged pressure contour for G = 0.2 (a), 0.4 (b), and 0.6 (c) at D = 0.4.

The cycle averaged pressure at G = 0.2, G = 0.4, and G = 0.6 for a D value of 0.4 are

shown in Fig. 4.10. In the figure, a low-pressure zone exists between the schools in the G = 0.4, is larger at G = 0.6 cases, but in not present at G = 0.2. The presence of the second subgroup partially or fully interrupts this low-pressure region, increasing the pressure between the subgroups. This closer proximity increased pressure decreases some of the drag-producing suction that occurs at the back of fish 4. Similar effects have been reported previously [76], [102], showing that in a two-body system at very small streamwise spacing, drag reduction and thrust enhancement result from an increase in the pressure between the bodies. These results are also very similar to the block effect previously reported in dense diamond fish schools [15], [23]. The results indicate that a similar thrust enhancement occurs between subgroups within a larger school with small streamwise spacing between the subgroups.

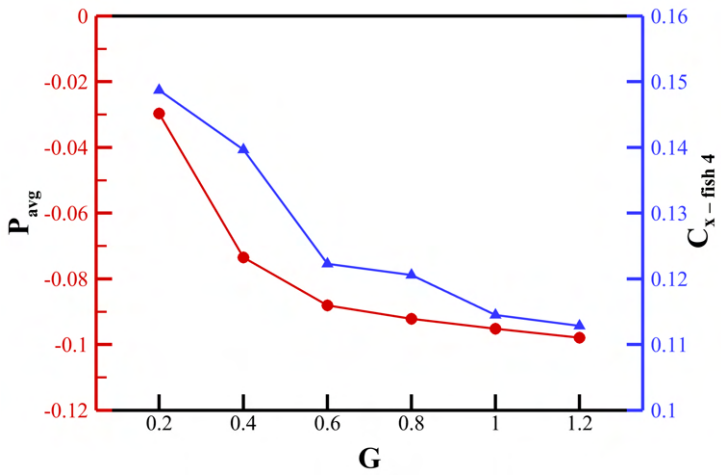

FIGURE 4.11: Cycle averaged pressure 0.1l behind fish 4 and net force of fish 4 plotted against G for D = 0.4.

To get a clear picture of this effect and how it impacts the net force on fish 4 at each G spacing, the cycle averaged pressure at 0.1l behind fish 4 and the net force of fish 4 are plotted against the spacing G in Fig. 4.11 for a D value of 0.4. In the figure, the change

in pressure correlates very well with the change in net force observed. This further increases the evidence that the pressure increase is responsible for the drag reduction when the space between groups is small.

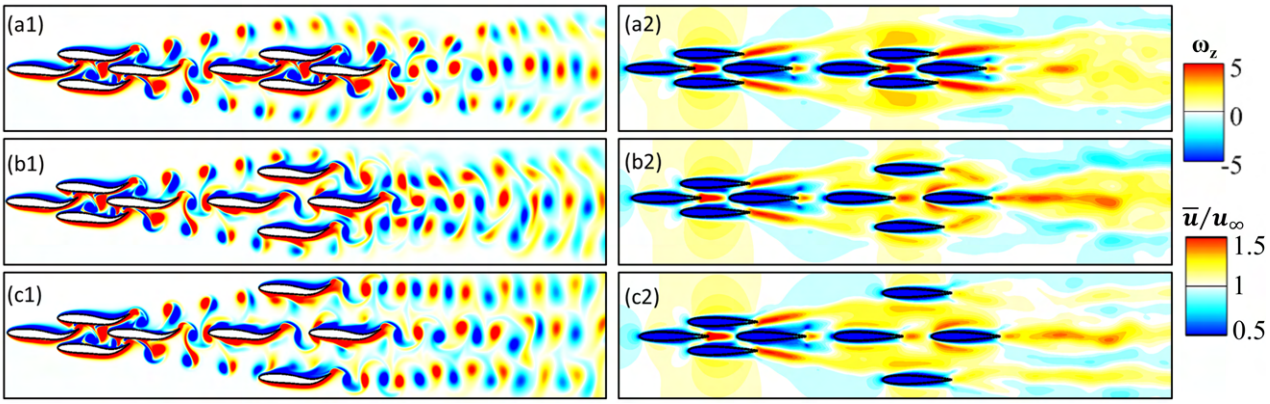

FIGURE 4.12: Vorticity (1) and cycle averaged velocity (2) for D = 0.4 (a), 0.8 (b), and 1.2 (c) at G = 0.4.

Next, the vorticity is shown for D = 0.4, 0.8, and 1.2 at G = 0.4 in Fig. 4.12. At D = 0.4, the wake behind the second subgroup has the same structure as the diamond school, with a 2S core and 2P pairs of vortices on either side. The school intersects the 2S pair from fish 4, while completely missing the 2P pairs which move laterally around the subgroup. In the medium width D = 0.8, the 2P pairs from the front school are partially captured by the outer fish in the second subgroup. The vortices destructively interfere with the shear layer of that fish. The resulting wake begins with a 2S pair behind each of the outer fish but transitions to a 2P pair farther downstream. At D = 1.2, the 2P wake pair from the front subgroup is captured on the inside of the outer fish. This creates constructive interference with the shear layer. The resulting wake is wider, with 3 sets of 2S pairs.

The effects of the vortex interactions can be seen in Fig. 4.13, which details the net force

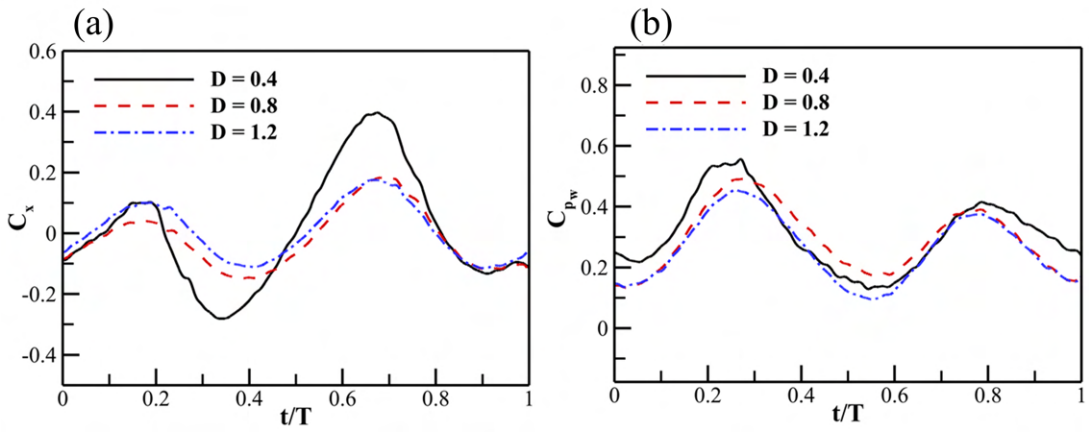

FIGURE 4.13: Coefficient of forward force (a) and power (b) for D = 0.4, 0.8, and 1.2 at G = 0.4.

and power consumption in fish 6 over a cycle of motion. In the figure, the higher power consumption and net force resulting from denser schooling interactions are seen at D = 0.4, whereas D = 0.8 and D = 1.2 have more consistent results with smaller peaks and troughs and are lower in both power consumed and net thrust generated. The main difference between the latter two occurs when the fish is flapping outward from the school. The shear layer enhancement gives both a power and a thrust benefit at D = 1.2.

4.1.4 Section Summary

Two-dimensional numerical simulations have been conducted to study the interaction between two subgroups of fish-like swimmers in dense diamond formations. It is shown that the addition of a second diamond subgroup enhances the performance of both subgroups, with the back subgroup primarily gaining efficiency while the front

subgroup primarily increases in the net force. The wake structures within the two-subgroup system are identified, and two primary vortex capture mechanisms are identified for enhancing the efficiency in the second subgroup. First, changing the spacing between the subgroups showed enhancement of the shear layer via constructive interference with the center wake of the front subgroup led to better performance in the back subgroup. This creates a repeating high-efficiency zone based on the spacing of the subgroups. Second, high efficiency in the second subgroup can be achieved either by swimming compactly to maximize the interaction within the subgroup or in a wider formation to fully capture the wake of the front subgroup such that the shear layer of the outside pair is enhanced by the wake interaction. The improvement in performance for the front subgroup was shown to occur due to the thrust increase that results from the proximity of the two subgroups, and the advantage dissipates as the spacing between subgroups increases. Overall, the efficiency gain in the second subgroup is shown to be heavily dependent on both the lateral spacing of the subgroup and the space between groups. This ranges from 7% efficiency gains in the subgroup to a negative effect on efficiency from swimming in a subgroup in the worst cases. The net force benefit in the front subgroup was shown to rely solely on the spacing between the subgroups, benefiting most when they are the closest together.

5 Body Shape Effects in Bio-Robotic Platform

5.1 Shape Effects in Tail-like Propulsor

During the undulation motion of fish-like swimming, the movement of the caudal fin can be approximated by a flapping foil, as demonstrated in Fig. 5.1. This study focuses on understanding how the cross-sectional shape of a caudal fin affects propulsive performance. To achieve this, two-dimensional numerical simulations of fluid flows around flapping foils are studied. By varying the foil shape using a class-shape transformation method, we investigate a broad range of foil shapes. In the study, we also show consistent results with previous studies that a thicker leading edge and sharper trailing edge makes for a more efficient foil shape undergoing a flapping motion. In addition, we explain that the performance of the foil is highly sensitive to its shape, specifically the thickness of the foil between the 18th and 50th percent along the chord of the foil. Moreover, we elucidate the flow mechanisms behind variations in performance metrics, particularly focused on constructive interference between the vortices generated at the leading-edge with the trailing-edge vortex, as well as the pressure

field differences that lead to higher power consumption in less efficient foil shapes.

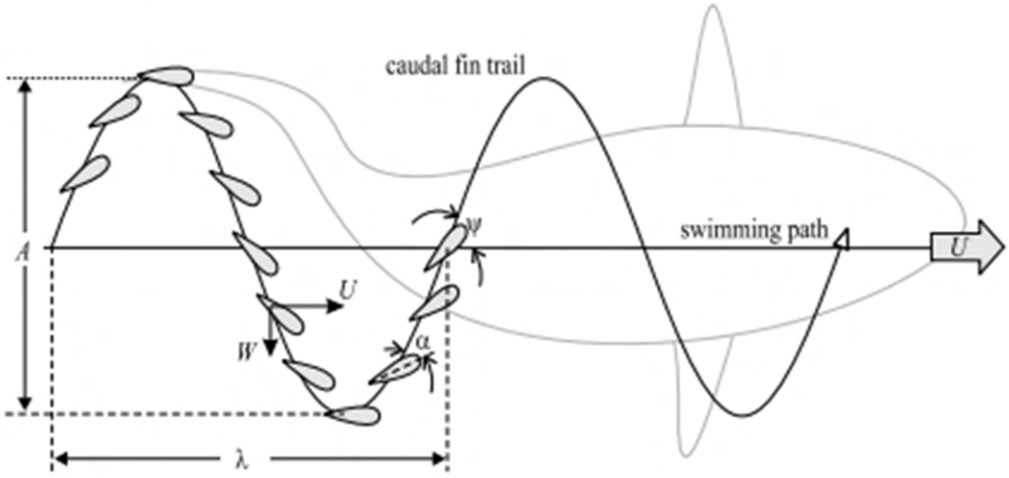

FIGURE 5.1: Pitching and heaving foil as a model for caudal fin of an undulating swimmer, reproduced from [103].

5.1.1 Problem Statement

First, we prescribe a flapping kinematics with a fixed set of kinematics for foils. The motion during a down-stroke is schematically illustrated in Fig. 5.2. Here, U_∞ denotes the free-stream velocity at the inlet, δ_{max} is the maximum thickness of the foil, S_{max} represents the distance of the location for maximum thickness from the leading-edge of the foil along its chord. Moreover, c shows the chord length of the foil, $h(t)$ is the instantaneous heaving position, $h_\circ$ is the maximum heaving displacement, and $\theta(t)$ is the instantaneous pitching angle. The following mathematical relations prescribes the flapping kinematics of a foil

$$h = h_0 sin(2\pi f t) \tag{5.1}$$

$$\theta = \theta_0 sin(2\pi f t + \phi), \tag{5.2}$$

where f is the frequency of the motion, $\theta_\circ$ is the maximum pitching angle, and ϕ is the phase angle between the pitching and heaving motions.

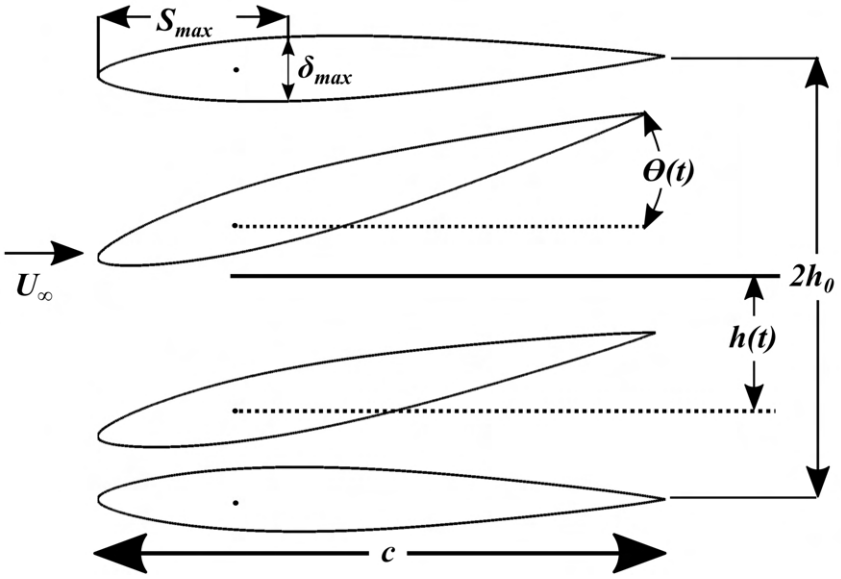

FIGURE 5.2: Definition of principal motion parameters and kinematics during the down-stroke of a NACA0012 foil

Previously, van Buren et al. [104] analyzed the effect of changing $h_\circ$, $\theta_\circ$, and ϕ on the performance of flapping foils. It was concluded that the most efficient motion occurred at $\phi = 270°$. In addition, they found that cases with $h_\circ = 0.375c$ produced the highest efficiencies. Furthermore, they found the best performance with respect to efficiency in cases with $\theta_\circ = 15°$. Therefore, these important results provide the basis for our choices of values for ϕ, $h_\circ$, and $\theta_\circ$ for our present work.

Next, the methodology for varying the shape of the foils is determined. Many previous studies focused on using standard shapes of foils, such as those belonging to NACA series. In order to ensure the capturing of a large spectrum of geometric configurations of foils, a parameterization method that allows us to fully control the shape of a foil is required. The use of such a method allows the complete exploration of the design

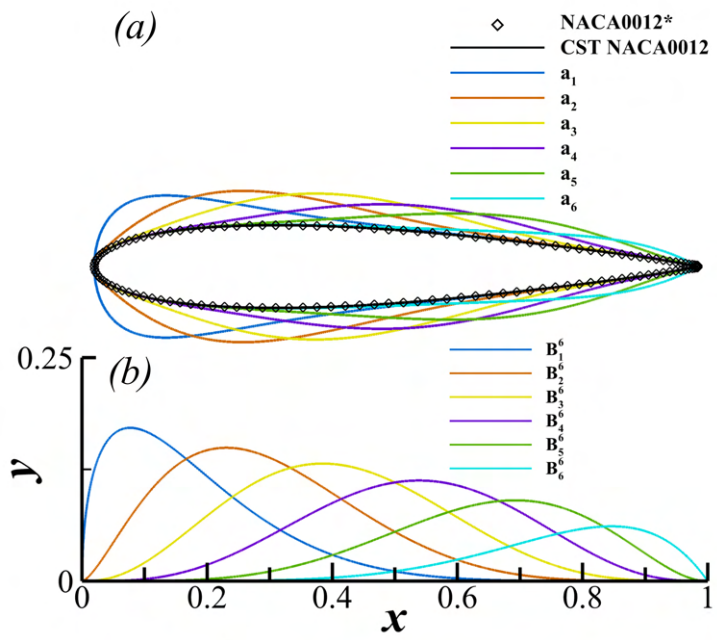

FIGURE 5.3: (a) Sample foil shapes generated by increasing each parameter individually along with the CST-generated [23] and true* NACA0012 foils [105]. (b) Basis functions of CST along the chord.

space, rather than being limited by standard series foil shapes. Reviews of the previously developed and employed parameterization methods to create better performing foils were provided by various researchers [106], [107]. In Poole et al. [106], multiple parameterization methods, including analytic method, singular value decomposition (SVD) method, class-shape transformation (CST) method, discrete method, domain element method, free form deformation (FFD) method, PARSEC method, PDE method, and Splines method are compared. While this study did not provide a recommendation for a single method as superior, it does highlight SVD and CST for being more efficient in defining foil shapes with few parameters than the others. In another study [107], B-splines, CST, SVD, and PARSEC were analyzed in more detail from the aspects of accuracy and efficiency. CST and SVD were also found to be the two most efficient methods in defining foil shapes with a less number of independent parameters.

The CST method for the parameterization of foils was developed by Kulfan et al. [108], [109]. In addition to demonstrating superior capabilities of generating foil shapes, they also demonstrated how CST could be used to form other two-dimensional (2D) and three-dimensional (3D) geometric configurations. Additionally, it was also shown that this parameterization technique will always produce a foil-like shape while utilizing the shape function for a foil. Hence, this robustness makes it a preferred candidate algorithm to perform extensive parametric studies to extract optimal shapes of foils for a desired objective function. For this study, we use a class-shape transformation method. This method was previously identified as an efficient method for varying foil shapes with a reduced number of design variables while maintaining the core shapes of foils [107], [110]. In this method, a class function is used to define the basic geometric foil shape with a round leading-edge and a sharp trailing-edge. It is then multiplied by the shape function that allows to modify the basic foil shape and generate a wide variety of different geometries. The CST-based foils are generated with the following equations:

$$y(x) = x^{N_1} \cdot (1-x)^{N_2} \cdot \sum_{j=1}^{N} a_j \cdot K_j^N \cdot x^{j-1} \cdot (1-x)^{N-j} = \sum_{j=1}^{N} a_j \cdot B_j^N, \tag{5.3}$$

$$B_j^N = K_j^N \cdot x^{j+N_1-1} \cdot (1-x)^{N+N_2-j} \tag{5.4}$$

$$K_j^N = \frac{(N-1)!}{(j-1)!(N-j)!} \tag{5.5}$$

where $x^{N_1} \cdot (1-x)^{N_2}$ is the class function, $K_j^N \cdot x^{j-1} \cdot (1-x)^{N-j}$ is the shape function,

B_j^N are the basis functions, and a_j are the CST coefficients. First, in order to give the general foil shape of a round leading-edge and pointed trailing-edge, we define $N_1 = 0.5$ and $N_2 = 1.0$. It is important to mention that the order of the Bernstein polynomial in the shape function is set to 5, which makes $N = 6$. This was determined from the work of Kulfan et al. [109] and earlier shown to be sufficient for 2D foil shapes [70], [71], [110]. This value of N implies that we have 6 parameters that are used next to determine the foil shape $a = (a_1, a_2, ..., a_6)$, where a_j are the parameters corresponding to Equation (3) and a is the vector used to denote all these parameters. Shown in Fig. 5.3(b) are the basis functions for the CST with $N_1 = 0.5$, $N_2 = 1.0$ and $N = 6$. It can be observed that each function corresponds to a different locations of peak values along the chord. This particular feature enables the manipulation of thickness in each region. It is made possible by increasing or decreasing the value of a coefficient with the basis function that peaks in the corresponding region. Fig. 5.3(a) illustrates this process through an example, where each coefficient is increased about 10% from the NACA0012 value to vary the foil shape. We notice that using a larger coefficient values make the resulting foil thicker in the regions where its basis function is the largest. Additionally, the CST-generated NACA0012 foil, the values of which are given in Han et al. [110], is shown alongside the actual NACA0012 foil. This confirms that the CST method accurately portrays this foil shape using $N = 6$.

5.1.2 Simulation Setup

The Cartesian computational grid used for our current simulations is shown in Fig. 5.4(a). The domain size is $16c \times 14c$, and the total grid contains about $954{,}000$ (993×961) nodes. To accurately capture the foil geometries and flow boundary layers, an extremely dense region is assigned around the foil with a minimum grid spacing of $\Delta_{min} = 0.00227c$. Outside this layer, a grid with resolution $\Delta_{mid} = 0.0125c$ is generated to resolve the wake features behind the flapping foil with sufficient accuracy. To exclude the effects of the grid on the hydrodynamic force calculation, grid independence study, shown in Fig. 5.4(b), is performed on three sets of grids with different minimum grid spacing, $\Delta_{Coarse} = 0.00468c$, $\Delta_{Nominal} = 0.00227c$, and $\Delta_{Fine} = 0.00175c$, with a NACA0012 foil undergoing previously defined kinematics. From this grid study, the difference between the mean thrust coefficients obtained from the nominal and fine grids is 0.98%. Furthermore, the difference in the maximum thrust coefficients from the nominal and fine mesh is 1.15%. Hence, it is adequate to use nominal grid for our simulations.

To set up the flow in the computational domain, the left boundary is set to a velocity inlet with a constant incoming flow speed of $2.5c/T$. A zero-gradient boundary condition is considered to the upper and lower sides, and a zero stream-wise gradient is prescribed to the outlet on the right side, as shown in Fig. 5.4(a). A homogeneous Neumann boundary condition is used for pressure at all boundaries.

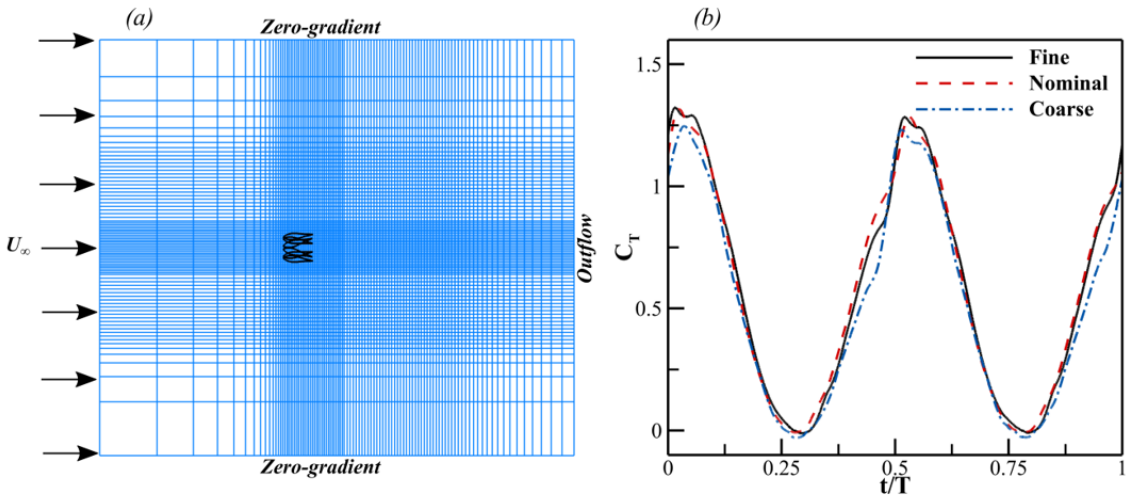

FIGURE 5.4: *(a)* Schematic of the computational domain, Cartesian grid, and boundary conditions. *(b)* Comparison of instantaneous thrust coefficients for a NACA0012 foil obtained through coarse, nominal, and fine grids

To quantify the hydrodynamic performance, the coefficients of thrust and power are defined as

$$C_T = \frac{F_x}{0.5\rho U_\infty^2 c^2} \tag{5.6}$$

$$C_{Pw} = \frac{Pw}{0.5\rho U_\infty^3 c^2}, \tag{5.7}$$

where F_x is the stream-wise force experienced by the foil and ρ is density of the fluid. Also, the propulsive efficiency is defined as

$$\eta = \frac{\overline{C_T}}{\overline{C_{Pw}}}, \tag{5.8}$$

where $\overline{C_T}$ and $\overline{C_P w}$ are the cycle-averaged coefficients of thrust and power, respectively.

The flow conditions for this study are described using two dimensionless parameters, the Reynolds number (Re) and the reduced frequency (f^*), where the reduced frequency is given by the following equation.

$$f^* = \frac{fc}{U_\infty} \tag{5.9}$$

In our current study, we consider a baseline of $Re = 10{,}000$ and $f^* = 0.4$, which corresponds to a Strouhal number of $St = 0.3$, given by the following equation

$$St = \frac{fA}{U_\infty}, \tag{5.10}$$

where $A = 2h_0$ is the peak to peak trailing edge amplitude. These values are aligned with the previously studies [70], [110] and lie within the operating range of natural swimmers [111], [112].

5.1.3 Results and Discussion

In this section, we explain our findings for varying shapes of foils, their performance metrics, and the governing flow physics.

5.1.3.1 Hydrodynamic Efficiency

First, we perform simulations for flows over flapping NACA0012 foil generated with the CST technique shown in Fig. 5.3. To understand the impact of each coefficient

on the foil's performance, we then change a single CST coefficient while holding the remaining ones for the conventional NACA0012 profile, resulting in a range of foils similar to Fig. 5.3. The shapes are varied to find the peak efficiency for each coefficient. In order to better compare the results to the NACA0012 foil the shapes originate from, the relative efficiency is shown. This is computed as $\eta_R = \frac{\overline{\eta}}{\eta_{NACA0012}}$. Additionally, we utilize these coefficients from the optimized foil reported in Ref. [110] to ensure that the current range of coefficients include the ones with maximum η for each coefficient.

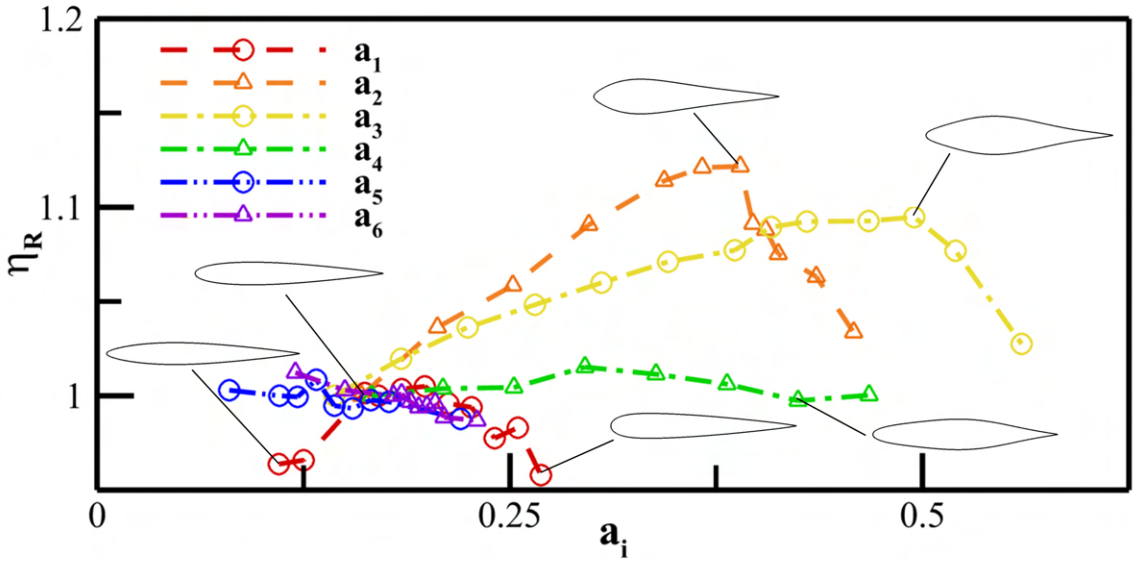

FIGURE 5.5: Values of coefficients versus η_R computed by varying a single coefficient at a time, with the other coefficient values fixed at the values for NACA0012 profile.

The results shown in Fig. 5.5(a) exhibit η for each case, normalized by the propulsive efficiency of a NACA0012 foil with the varying values of coefficients. It is important to highlight that a_5 and a_6 have a very narrow range of η, and are best around the values for a NACA0012 foil. This aligns with our hypothesis and previous studies showing that a geometric configuration with a thicker trailing-edge and without a thicker

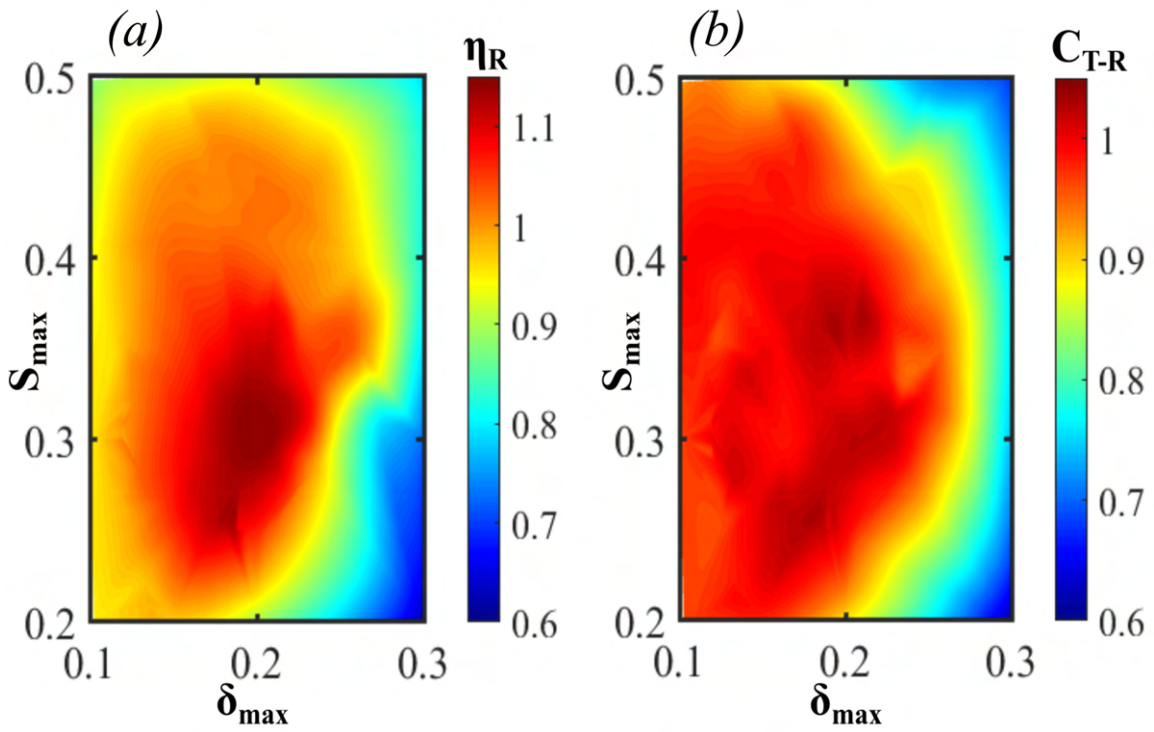

FIGURE 5.6: Contour plots of efficiency *(a)* and thrust *(b)* vs Maximum thickness and Maximum thickness location for all of the shapes used in this study.

leading-edge is inefficient [110]. Looking at Fig. 5.3(a), increasing a_5 or a_6 without changing the other coefficients creates a thick trailing-edge. Similarly, the values of a_1 are optimal around those associated with a NACA0012 foils, but it offers a slightly broader range of values for high η. The underlying reason could be illustrated by considering Fig. 5.3(b), where an increasing a_1 too much makes the foil into a teardrop shape that is large only at its leading edge. In the plot, for a_4, we observe that there is a much larger range of values for higher η, and that the most efficient foil has a larger coefficient value than that for a NACA0012 foil. However, the overall effect of increasing this coefficient is small, and leads to only an enhancements of 2% in η at best. The foils corresponding to changes in a_3 are seen to have a significantly larger influence on the maximum η along with an increasing trend of η as a_3 increases gradually from

that of a NACA0012 foil up to a steep drop-off point at an a_3 value of about 0.5. At the maximum, changing only this particular coefficient increases η by over 10% from that of a NACA0012 foil. Finally, variations in a_2 have the largest impact on η, because increasing its value from that of a NACA0012 foil improves this performance metric substantially, until a sharp drop is noticed for $a_2 = 0.32$. At its peak, changes in a_2 alone increases η by over 13%. These plots also reveal that the performance of a flapping foil is very sensitive to the geometric shape, meaning that very small variations in the shape of a foil lead to large differences in performance parameters. It is evident that η is particularly sensitive to thickness and shape of the foil between the locations $0.18c$ and $0.5c$ along the chord. It can be seen from Fig. 5.3, where the basis functions, corresponding to a_2 and a_3, are dominant in that region. Near the peaks of a_2 and a_3, η of the foil changes by more than 2% for every 1% change in a_i value. Furthermore, these results show that for other coefficients, such as a_4 and a_5, the performance is not sensitive to variations in the foil's shape in that region.

These new findings challenge the assumption made by many previous studies related to flapping foils [113]–[116]. These research investigations focused on various aspects of flapping foils, including 3D effects, kinematics, and flow features, solely relying on standard shapes of foils and assume that the results not sensitive to variations in their geometric configurations. Our present study reveals that small changes in the shape can give large changes in results, and that this effect varies for each coefficient. Therefore, simple variations in thickness of a flapping foil, belonging to a classical series of geometric configurations, do not necessarily scale to the whole domain of

flapping foils.

Next, we examine a wider range of shapes of foils, changing multiple parameters sequentially. First, from this study, we consolidate our findings by observing the effect that the maximum thickness and maximum thickness location have on the performance of the foil. Contour plots are presented in Fig. 5.6(a-b) that provides a map of η and C_T as a function of δ_{max} and S_{max}. Selected cases with a constant S_{max} changing δ_{max} (A_δ,B_δ, and C_δ) and constant δ_{max} changing S_{max} (A_S,B_S, and C_S) are chosen to present in depth analysis, each including the most efficient foil ($B_{\delta,S}$). The efficiency values in this plot, shown by the color contour, are normalized by the NACA0012 foil's efficiency. The middle region of this contour colored in red exhibits a higher η. The most efficient propulsive performance are shown by the foils with $0.18 < \delta_{max} < 0.22$ and $0.26 < S_{max} < 0.33$. A smaller width of the red region here compared to its height is also apparent, which indicates that η is less sensitive to variations in S_{max} and more dependent on δ_{max}. Additionally, the average thrust coefficient ($\overline{C}_T$), normalized by the NACA0012 thrust coefficient, is plotted as a function of maximum thickness (δ_{max}) and maximum thickness location (S_{max}). From this plot, it can be seen that the best performing foils in thrust are generally centered in two different regions, one around maximum thickness of δ_{max} = 0.19 and max thickness location of S_{max} = 0.375, and the other around a maximum thickness of δ_{max} = 0.18 and max thickness location of S_{max} = 0.26. Unlike efficiency, the maximum thrust production occurs in two regions and is equally sensitive to the maximum thickness and the location of maximum thickness along the foil.

5.1.3.2 Maximum Thickness

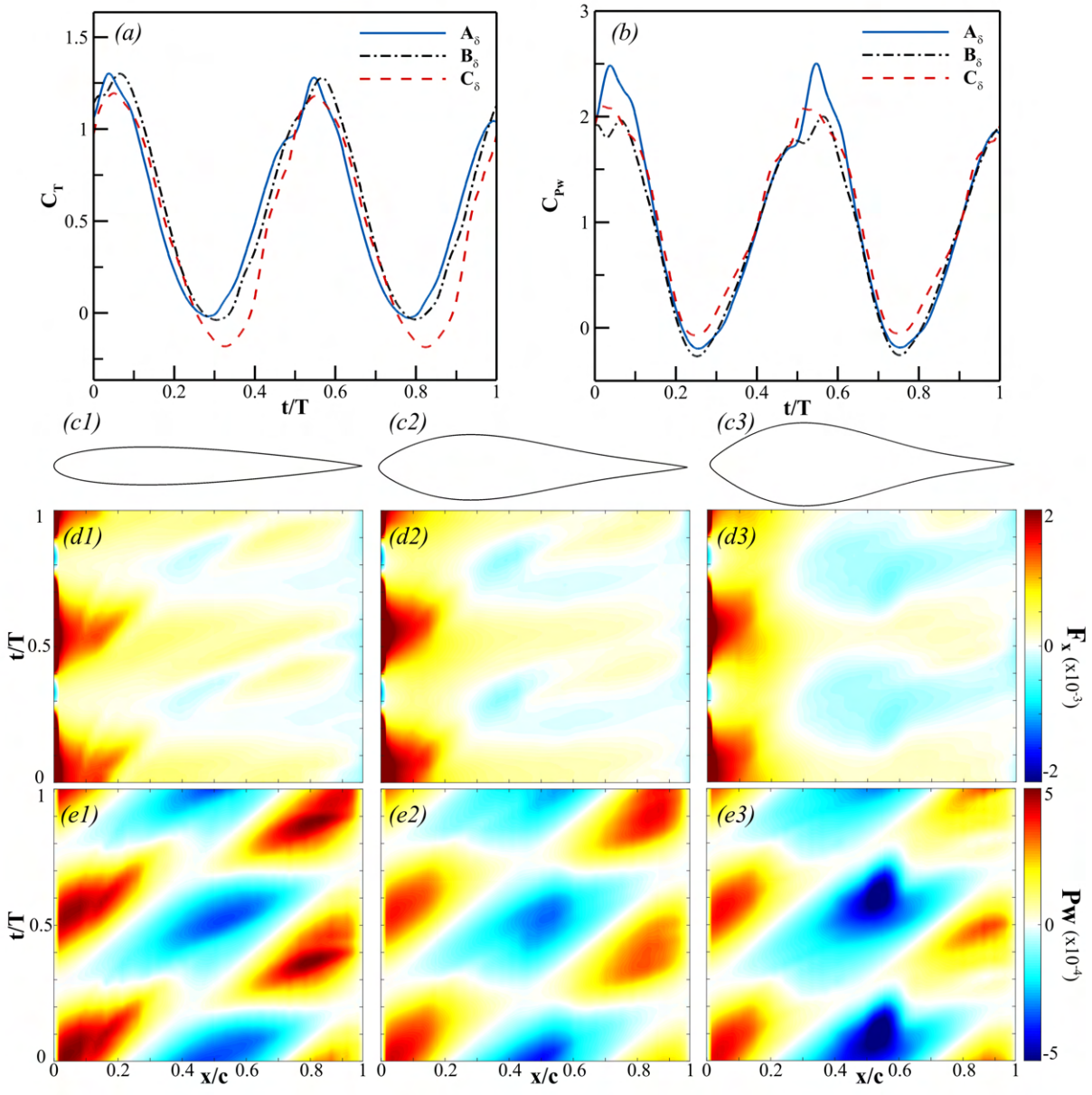

FIGURE 5.7: Instantaneous profiles of C_T and C_{Pw} *(a-b)*, shape profiles*(c)*, and contours of the thrust and power consumption along the foil through a cycle of motion *(d-e)* for thickness changing cases A_δ *(c1,d1,e1)*, B_δ *(c2,d2,e2)*, and C_δ *(c3,d3,e3)*.

In order to isolate the effects on performance due to maximum thickness for further investigation, three foil shapes are chosen with a constant maximum thickness location to review in depth. The cases chosen are shown in Fig. 5.6 and details are given in

Table 5.1. The S_{max} value of 0.3 was chosen to include the highest efficiency foil studied. In the table, it is observed that the most efficient foil, B_δ, has a large increase in efficiency with a small increase in thrust compared to the thinner foil, A_δ. The thicker foil, C_δ, experiences a large drop in both efficiency and thrust. The table also shows the breakdown of forward force into pressure and shear components. This indicates that the force changes occur primarily due to the pressure forces.

Case	δ_{max}	C_{x-pr}	C_{x-s}	η_R	C_R
A_δ	0.12	0.58	-0.013	1	1
B_δ	0.21	0.60	-0.011	1.15	1.03
C_δ	0.27	0.48	-0.006	0.79	0.88

TABLE 5.1: Selected cases changing δ_{max} along $S_{max} = 0.3$.

To illustrate temporal variations in hydrodynamic performance parameters and investigate the performance differences further, temporal profiles of C_T and C_{Pw} over a single flapping cycle of motion are shown for the three aforementioned cases in Fig. 5.7*(a-b)*. The coefficients of thrust and power are calculated using equations 5.6 and 5.7. The figure also shows the shapes of the foils *(c)* along with the thrust produced *(d)* and power consumed *(e)* along the length of the foil over a cycle of motion. From the figure, we see that both the thrust and power exhibit their respective peaks at around $t/T = 0.05$ and again at $t/T = 0.55$, which corresponds to the end of the heaving motion. C_T and C_{Pw} then dip back down, reaching their minima at $t/T = 0.30$ and $t/T = 0.80$. This corresponds to the point immediately after the foil direction change occurs ($t/T = 0.30$).

In comparing case A_δ to the most efficiency foil (B_δ), the large discrepancy in efficiency previously mentioned is observed in Fig. 5.7*(b)* at the end of the heaving motion, as

the direction change is initiated ($t/T = 0.55$). In comparing the contour plots of power consumption at these times, it is evident that the increase in power consumption is a result of differences at the leading edge of the foil, from $x/c = 0$ to $x/c = 0.3$. To investigate further, the vorticity and pressure contours at $t/T = 0.55$ are shown in Fig. 5.8. The pressure coefficient plotted is calculated as

$$C_P = \frac{p}{0.5\rho U_\infty^2}, \tag{5.11}$$

where p is the hydrodynamic pressure. In the vorticity, an obvious difference occurs in the V1 vortex on the top leading edge of the foil. In case A_δ, the leading edge vortex begins to separate from the foil body, generating vortex V1 and resulting in a stronger low pressure area on the top front edge of the foil. Conversely, in case B_δ the leading edge stays attached well to the body of the foil. There is however still a low pressure region formed on the top leading edge of the foil. In the thinner foil A_δ, the normal to this low pressure region faces primarily in the $+y$ direction. Alternatively, in the thicker foil B_δ the normal to this surface faces more in the $-x$ direction, promoting the overall thrust. The larger force in $+y$ in A_δ leads to the increased power consumption through this portion of the motion, and prevents the increased low pressure region from enhancing the thrust significantly over the value observed in foil B_δ.

In comparing C_δ to B_δ, there is a significant decrease in thrust production that begins as the foil changes directions and exists through much of the next stroke ($t/T = 0.75$).

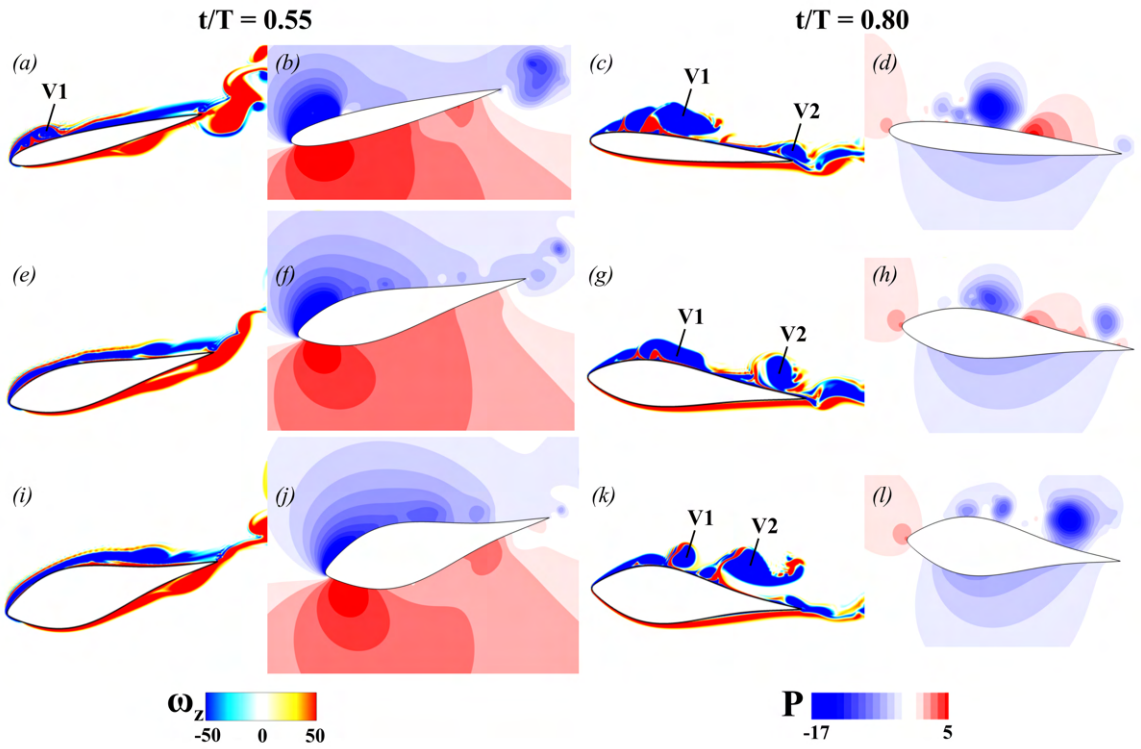

FIGURE 5.8: Vorticity and pressure contour plots for thickness changing cases A_δ *(a-d)*, B_δ *(e-h)*, and C_δ *(i-l)*. Vorticity is shown at points where coefficients of thrust and power vary the most between the cases.

In comparing the contour plots of thrust production, a large low thrust region is observed in the back 60 percent of the foil is observed for foil C_δ that does not appear for the other cases. In the vorticity and pressure plots at this time (Fig. 5.8), it is observed that case C_δ has significantly more breakdown of the leading edge vortex along the back half of the foil, following the point of maximum thickness. Specifically, a significantly larger V2 vortex has built up and completely separated from the foil body. In the corresponding pressure contour, it can be seen that this also corresponds to a lack of a high pressure region between V1 and V2 observed for the other foils. This significant drop in pressure leads to the overall decrease in the net force in $-x$, giving the drop in cycle-average thrust observed. This separation occurs due to the larger

thickness giving an overall steeper foil behind the maximum thickness point, promoting separation of the leading edge vortex. The vortex separation prevents constructive interference between the V2 vortex with the trailing edge vortex, as is seen in B_δ. The lack of constructive interference leading to a lower thrust production is consistent with Ref. [117].

Overall, the thickness is found to be a sensitive parameter for efficiency due to the breakdown of the leading edge vortex, along with the proportion of the normal surface that points in the forward direction. In the case where the foil is thinner, there is less of a component in the thrust direction and an increase in horizontal force. While the thrust is compensated by the breakdown of the leading edge vortex at the front edge of thinner foils giving better suction force, this only increases the already higher horizontal force, consuming additional power. Because of this, increase in thickness gives the gradual increase in efficiency observed in Fig. 5.6(a). When the foil becomes too thick, however, the leading edge vorticies begin to break down behind the point of maximum thickness. This breakdown removes the high pressure region along the back of the foil that contributes significantly to thrust production. Because the transition from smoother vorticity to the total breakdown of the leading edge vortex is more abrupt, the efficiency drops quickly when the thickness becomes too high in Fig. 5.6. These results show that generally, a larger leading edge is advantageous, which is consistent with the results found in Ashraf et al. [64].

5.1.3.3 Maximum Thickness Location

To similarly isolate the effects on performance due to maximum thickness location along the foil for further investigation, three foil shapes are chosen with a constant maximum thickness to review in depth. Detailed values for the cases chosen are given in Table 5.2. The δ_{max} value of 0.21 was chosen to include the highest efficiency foil studied. In the table, it is observed that the most efficient foil, B_S, has a large increase in efficiency with a small increase in thrust compared to the other two. The table also shows the breakdown of forward force into pressure and shear components. This indicates that the force changes occur primarily due to the pressure forces.

Case	S_{max}	C_{x-pr}	C_{x-s}	η_R	C_R
A_S	0.25	0.56	-0.009	1.03	0.97
B_S	0.3	0.60	-0.011	1.15	1.03
C_S	0.4	0.58	-0.01	1.02	0.99

TABLE 5.2: Selected cases changing S_{max} along $\delta_{max} = 0.21$.

To investigate this further, the temporal profiles of C_T and C_{Pw} over a single flapping cycle of motion is shown for the three aforementioned cases in Fig. 5.9*(a-b)*. The coefficients of thrust and power are calculated using equations 5.6 and 5.7. The figure also shown the shapes of the foils *(c)*, along with the thrust produced *(d)* and power consumed *(e)* along the length of the foil over a cycle of motion. The overall trends from the figure are similar to the maximum thickness cases, with both C_T and C_{Pw} exhibit their respective peaks at around $t/T = 0.55$ and reaching their minima at $t/T = 0.80$.

In comparing case B_S with case C_S, a decrease in thrust produced and increase in power consumption is observed at the end of the heaving motion as the change in direction

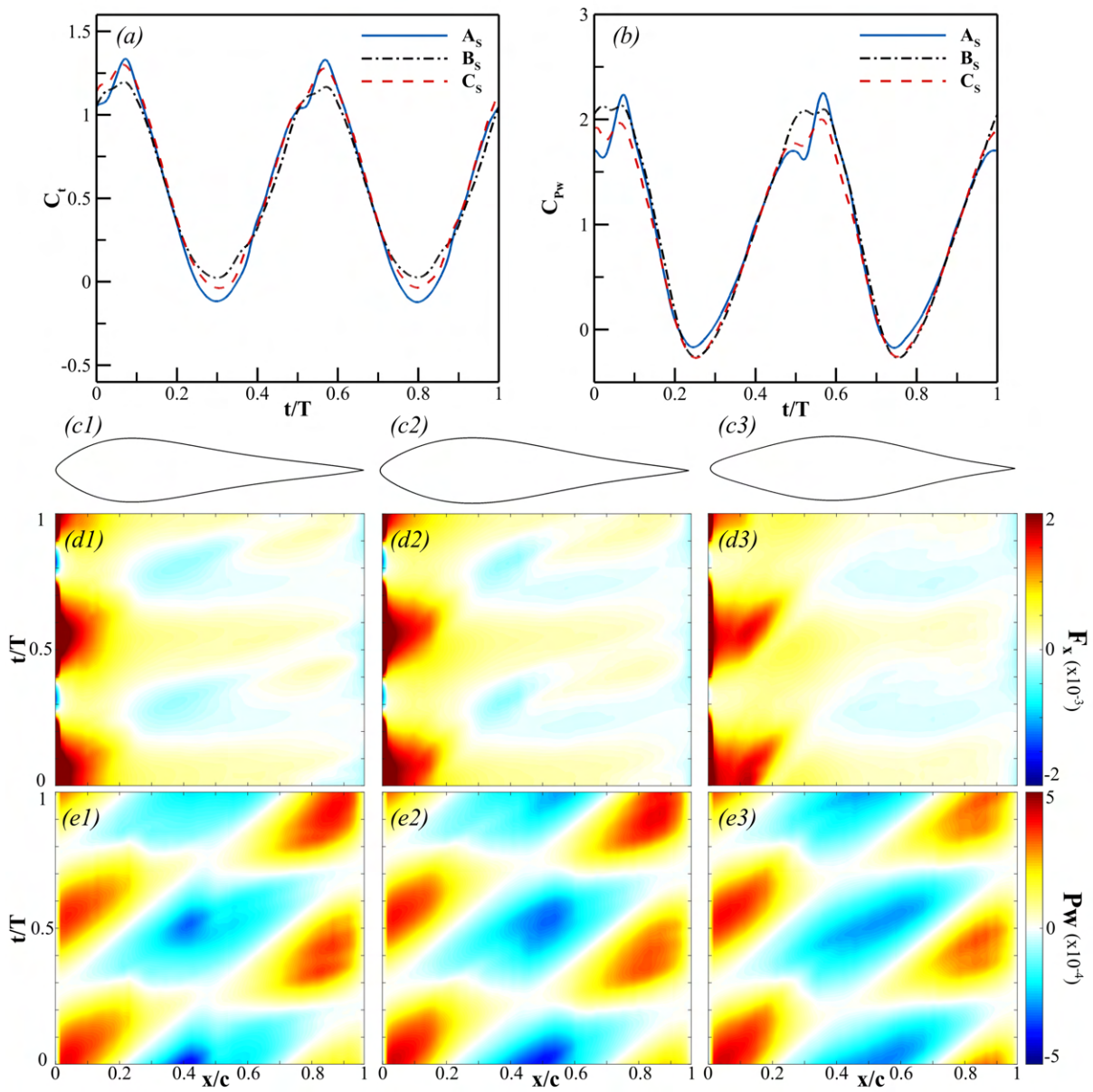

FIGURE 5.9: Instantaneous profiles of C_T and C_{Pw} *(a-b)*, shape profiles*(c)*, and contours of the thrust and power consumption along the foil through a cycle of motion *(d-e)* for thickness changing cases A_S *(c1,d1,e1)*, B_S *(c2,d2,e2)*, and C_S *(c3,d3,e3)*.

is initiated. In the contour plots for thrust and power, it is observed that the thrust difference occurs primarily at the front of the foil, around 25 percent of the chord, and the power difference occurs at the front of the foil body. In the pressure and vorticity plots

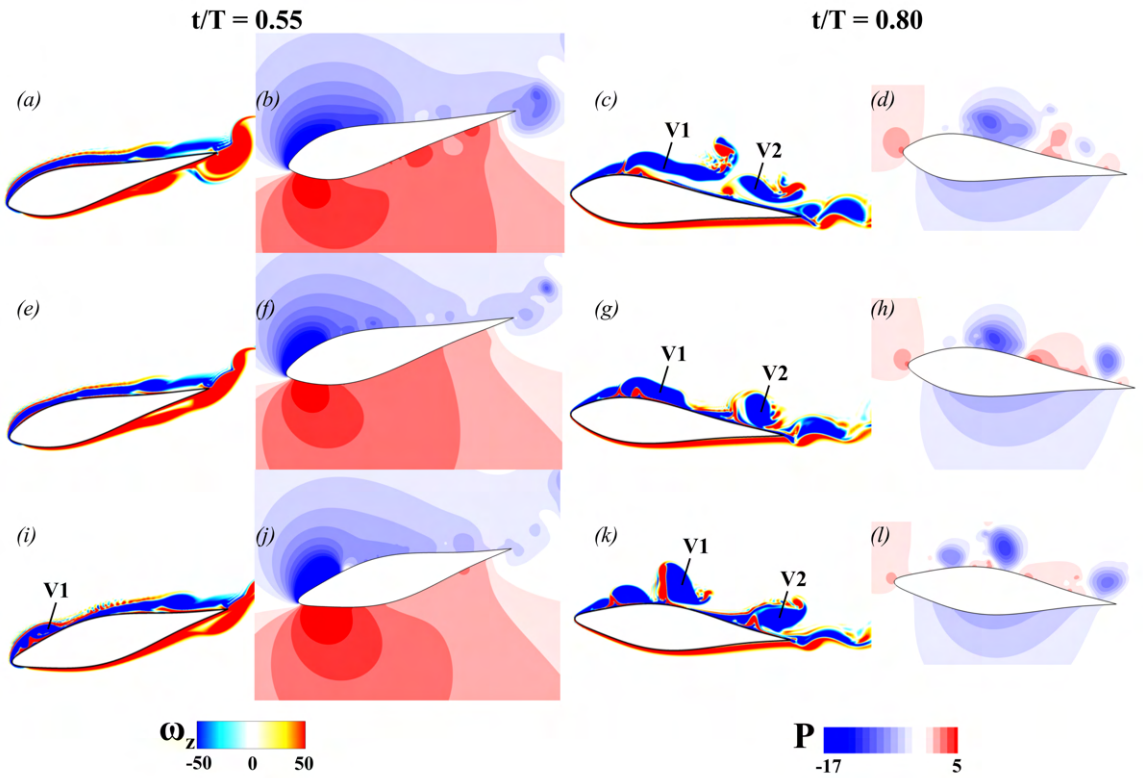

FIGURE 5.10: Vorticity and pressure contour plots for thickness changing cases A_S *(a-d)*, B_S *(e-h)*, and C_S *(i-l)*. Vorticity is shown at points where coefficients of thrust and power vary the most between the cases.

shown in Fig. 5.10, a similar phenomena is observed to the thinnest foils discussed in the previous section. The leading edge vortex starts to break down near the front edge, leading to a larger vortex building up (V1). This gives a similar larger high pressure region causing an increase in the lateral force, resulting in an increase in power consumption. This can be attributed to the delay in the maximum thickness of the foil occurring so far back along the chord that it acts in the front as a thinner foil would. Additionally, a higher pressure region is observed developing behind the V1 vortex. This occurs still before the maximum thickness point, so the surface of the foil has a normal component in the $-x$ direction. The higher pressure at this point gives the reduction in thrust produced for this region discussed above. This occurs because of

the aforementioned geometric phenomena leading to the formation of V1, along with the maximum thickness point being far enough back along the foil to allow the higher pressure to be a detriment to the thrust production in the foil.

Similar to δ_{max}, efficiency is shown to be sensitive to S_{max} due to a breakdown of the leading edge vortex around the point of maximum thickness, which does not occur for the most efficient foil shape but happens for the others. The optimal values are seen around $S_{max} = 0.3$, which is consistent with the findings in Ref. [66].

5.1.3.4 Effect of Reynolds Number

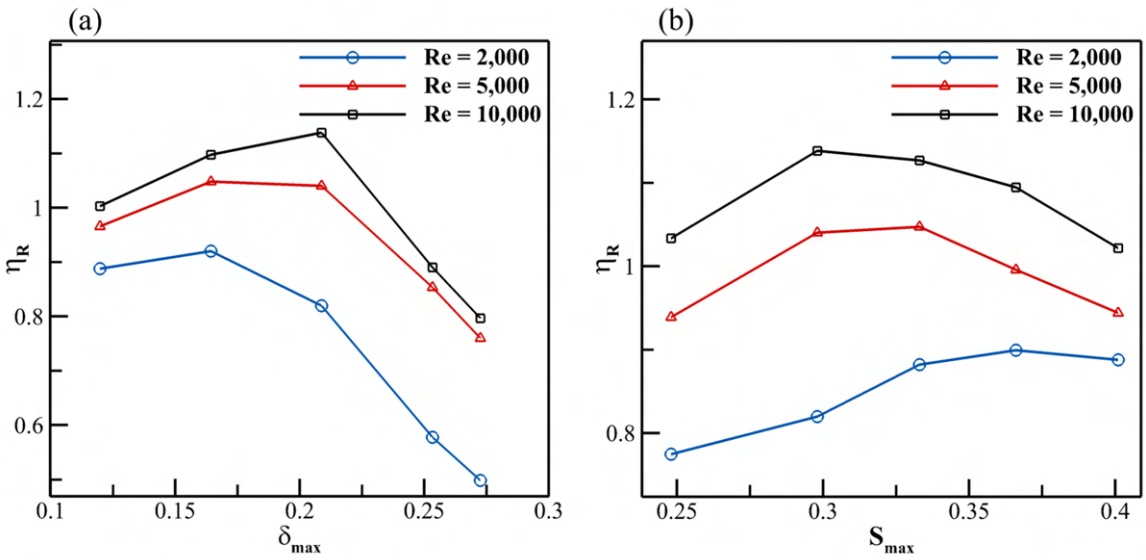

FIGURE 5.11: Normalized efficiency vs. maximum thickness (a) and maximum thickness location (b) for varying Reynolds numbers.

Next, the effect of maximum thickness and maximum thickness location at different Reynolds numbers is studied. To accomplish this, select foil shapes are simulated at varying Reynolds numbers, to confirm the applicability of our results across varying flow regimes. First, cases varying the maximum thickness with a constant maximum

thickness location along the foil are tested, changing the Reynolds number to 2000, 5000, and 10000. The resulting propulsive efficiencies are shown in Fig. 5.11(a). Next, the same process is repeated changing the maximum thickness location, keeping the maximum thickness constant. The results are shown in Fig. 5.11(b). First, an overall trend of higher Reynolds number giving higher efficiency is observed across all of the cases. In the cases changing maximum thickness, a similar curve is shown for all Reynolds numbers, though the peak efficiency values occur at smaller thicknesses for lower Reynolds numbers. These results are consistent with the findings of Ashraf et. al. [64], showing that for as Reynolds number increases, the optimal thickness for efficiency increases also. A similar phenomena is observed to Fig. 5.8, however the complete leading edge vortex separation occurs in thinner foils at lower Reynolds numbers, giving the curve shape observed. In the maximum thickness location cases, a similar phenomena occurs with the same overall efficiency curves, however, the optimal thickness location for efficiency is shifted towards the back of the foil. Similar to the thickness cases, the leading edge vortex separation that makes the smallest maximum thickness location cases inefficiency occurs more in the lower Reynolds number cases. This gives the shift in efficiency plot when changing Reynolds number seen in the figure.

The effect of Reynolds number is futher observed by simulating all foil shapes at a Reynolds number of 5000. The results are presented in the contour plots shown in Fig. 5.12 which provides a map of η and C_T as a function of δ_{max} and S_{max}. The efficiency values in this plot, shown by the color contour, are normalized by the NACA0012

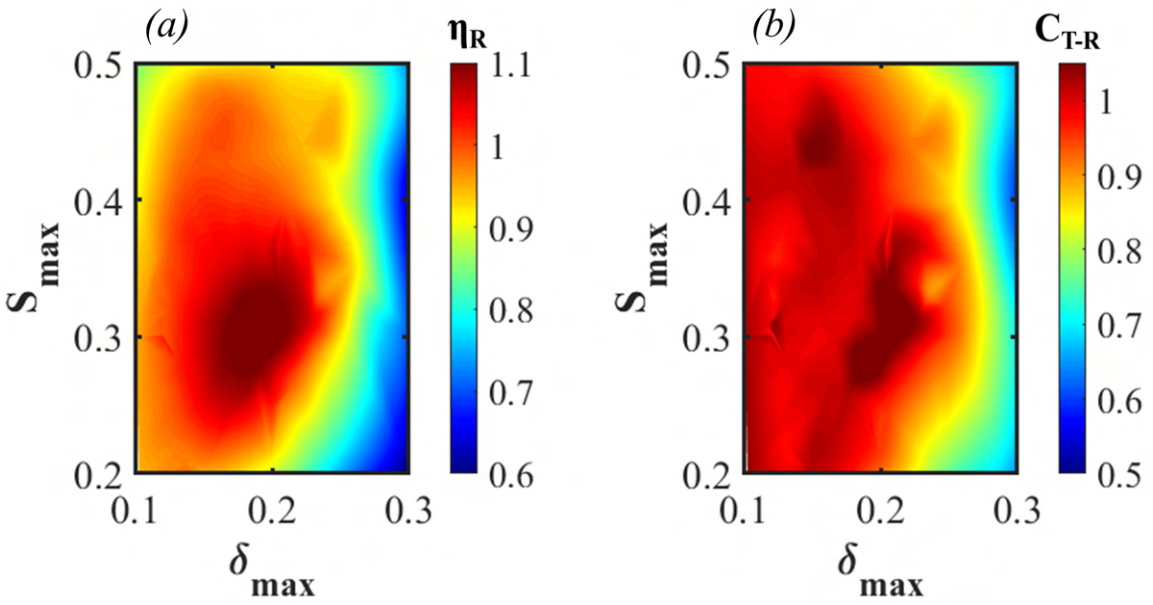

FIGURE 5.12: Contour plots of efficiency *(a)* and thrust *(b)* vs Maximum thickness and Maximum thickness location for all of the shapes used in this study at Re = 5000.

foil's efficiency. The middle region of this contour colored in red exhibits a higher η. Comparing to the Reynolds number of 10000 results presented in Fig. 5.6, the overall trend and locations of peak performance in both thrust and efficiency are the same, including two regions of high thrust production and a single region of high efficiency. This further confirms that the results are robust within a small range of Reynolds numbers.

5.1.4 Section Summary

In this work, we conducted a holistic study of the shape of tail-like flapping propulsion. Specifically, we examined the effect of foil shape on performance and the underlying mechanisms that cause the variation in performance. We used a CST parametrization method to create geometric parameters that are varied to create unique foil shapes. We

then prescribed a flapping motion and flow conditions in the range of the ones seen in bio-robotic swimming. Computational fluid dynamics simulations of these shapes in a flapping motion were completed using an in-house immersed boundary method-based direct numerical solver. From the initial study varying a single CST parameter at a time, we found that the efficiency of a foil was very sensitive to the shape of the foil. Specifically, we saw a significant change in performance when adjusting the thickness of the foil in the range of 18 to 50 percent of the chord length. Outside of this range, the shape of the foil had little effect on the efficiency.

Next, in a study of a larger subset of foil shapes for efficiency it was found that the maximum thickness and the location of the maximum thickness had an optimal range of 0.2c and 0.3c, respectively. Sensitivity of efficiency to the maximum thickness was greater than it was to its location along the foil. Upon analyzing the continuous coefficients of thrust and power, along with the vortex structures and pressure fields for varying each parameter individually, we found that better attachment of the leading edge vortex, leading to constructive interference with the trailing edge vortex, is the source of the performance enhancement. Additionally, a favorable pressure gradient during the turning from the up-stroke to the down-stroke was observed, which lead to the increase in thrust generated and decrease in power consumed, respectively, for the most efficient cases. Similar results were shown in the optimal of both the maximum thickness and maximum thickness location, with variations in either leading to poorer adhesion of the leading edge vortex, either in the front of the foil before the point of maximum thickness in cases with thinner foils or at the back of the foil behind the

maximum thickness point in cases with thicker foils.

Overall, we found that a thicker leading-edge on a foil led to more favorable pressure gradients to lower power consumption during a flapping motion, while a thicker foil results in a drop in thrust produced due to the lack of adhesion of the leading edge vortex preventing constructive interference with the trailing edge vortex. We saw that not only is the overall performance of a flapping foil highly sensitive to its shape, but also the vortex structures behind the flapping performance is significantly different depending on the choice of the foil shape. Because of this sensitivity and change based on the shape of a foil, care should be taken when selecting foil shapes to use for bio-inspired underwater robotics, and careful shape selection can lead to significant performance benefits.

5.2 Body Shape and Kinematics Effects in a Tuna-inspired Robotic Plaform

In this section, the relationship between morphological and kinematic effects in a bio-inspired robot is studied in detail. To do this, a detailed reconstruction is made from high-speed videos of the Tunabot Flex platform [10]. The robotic platform is detailed in Fig. 5.13. The body measures 25.5cm in length, and some body flexibility is generated via multiple body joints connecting rigid body segments. The platform achieves high-efficiency tuna-like swimming at frequencies up to 8 Hz and 4.6 body lengths per second.

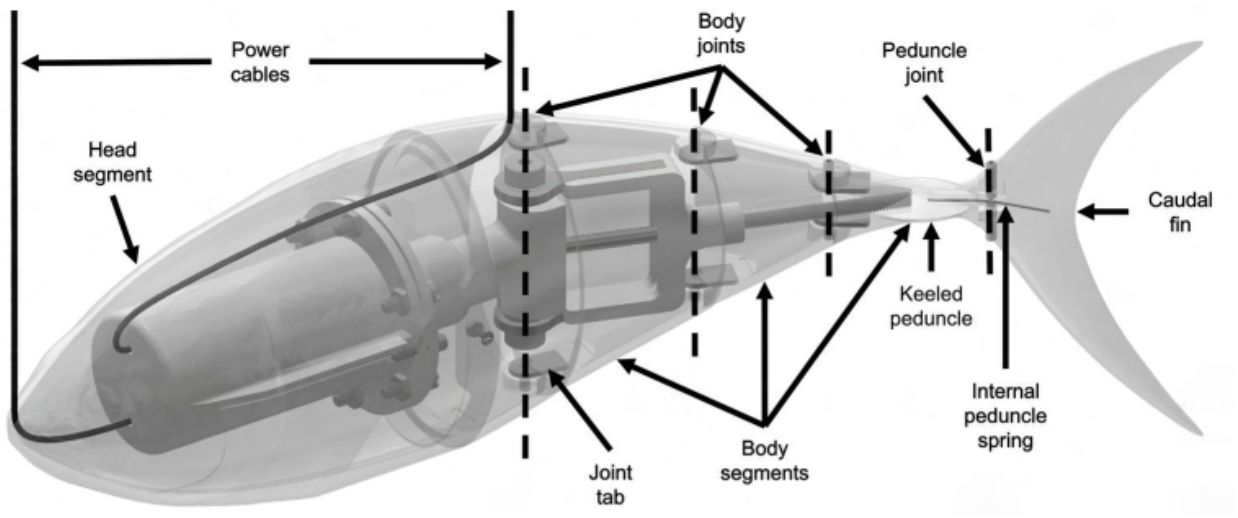

FIGURE 5.13: Design of the Tunabot flex, reproduced from White et al. [10].

3D flow simulations are then conducted in a high-fidelity flow solver. Morphological and kinematic parameters are then adjusted based on flow simulation results within the design constraints of the Tunabot platform construction. The study begins by varying the length-to-width ratio of the Tunabot body, finding that an increase in the width has little impact on the caudal fin performance, but does increase drag by an increasing amount when the body width is greater than 23% of the length. Next, the body joint maximum angles are varied to observe the impacts of varying amounts of body flexibility. More closely mimicking the kinematics from the yellowfin tuna found a better propulsive efficiency and cost of transport, however, the decreased amplitude of the caudal fin does lead to losses in thrust production and speed. Finally, the addition of rigid median fins to the Tunabot flex design is explored. Through beneficial pressure and vortex interaction thrust production on the caudal fin and drag on the body can be reduced by Tuna-inspired dorsal and anal fin design. These findings serve to bridge the gap between biologically driven fluids studies and their application in bio-inspired

robotic platforms.

5.2.1 Problem Statement

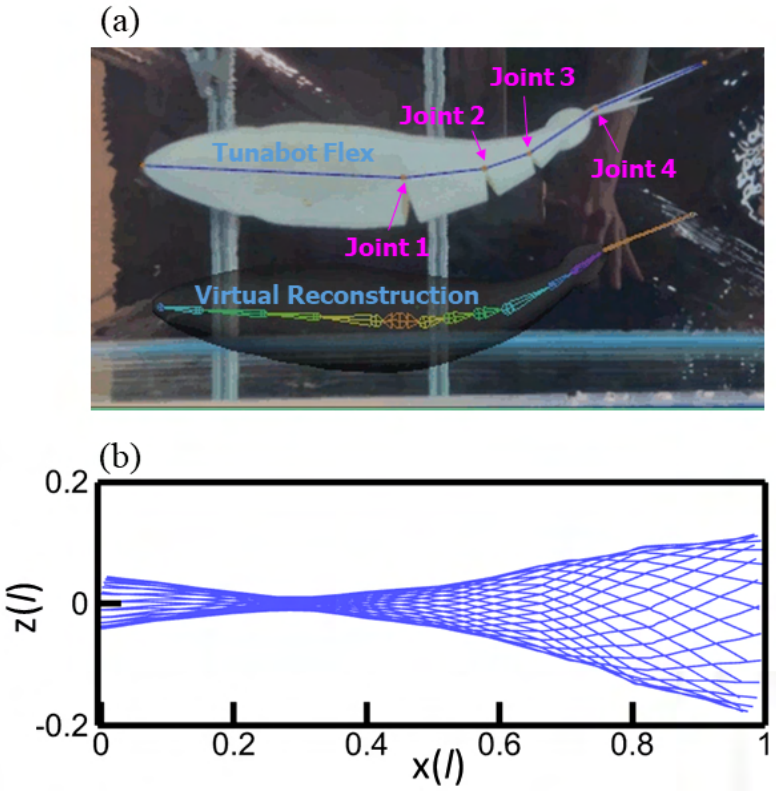

FIGURE 5.14: (a) Snapshot of a direct comparison between the Tunabot flex and virtual Tunabot flex in the reconstructed motion. (b) Midline kinematics of the reconstructed Tunabot flex motion.

In this research, the Tunabot flex is studied in steady forward swimming. The Tunabot Flex platform focuses on the impacts of body flexibility by introducing body joints in a single motor platform during steady swimming at varying strouhal numbers. As additional body joints are introduced, a performance enhancement is shown. More detail about the platform and experimental setup can be found in White et al. [10]. To reconstruct the motion of Tunabot flex, a CAD model is remade for simulation from the robotic design. A 3D surface model of the body was created using Autodesk Maya.

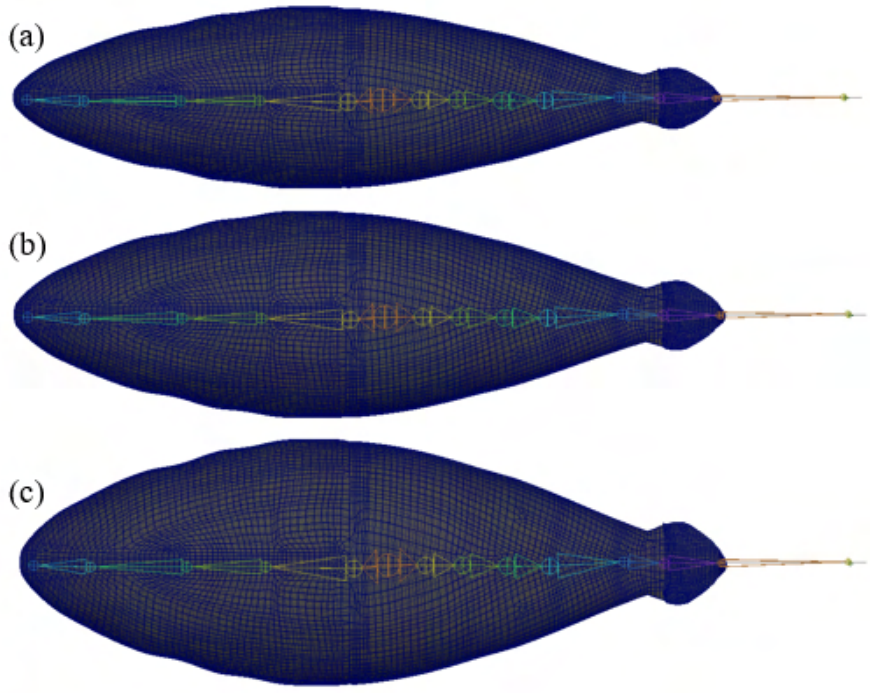

FIGURE 5.15: Virtual body with increasing body thicknesses: baseline thickness (a), 25% thickness increase (b), and 50% thickness increase (c).

The surface is then smoothed and finely meshed for simulation. This surface model is also rigged with a virtual skeleton to control the Tunabot's posture and deform the corresponding skin in a realistic manner. A virtual scene is then set up to overlay the model with a bottom-view video of the Tunabot swimming. The Tunabot in the videos used for this reconstruction was flapping at a frequency of 3.7 Hz. Finally, the swimming kinematics of the Tunabot are reconstructed by matching frame-by-frame the position of the Tunabot in the video with the reconstructed Tunabot. The virtual body, compared with the real Tunabot flex while swimming in the flow channel, is shown in Fig. 5.14(a). The midline of the virtual model generated from the reconstructed motion is shown in Fig. 5.14(b). This methodology has been used extensively to reproduce video motion virtually for fluid simulations in biological [84], [110], [118], [119] and

biorobotic [120], [121] applications.

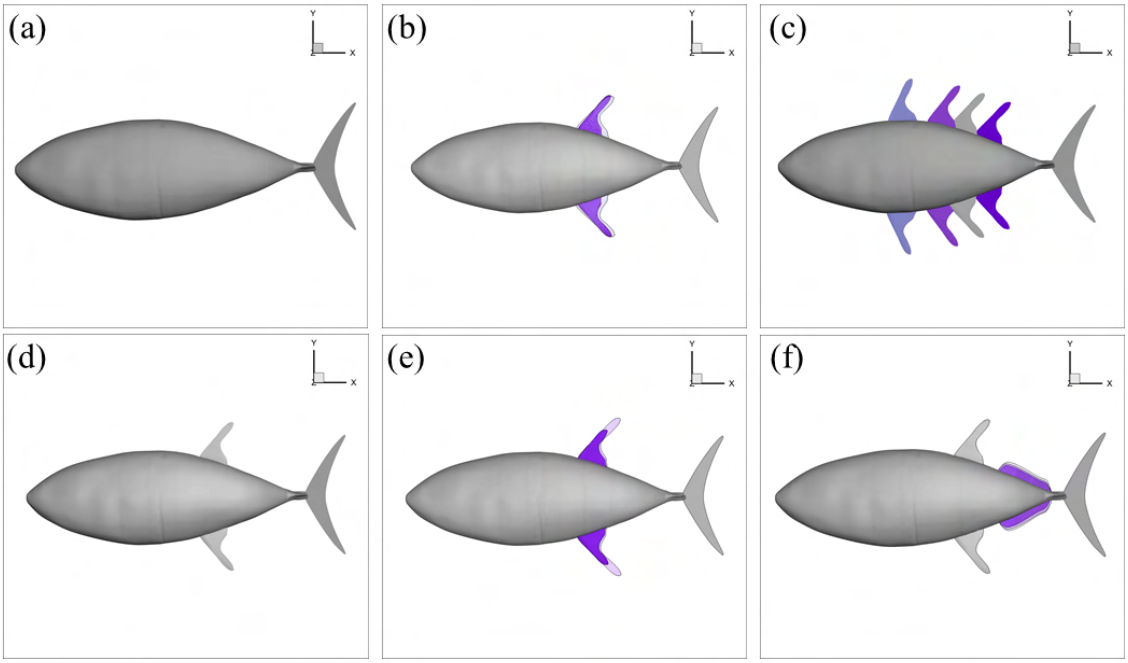

FIGURE 5.16: Addition of median fins, demonstrated by the baseline shape (a), yellowfin-tuna modeled dorsal and anal fin (b), and inclusion of a fin-band (f), with parameter changes of fin width (b), fin position (c), fin height (e) and fin band size (f).

In addition to this baseline case, the body size is varied by scaling the entire body laterally. The scaled bodies used for simulation are shown in Fig. 5.15. The body kinematics are also varied by scaling the maximum joint angles for each joint shown in Fig. 5.14. Finally, the median fin additions are shown in figure 5.16. In the figure, the baseline shape is shown along with all tested median fin designs. The baseline shape (Fig. 5.16(d)) is based on the shape taken from images of a yellowfin tuna dorsal and anal fin. Additional models are generated by changing the parameters of the fin height, width, and placement on the body, and the addition of a fin band based on the finlets present on the biological tuna body.

5.2.2 Simulation Setup

The flow conditions in this study are described by two dimensionless parameters, the Reynolds number (Re) and the Strouhal number (St), defined as:

$$Re = UL/v \tag{5.12}$$

$$St = fA/U \tag{5.13}$$

where U is the incoming flow velocity, A is the peak-to-peak amplitude of the caudal fin tip, v is the kinematic viscosity of the fluid, and f is the tail beat frequency. The Reynolds number is chosen to be 4,000. The Strouhal number of 0.51 is chosen to keep the cases near the free-swimming condition, where the cycle average net force C_x is zero, based on the forces resulting from a series of simulations completed using the reconstructed kinematics at varying Strouhal numbers.

To sufficiently resolve the flow near the body without wasting meshes in unnecessary regions, mesh refinement blocks are used. These are arranged in a nested formation, allowing for efficient allocation of grid points and enhanced parallelization of the fluid solver as discussed in section 2.1. The grid setup, boundary conditions, and block geometries are shown in Figure 5.17. In the figure, the baseline cartesian grid is shown, and each successive block doubles the refinement of the mesh within the block. This results in a grid spacing around the body of 0.0039L, resulting in a total of approximately 11.3 million meshes.

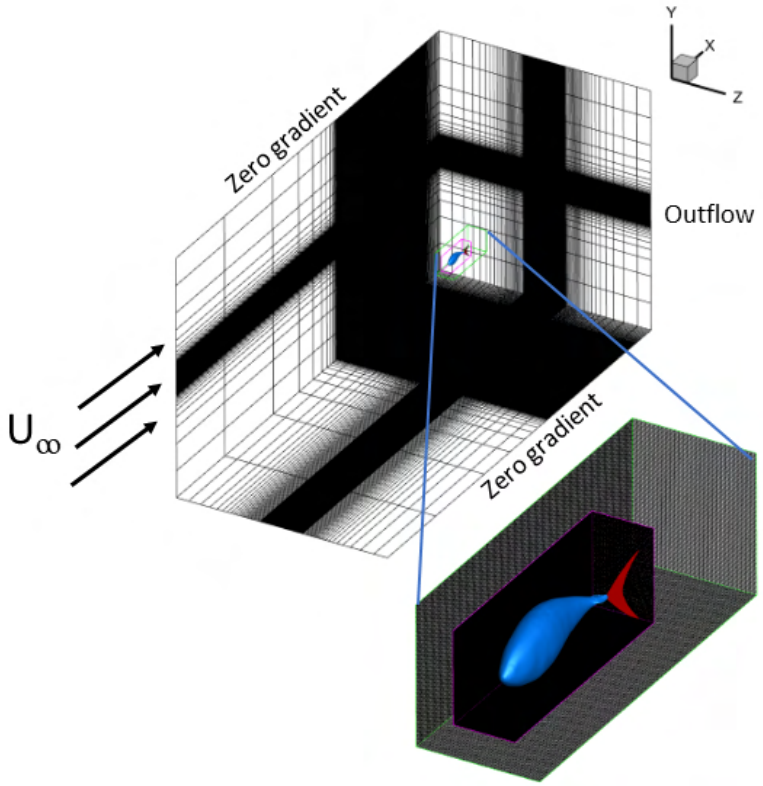

FIGURE 5.17: Computational grid schematic with local mesh refinement blocks shown along with the boundary conditions for the simulation.

To understand our results, we first use the thrust coefficient in the -x direction:

$$C_T = \frac{F_T}{\frac{1}{2}\rho U_\infty^2 S} \tag{5.14}$$

where S is the surface area of the caudal fin, F_T is the instantaneous force on the caudal fin in the $-x$ (forward) direction, ρ is fluid density, U is free stream velocity and L is the body length. Averaging C_T over one period of motion for each foil, giving $\overline{C_T}$, corresponding to the net thrust over a cycle of motion. Similarly, the coefficients of drag and power can be computed as:

$$C_D = \frac{F_D}{\frac{1}{2}\rho U_\infty^2 S} \tag{5.15}$$

$$C_{pw} = \frac{Pw}{\frac{1}{2}\rho U_\infty^3 S} \tag{5.16}$$

where F_D is the instantaneous force on the body in the +x (backward) direction and Pw is the instantaneous power consumed over the entire body for the undulating motion. The averages over a period of motion are also computed, giving the results of $\overline{C_D}$, which is the net thrust over a cycle of motion, and $\overline{C_{pw}}$, which is the net power consumed over a cycle of motion. Finally, the efficiency is calculated using a Froude efficiency, which is defined as a ratio of thrust output to total power input:

$$\eta = \overline{C_T}/\overline{C_T} \tag{5.17}$$

5.2.3 Results and Discussion

5.2.3.1 Reconstructed Motion and Flow

In this section, the hydrodynamic performance, vortex, and wake structures from the simulation of the reconstructed Tunabot flex kinematics are presented. Each simulation is computed for six periodic tail beat cycles to ensure that the results have reached a steady periodic state. The thrust, drag, and power consumption for the body (shown in blue in Fig. 5.17) and the caudal fin (shown in red in Fig. 5.17) are shown in Fig. 5.18. From the figure, two distinct peaks of thrust production and power consumption

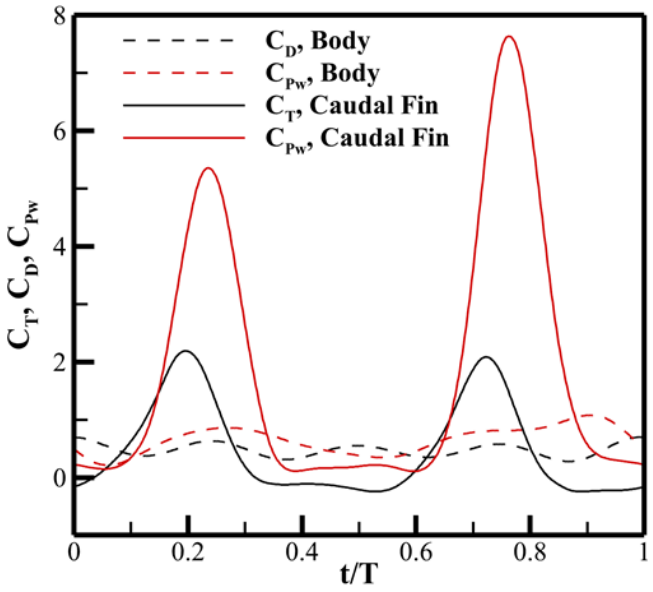

FIGURE 5.18: Coefficients of power and thrust on the body and caudal fin of the Tunabot over one cycle of reconstructed motion.

are observed, corresponding with the right-to-left and left-to-right strokes of the tail. Compared with the results from the Tunabot with no body flexion [120], the thrust and power consumption are both more concentrated at the peaks, with less thrust being produced during each mid-stroke when the body flexion is present.

To visualize the 3D vortex structures, isosurfaces are defined by Q criterion [122]. Q is defined by

$$Q = \frac{1}{2}[|\mathbf{\Omega}|^2 - |\mathbf{\Lambda}|^2] \tag{5.18}$$

where $\mathbf{\Omega}$ is defined by $\mathbf{\Omega} = \frac{1}{2}[\Delta u - (\Delta u)^T]$ and $\mathbf{\Lambda}$ is defined by $\mathbf{\Lambda} = \frac{1}{2}[\Delta u + (\Delta u)^T]$. These represent the vorticity and shear strain rate tensors, respectively. The regions of high Q can be used to visualize the presence of vortices or highly rotational flow [123].

Figure 5.19 shows the vortex wake of the reconstructed model in steady swimming.

Iso-surfaces of the Q-criterion are utilized to visualize the wake structures. During the flapping motion, interconnected vortex rings are generated by the caudal fin. Rings are labeled using R0 to R3 in chronological order of generation. The rings form a general reverse Kármán vortex street. The posteror body vortex (PBV) is also indicated. At t/T = 0.25, three vortex rings are identified in the wake, one from each prior half-stroke of the tail. They expand significantly laterally in the body's frontal plane due to the lateral movements of the caudal fin during a flapping motion. The body median plane, however, shows a slight narrowing of the wake as it leaves the caudal fin. At t/T = 0.75, vortex rings R1-R3 have advected further downstream, and a new ring, R0, has formed during the half stroke from t/T = 0.25 to t/T = 0.75.

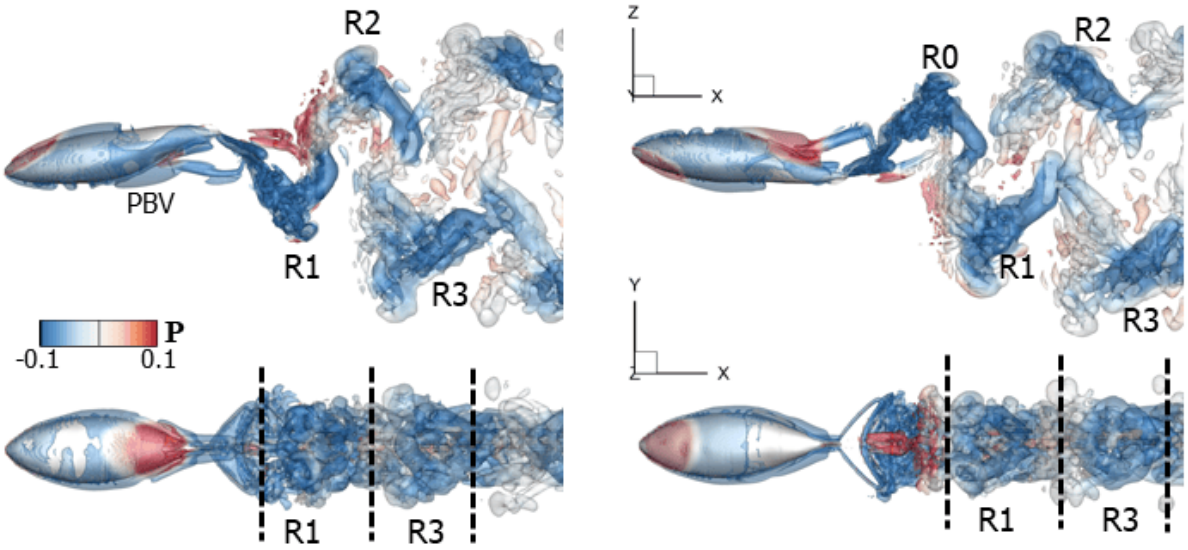

FIGURE 5.19: Vortex structures around Tunabot t/T = 0.25 (left) and t/T = 0.75 (right) from the top and side views. Isosurfaces are plotted with a Q criterion of Q = 40 and colored by the pressure.

In addition to the wake, a vortex tube is formed along the body and separates near the peduncle region. A high-pressure region is formed in the posterior body region,

producing some thrust on the body that contributes to the overall trust production for each half-cycle.

5.2.3.2 Effect of Length to Width Ratio

In this section, the hydrodynamic performance, vortex, and wake structures are observed for the reconstructed kinematics prescribed to the computational model with varying body thicknesses. The thickness is varied by scaling the lateral size of the model, with the body length L held constant. The baseline body length, L, is held constant. The baseline body width is 18.8% of the body length and is scaled up by 10, 20, 30, 40, and 50 percent. The change in body shape did not have any significant impact on the caudal fin performance, with cycle average thrust and power values remaining within two percent of the baseline values. The body drag and power, however, saw a significant change in the cycle average. The coefficients are given in Tab. 5.3. In the table, it is seen that the drag and power increase very moderately from 0.188L to 0.225L, after which there is a steeper increase in the drag and power associated with increasing body thickness.

Body Width	$\overline{C_D}$	$\overline{C_{pw}}$
Baseline (0.1888L)	0.47	0.65
0.207L	0.50	0.68
0.225L	0.50	0.67
0.244L	0.57	0.75
0.252L	0.60	0.78
0.282L	0.64	0.83

TABLE 5.3: Cycle averaged coefficients of drag and power on the body for each body size.

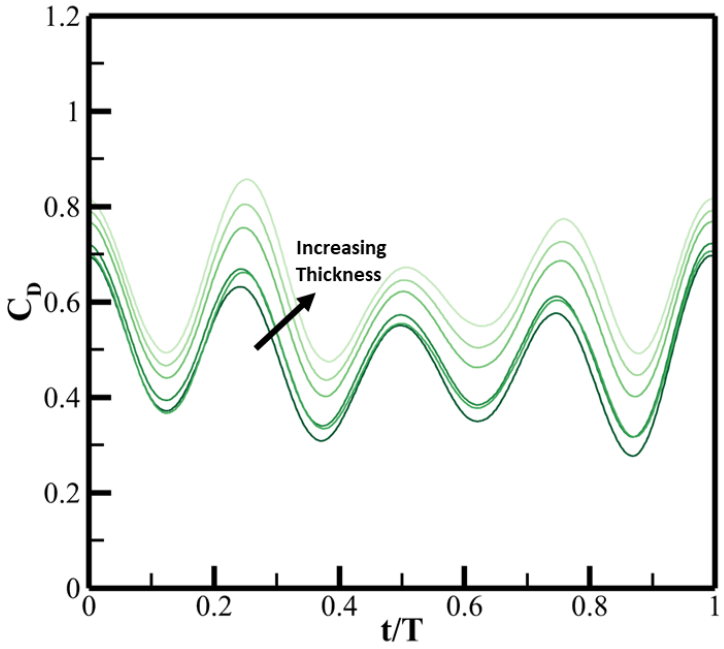

FIGURE 5.20: Coefficient of drag C_D on the body for each Tunabot body thickness from the baseline to +50%. Darker colors correspond with a thinner body.

The continuous body drag is plotted over a cycle in Fig. 5.20. In the figure, more peaks are seen than the caudal fin values of Fig. 5.18 because the body drag is not directly tied to the half-strokes of the tail. The drag difference between 0.188L, 0.225L, and 0.252L is relatively small, with a continuous increase in drag for each subsequent thicker body. Some fluctuation is seen however around t/T = 0.25. At this peak, the difference between each thickness above 0.252L is significantly greater than the rest of the cycle.

To more closely observe the difference between these cases, the flow for thicknesses of 0.188L, 0.225L, and 0.252L percent of the length are plotted in Fig. 5.21. The figure shows a similar overall structure to the baseline flow presented in Fig. 4. The posterior body vortex, however, grows significantly with the change in body thickness. As this

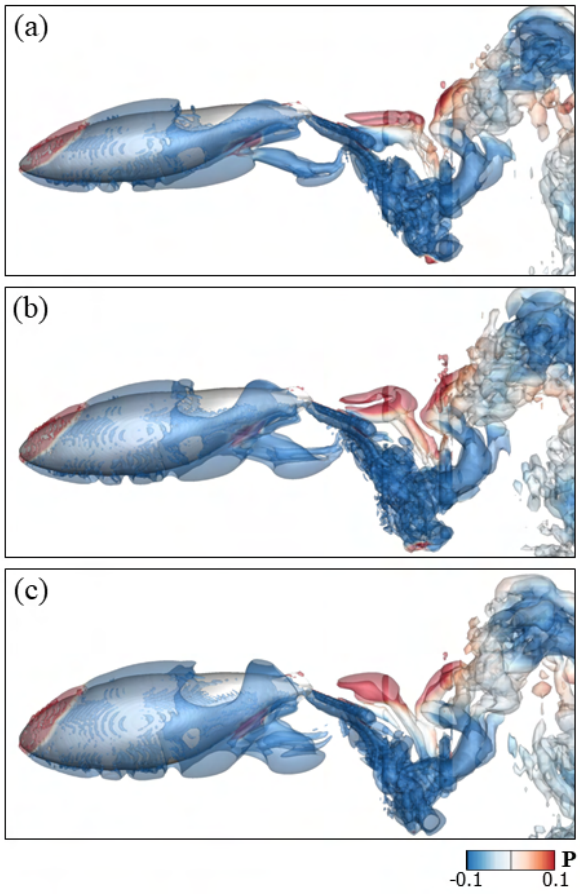

FIGURE 5.21: Vortex wake structures at t/T = 0.25 from the top view for thicknesses of 0.188L, 0.225L, and 0.252L. The iso-surfaces are plotted with a Q-criterion of Q = 40 and colored by the pressure.

flow separation region grows, the low pressure resulting from this circulating flow region interacts with the posterior portion of the Tunabot body, creating a suction force that increases the total drag. Additionally, at this timestep, the body is flapping away from this low-pressure region, so more power is consumed by its presence. This causes an overall increase in both power and drag for the thicker body shape.

Joints 1 & 2	$\overline{C_T}$	$\overline{C_{pw-cf}}$	$\overline{C_D}$	$\overline{C_{pw-bd}}$
Baseline (J_1=1.0, J_2=1.0)	0.47	1.84	0.47	0.65
J_1=0.75, J_2=1.0	0.32	1.29	0.46	0.59
J_1=0.50, J_2=1.0	0.20	0.94	0.46	0.55
J_1=0.25, J_2=1.0	0.11	0.74	0.44	0.52
J_1=1.0, J_2=0.75	0.44	1.64	0.46	0.63
J_1=1.0, J_2=0.50	0.42	1.50	0.46	0.62
J_1=1.0, J_2=0.25	0.39	1.35	0.46	0.61
J_1=0.75, J_2=0.75	0.30	1.16	0.46	0.58
J_1=0.50, J_2=0.50	0.16	0.75	0.44	0.54
J_1=0.25, J_2=0.25	0.06	0.53	0.43	0.51

TABLE 5.4: Cycle averaged coefficients of thrust, drag, and power on the body for each body kinematics.

5.2.3.3 Changing Body Joint Angles

In this section, the hydrodynamic performance, vortex, and wake structures are observed when decreasing the body flexibility central to the performance gains demonstrated in White et al. [10]. By decreasing joints 1 and 2, the impact of body flexibility is lessened and the flow impacts can be studied while maintaining a relatively high tail amplitude by maintaining joints 3 and 4. To scale the joint angles, the virtual joints along the virtual skeleton in the model are scaled to a percentage of the values given by the reconstruction. A summary of the cycle-averaged results is given in table 5.4.

In the table, a reduction in the body flexibility is seen to significantly affect the performance. Reductions in joint 1, with or without a change to joint 2, significantly hindered the thrust produced by the caudal fin. The resulting power savings and body drag reduction were minimal, leading to a drop in Froude efficiency. Reductions to joint 2 alone, however, did result in up to 5% efficiency benefit for the case J_1=1.0, J_2=0.25. This occurs due to a large drop in caudal fin power consumption, accompanied by a

slight drop in body power, with only a small detriment to the total thrust production.

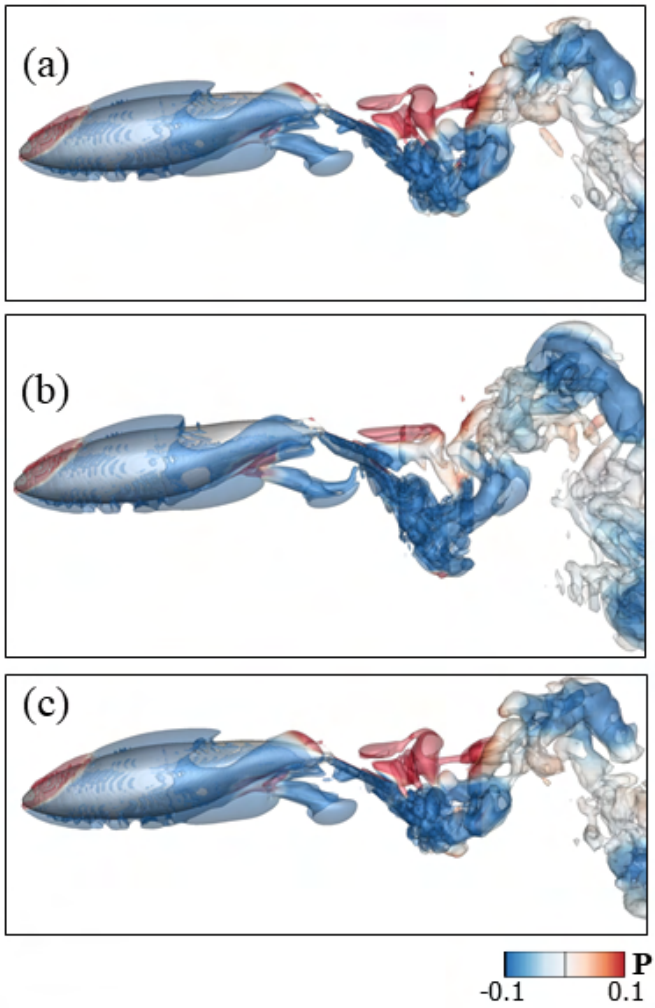

FIGURE 5.22: Vortex wake structures at t/T = 0.25 from the top view for J_1=0.50, J_2=1.0 (a); J_1=1.0, J_2=0.50 (b); and J_1=0.50, J_2=0.50 (c) at t/T = 0.25. The isosurfaces are plotted with a Q-criterion of Q = 40 and flooded by the pressure.

In order to understand the difference between decreasing the joint angles 1, 2, and both 1 and 2, Q criterion isosurfaces are plotted in Fig. 5.22. Comparing to the baseline flow in Fig. 5.19, the wake narrows significantly when joint 1 is reduced. The larger lateral expansion of the wake in the baseline is observed when only joint 2 is reduced. Finally, the wake has significantly narrowed when both joint angles are reduced, along with

significantly less buildup of vortex tubes occurring on the caudal fin.

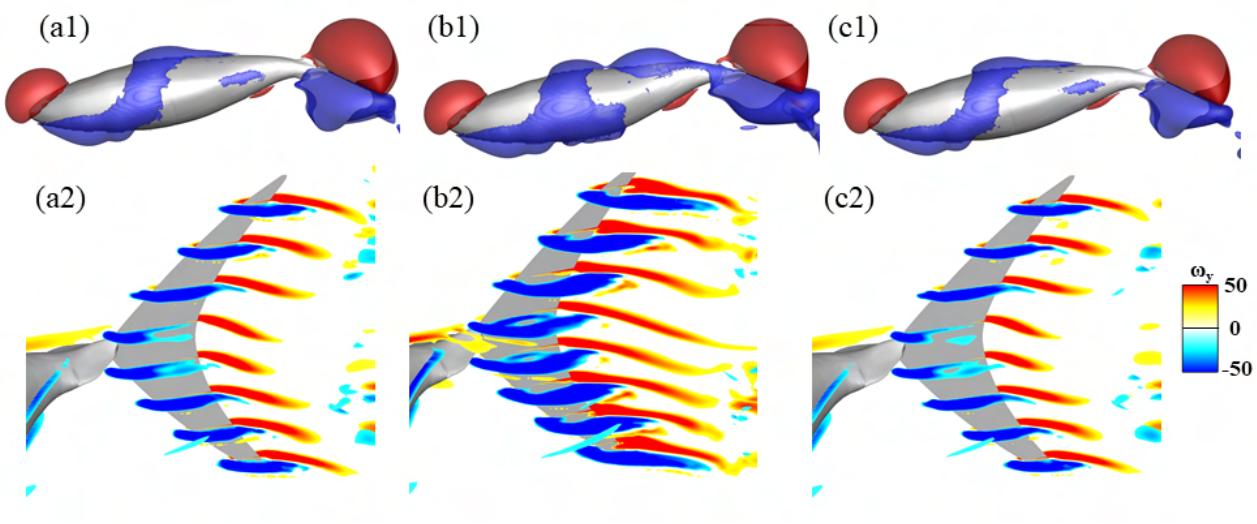

FIGURE 5.23: Pressure isosurfaces with red indicating regions of high pressure and blue indicating regions of low pressure (top) and y-vorticity at the tail (bottom) for J_1=0.50, J_2=1.0 (a); J_1=1.0, J_2=0.50 (b); and J_1=0.50, J_2=0.50 (c) at t/T = 0.25.

To investigate further, pressure isosurfaces, along with slice cuts of the y vorticity ω_y are plotted for J_1=1.0, J_2=0.50; J_1=0.50, J_2=1.0; and J_1=0.50, J_2=0.50 at the thrust peak in the cycle, t/T = 0.25, in Fig. 5.23. From the figure, a more favorable low pressure region along the body is observed when joint 1 is maintained at 1.0 (Fig. 5.23(b1)). By observing the y-vorticity, a leading edge vortex is observed in each case. The strength of this vortex, however, is significantly reduced when joint 1 is reduced, leading to a large drop in thrust production. A stronger favorable pressure gradient across the caudal fin is observed when the leading edge radius is enhanced, producing more thrust. Because of this, the reduction in joint 1 is highly detrimental to the performance of the caudal fin.

5.2.3.4 Addition of Median Fins

Finally, simulations are completed analyzing the effects of adding median fins to the Tunabot body. Significant biological-focused research has demonstrated the propulsive performance benefits available from the addition of median fins in fish-like swimming [84], [85], [110], [124]. The designs used in this section are detailed in Fig. 5.16. For each case, the midline kinematics are matched to the original reconstructed motion of the Tunabot. The fins move rigidly with the segment of the body they are attached to.

	$\overline{C_T}$	$\overline{C_{pw-cf}}$	$\overline{C_D}$	$\overline{C_{D-mf}}$	$\overline{C_{pw-mf}}$	η
No median fins	0.8858	7.4760	0.2837	n/a	n/a	0.1059
Basline fins	0.9962	7.5516	0.2850	0.0183	0.1473	0.1294

TABLE 5.5: Cycle averaged coefficients of thrust, drag, and power on the body and fins for the Tunabot model with (Fig. 5.16(d)) and without median fins (Fig. 5.16(a)).

The forces and power consumption for the Tunabot models with (Fig. 5.16(d)) and without (Fig. 5.16(a)) median fins is given in Table 5.5. In the table, it is observed that the thrust on the caudal fin gains over 12 % thrust enhancement from the addition of the median fins. There is a subsequent increase in the caudal fin power consumption, and the median fins add drag and power consumption to the system, but the benefits from thrust increase outweigh the increases in power. The net propulsive efficiency benefit from the addition of tuna-modeled median fins is 22%.

To understand these benefits, the flow is plotted in Fig. 5.24. In the figure, the advection of the vortices from the median fins interacts with the caudal fin. The instantaneous pressure slice shown through the caudal fin in the figure shows that an additional low pressure region is generated by the median fin. This low pressure region

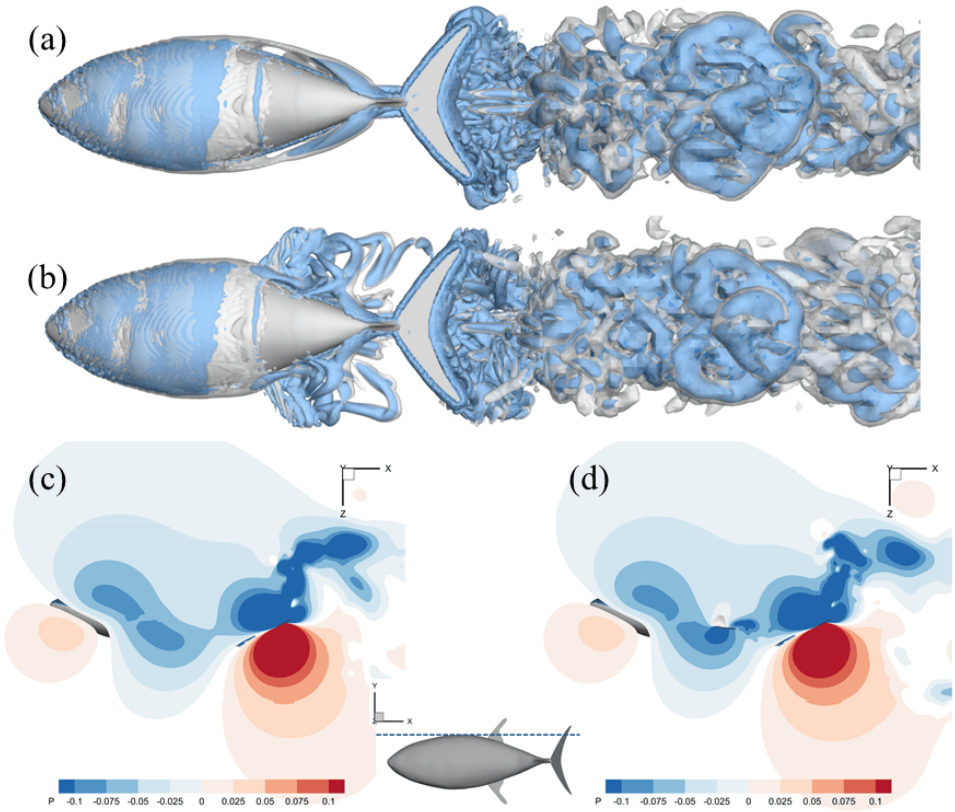

FIGURE 5.24: Q criterion isosurfaces (a-b) and pressure slice cut (c-d) for no median fins (a,c) and with median fin (b,d) Tunabot models.

enhances the low pressure suction side of the caudal fin, increasing the total thrust produced by the caudal fin. Unlike previous works [84], [110], [124] no leading edge vortex enhancement on the caudal fin from the vortex interaction between the median and caudal fin is observed. In this fin configuration, there is no median fins occupying the posterior portion of the body closest to the tail, creating a combined posterior body vortex and median fin vortices. This also prevents the body drag reduction effects observed due to the altering of the posterior body vortex that is observed in these previous fish-based studies. Despite these shortcomings, the low-pressure enhancement offered by the median fin still significantly enhances the performance.

Next, the forces and power consumption for the Tunabot model with a varying median

Median Fin Position	$\overline{C_T}$	$\overline{C_{pw-cf}}$	$\overline{C_D}$	$\overline{C_{D-mf}}$	$\overline{C_{pw-mf}}$	η
A (Anterior)	0.9013	7.4300	0.3054	0.0344	0.1045	0.1196
B	0.9714	7.7284	0.3040	0.0215	0.1249	0.1237
C	0.9962	7.5516	0.2850	0.0183	0.1473	0.1294
D (Posterior)	1.0150	7.5741	0.2625	-0.0032	0.1791	0.1309

TABLE 5.6: Cycle averaged coefficients of thrust, drag, and power on the body and fins for the Tunabot model with varying medain fin position(Fig. 5.16(c)).

fin position along the body as shown in Fig. 5.16(c) are provided in Table 5.6. Unlike the baseline fin, moving the fin toward the anterior introduces additional body drag, but reaches a maximum 7% increase for case B and does not continue further in case A. Conversely, moving the median fins posteriorly decreased body drag by 8%. Similarly, the thrust on the caudal fin progresses from a slight enhancement over no median fins in position A to increased enhancement over the baseline in position D. Finally, the drag produced by the median fins increases as the median fins shift toward the anterior.

The flow, visualized by isosurfaces of the Q criterion, is plotted for fin positions A, B, and D in Fig. 5.25. In the figure, the interactions between the median fins and the caudal fin is greater when the median fins are positioned closer to the posterior of the body. In position A, the wake structures have significantly further to travel to interact with the caudal fin, and the decreased body amplitude at position A generates weaker vortex structures overall. Conversely, position D produces much stronger median fin vortices, which also have less distance to travel before interacting with the caudal fin. This increased vortex interaction, along with closer proximity for the pressure effects

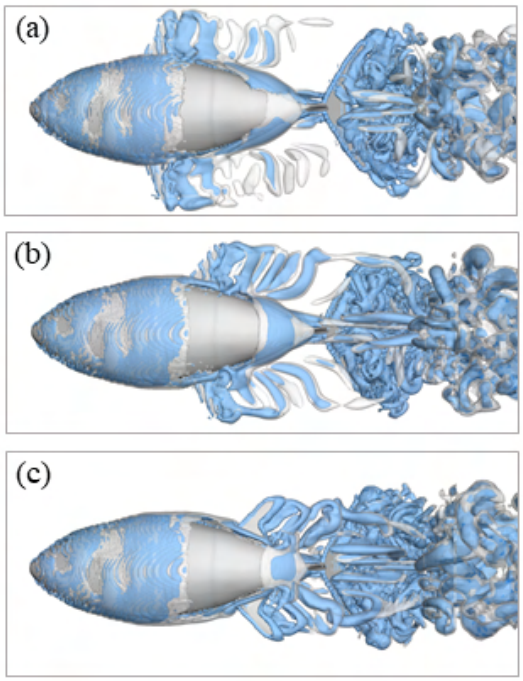

FIGURE 5.25: Q criterion isosurfaces for fin positions A (a), B (b), and D (c).

demonstrated in Fig. 5.24 can be attributed to the increase in caudal fin thrust generation. The posterior body vortex (PBV) also grows with a median fin closer to the head of the fish. This PBV creates a lower-pressure region along the body, which generates additional drag on this portion of the body. Finally, as the median fin amplitude increases in the later positions along the body, its amplitude increases, decreasing the drag produced by the fin and even turning to thrust in position D. This runs counter to the results of Guo et al. [124], which finds that there is a peak location for the median fins that they should not be displaced from. Moving the anal fin closer to the tail increased the drag on the body. In their study, the body surface is generally parallel to the incoming flow along the bottom of the body where the anal fin is located. In the tuna-like shape used in the Tunabot Flex, however, the latter half of the body surface

on the top/bottom of the fish points partially in the $-x$ direction. This means interrupting the vortex generation on this surface is the best way to decrease body drag, and moving the dorsal and anal fin back maximizes this effect.

Fin Size	$\overline{C_T}$	$\overline{C_{pw-cf}}$	$\overline{C_D}$	$\overline{C_{D-mf}}$	$\overline{C_{pw-mf}}$	η
Baseline	0.9962	7.5516	0.2850	0.0183	0.1473	0.1294
Decreased height	0.9848	7.5541	0.2839	0.0149	0.1183	0.1283
Increased height	0.9859	7.5739	0.2923	0.0070	0.1442	0.1277
Decreased width	0.9764	7.5818	0.2863	0.0185	0.1361	0.1265
Increased width	1.0057	7.5513	0.2813	0.0166	0.1658	0.1303

TABLE 5.7: Cycle averaged coefficients of thrust, drag, and power on the body and fins for the Tunabot model with varying medain fin height (Fig. 5.16(e)) and width (Fig. 5.16(b)).

Next, the effects of median fin size are studied. The height and width of the dorsal and anal fin are varied as demonstrated in Fig. 5.16(b,e). The forces on the fins and body along with power consumption are provided in Table 5.7. Changes to the fin height are not found to be beneficial. Increasing median fin height allows a larger amplitude for their flapping motion, as the fins point partially in the downstream direction. This results in a decrease in drag produced by the median fin, as the larger flapping amplitude counteracts the drag increase from a larger median fin. However, the power consumed by the median fin is significantly increased with the median fin height increase, and the overall efficiency of the motion is decreased. In the fin width, no significant efficiency benefits can be gained from an increase or decrease in fin size. A wider fin does increase the pressure region that then enhances the caudal fin thrust, as shown in Fig. 5.24. This increase, however, also increases the power consumption by the median fins, and leads to no net benefit for the efficiency. Similarly, decreasing fin thickness can decrease power consumption, but lessens the thrust benefit from

the median fin-caudal fin interaction. Overall, adjustments in median fin size are not found to significantly impact performance, and the size modeled after the yellowfin tuna is also found to be the best selection for the tuna-like robotic platform.

Fin Size	$\overline{C_T}$	$\overline{C_{pw-cf}}$	$\overline{C_D}$	$\overline{C_{D-mf}}$	$\overline{C_{pw-mf}}$	η
No Fin Band	0.9962	7.5516	0.2850	0.0183	0.1473	0.1294
Small Fin Band	0.9857	7.5982	0.2512	0.0203	0.1511	0.1237
Medium Fin Band	0.9815	7.6205	0.2480	0.0207	0.1528	0.1225
Large Fin Band	0.9965	7.6170	0.2469	0.0209	0.1530	0.1238

TABLE 5.8: Cycle averaged coefficients of thrust, drag, and power on the body and fins for the Tunabot model with varying fin band sizes (5.16(f)).

Finally, the effects of using a segmented fin band, as shown in Fig. 5.16(f) are tested by varying fin band size. The middle fin band is modeled in size after the individual finlets found to be beneficial in tuna swimming **wang2020** but combined into a single fin for practical purposes in a robotic setting. This more closely mirrors the fin shapes found to be beneficial by previous studies of the jackfish and sunfish [69], [84]. The forces on the fins and body along with the power consumption are shown in Table 5.8. From the table, it is seen that the addition of a fin band does not significantly impact the thrust production benefits of the median fin on the caudal fin. It also does not significantly add to the total drag increase from the median fins. It does reduce the body drag by about 12%, with only a slight increase in the drag reduction for the larger fin band sizes. Consistent with the results of the sunfish and jackfish, each of which has a thin fin band behind the dorsal and anal fin, the fin band prevents the posterior body vortex from crossing the midline of the body. When the PBV crosses this midline, it decreases body drag. By keeping the left and right stroke PBV's from interacting, the fin band allows for a pressure buildup on each side to help alleviate body drag.

5.2.4 Section Summary

In this section, the hydrodynamics of forward steady swimming in a flexible tuna-like robotic platform is studied numerically. The hydrodynamic performance and vortex dynamics are examined in detail, revealing the effects of the body joints on the thrust-producing leading-edge vortex. It is found that in the Tunabot flex, the caudal fin consumes a lower portion of the overall hydrodynamic power at only 75% compared to a rigid body [120]. The wake forms a wide reverse Kármán vortex wake composed of interconnected rings, consistent with the rigid body. The lateral deflection of the wake, however, is significantly increased by additional body joints. It is found that increasing the body thickness causes an overall increase in the drag, however, the detrimental effects are accelerated by large flow separation from the body when the body reaches a critical width of around 23% of the body length. Finally, by reducing flexion in the mid-body, some benefits to power consumption and efficiency were observed, however significant costs in thrust production follow, and large reductions in mid-body joints significantly hinder performance.

These results suggest that in this flow regime body thickness can be increased in robotic platforms below a threshold of around 23% of the body length before a steep increase in body drag is experienced. Also, adding body joints to a robotic platform will improve performance by enhancing leading-edge vortices and generating more favorable pressure gradients on the caudal fin. Larger amplitude joints can be focused around the mid-body and peduncle, however some flexion in the rest of the posterior body is

still critical to obtaining these benefits. The addition of median fins offers significant performance benefits to the system by increasing the thrust produced by the caudal fin. Adding a smaller fin band behind the dorsal and anal fin offers further benefits by reducing the body drag. These results help us to develop an understanding of morphological effects in bio-robotic swimming, serving as a baseline for future studies of schooling and informing future robotic design.

6 Body Shape Effects in Fish Schools

6.1 Shape Effects in a 2D Diamond School

To examine the effect that body shape plays in the interactions between fish in a dense school, fish-like undulating foils are numerically studied in a high-density diamond school. Shape parameters of leading edge radius, boattail angle, and maximum thickness location along the body are independently varied to control the body shape. A traveling wave is prescribed to the body, and the flow around the school is solved using an immersed boundary method-based incompressible Navier-Stokes flow solver. Our findings indicate that body shape does play a significant role in the performance of the school and varies school efficiency and thrust productions by as much as 7% and 40%, respectively. It also changes the efficiency in individual swimmers within the school by up to 25%. The leading edge radius drives the scale of the anterior body suction experienced throughout the school. A rounder leading edge generates more suction but consequently consumes more power. Changes to the location of the maximum thickness along the foil significantly impact the wall effect in the school by changing the shape of the "wall." A maximum thickness that occurs at or in front of the closest point of interaction between the body and tail is favored. Finally, changes

to the boattail angle manipulate the shape of the active channels in the school altering vortex-body interactions and the wall effect. A large boattail angle leads to a pinching that prohibits significant flow in the channels, reducing performance.

6.1.1 Problem Statement

6.1.1.1 Geometric Configuration of Body Shapes

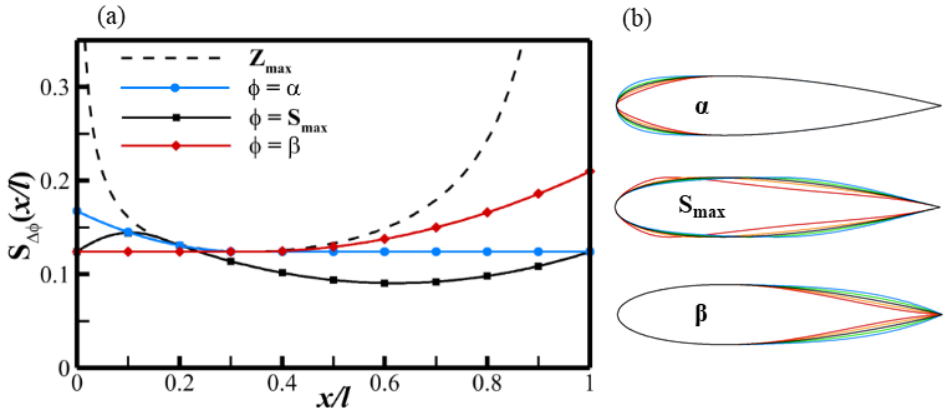

FIGURE 6.1: (a) Z_{max} function, along with shape functions for changing α, S_{max}, and β independently. (b) Range of body shapes created by varying each parameter individually.

To systematically study the effect of body shape within the school, a methodology that independently varies fundamental geometric foil shape parameters is required. For this study, the selected parameters are the leading edge radius (α), the location of the maximum thickness along the foil (S_{max}), and the boattail angle (β), based on previous study of a solo swimmer [71]. A class shape transformation is used to define the foil shape [108], [109], which defines the curve of the foil as:

$$y(x) = x^{N_1}(1-x)^{N_2}S(x) \tag{6.1}$$

In this method, a class function $x^{N_1}(1-x)^{N_2}$ is used to define a general class of shapes and the shape function $S(x)$ allows for a modification of the shape with a small number of parameters while maintaining the overall geometry of the class. In this study $N_1 = 0.5$ and $N_1 = 1.0$, giving the airfoil class. The shape functions are based on the Z_{max} function, which is defined by the transformation of a line at the point of maximum thickness into shape function space. To change the leading edge radius (α) while holding other parameters constant, the shape function $S_{\Delta\alpha}(x)$ varies the value of $S(0)$ and follows a quadratic equation tangent to the Z_{max} curve at the maximum thickness point. For changes in boattail angle (β), the shape function $S_{\Delta\beta}(x)$ varies the value of $S(1)$ and follows a quadratic equation tangent to the Z_{max} curve at the maximum thickness point. Finally, for changes in the location of maximum thickness (S_{max}), the point at which the shape function $S_{\Delta S_{max}}(x)$ is tangent to the Z_{max} curve is changed. More details can be found in Kulfan [108], [109]. In each of the cases, the shape parameter change is controlled by a single variable, and all other shape parameters are held constant. Figure 6.1(a) shows the Z_{max} function, along with an example shape function for an increase in α, β, and S_{max}. To test the full parameter space, each shape parameter is varied between the minimum and maximum value it can be while keeping the other shape parameters constant. The resulting set of foil shapes are shown in Figure 6.1(b). By using a class shape transformation function, shape parameters can be varied independently while maintaining a continuous shape that stays within the general class of airfoil shapes. It has also been proven in many previous studies of foil shape design [110], [125].

6.1.1.2 Undulating Swimmer Kinematics and Diamond School Configuration

To create a fish-like motion for the study, traveling wave kinematics are imposed on a foil. The resulting undulatory motion mimics a top-down view of fish swimming. The body length is used as the unit length for the simulations ($l = 1$) and is constant for all body shapes. The lateral displacement is defined by the following equations:

$$y(x,t) = A(x)\sin(\frac{2\pi}{\lambda}x - \frac{2\pi}{T}t) \tag{6.2}$$

$$A(x) = a_2x^2 + a_1x + a_0 \tag{6.3}$$

where y represents the lateral displacement located at x position along the body at time t. λ is the wavelength of the traveling wave over the body and T denotes the period of the undulating motion, both of which are set to one. To create carangiform-like swimming, the amplitude $A(x)$ is defined by the quadratic polynomial in Eq. 3, and the coefficients are set to $a_0 = 0.02$, $a_1 = -0.08$ and $a_2 = 0.16$ to mimic carangiform swimming [95]. The wave amplitude envelope and midline through a cycle are shown in Fig. 6.2(b). This methodology is common for reproducing biological swimming motions [100].

To arrange the fish in a basic schooling configuration that maximizes interaction, a dense diamond formation is utilized. The diamond formation has been utilized in a large range of schooling studies for its high energy efficiency [15], [26], [52], [94]. Additionally, Pan et al. [23] show that the dense spacing with 0.4l spacing between

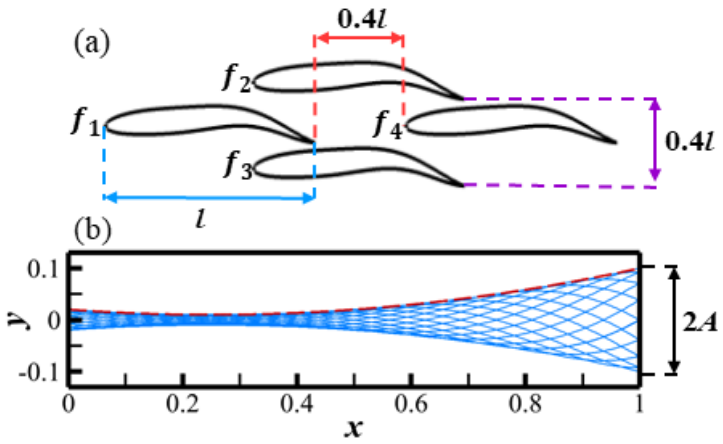

FIGURE 6.2: (a) Schematic of high-density diamond-like fish school arrangement. (b) The traveling wave amplitude envelope of carangiform motion (red dashed line) and sequenced midlines of the fish body during one tail-beat period (blue lines). A is the lateral motion amplitude at the tail tip.

fish maximizes the beneficial interactions within the school. To study the effects of body shape on the most efficient schooling interactions, we utilize this same dense diamond school arrangement. A schematic of the arrangement used in this study is shown in Fig. 6.2(a). To differentiate between individual fish within the school, each fish is numbered left to right, top to bottom, as indicated in the figure.

6.1.2 Simulation Setup

A schematic of the non-uniform Cartesian grid and boundary conditions used in the simulation is presented in Fig. 6.3(a). The computational domain size is chosen to be $16l \times 10l$ with 1410×770 grid points, approximately 1.1 million in total. The minimum grid spacing is 2.4×10^{-3} l everywhere around the fish bodies. A detailed inset of the grid around the head of the fish is shown in Fig. 6.3(a). The fish are swimming to the left, with a constant incoming flow velocity of U_∞ at the left-hand boundary.

An outflow boundary condition is assigned to the right-hand side and zero gradient boundary conditions on the lateral boundaries. All boundaries are treated with a homogeneous Neumann boundary condition for pressure. To ensure the accuracy of the grid, a mesh dependence study is shown in Fig. 6.3(b), using coarse ($\Delta_{min} = 0.003l$), nominal ($\Delta_{min} = 0.0024l$), and fine ($\Delta_{min} = 0.0019l$) grid spacings. Because smaller β gives a thinner tail geometry that requires a finer grid to accurately capture, the body shape with the smallest β is utilized for the grid study. The instantaneous net forward force is shown. The difference in peak C_x value between coarse and fine meshes is 6.0%, while the difference between the nominal and fine meshes is 0.7%. This demonstrates that the results on the nominal grid are grid-independent.

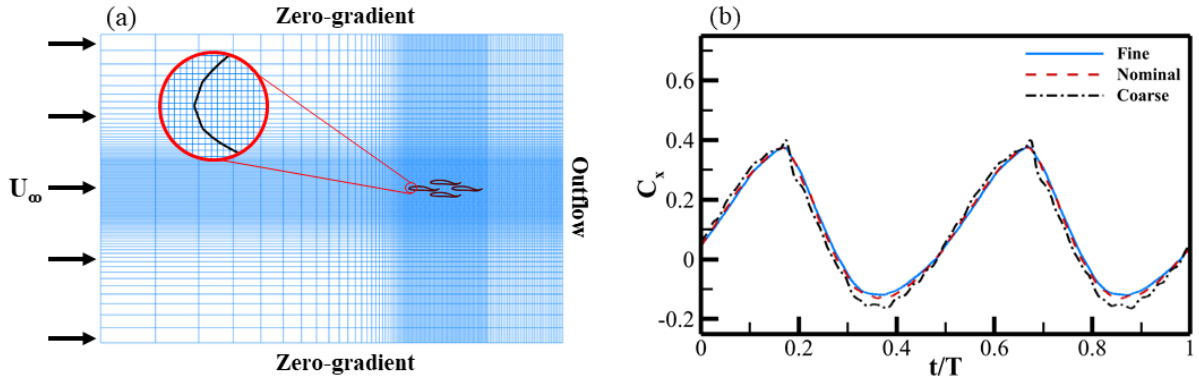

FIGURE 6.3: (a) Schematic of the computational domain, Cartesian grid, and boundary conditions. A detailed inset of the grid on the body is included. (b) Comparison of instantaneous net force coefficients for the foil ($\beta = 3.0$) obtained through coarse ($\Delta_{min} = 0.003l$), nominal ($\Delta_{min} = 0.0024l$), and fine ($\Delta_{min} = 0.0019l$) grid spacings.

In this work, two key dimensionless parameters, Reynolds number (Re) and Strouhal number (St) describe the hydrodynamic characteristics of the flow. Reynolds number is defined as $Re = U_\infty l/\nu$ where ν denotes the kinematic viscosity. For this study, the Reynolds number is set to Re=1000, consistent with prior studies of 2D carangiform

swimming [15], [23], [77] and corresponding with higher Reynolds numbers in three dimensions [93]. In this flow regime, the viscous effects are small while still maintaining coherent vortex structures [81]. Additionally, it was shown in Kelly et al. [15] that in dense planar schooling, the wake structures and performance remain similar as the Reynolds number is increased. The Strouhal number is defined as $St = 2fA/U_\infty$, where $f = 1.0$ is the tailbeat frequency. The Strouhal number is set to St=0.43, which balances the thrust and drag to achieve a steady swimming condition of a net-zero force over a cycle of motion. This gives an incoming velocity of $U_\infty = 0.465$ l/cycle. Details on the Strouhal number selection can be found in Pan and Dong [23].

6.1.3 Results

6.1.3.1 Baseline Foil Shape

To begin the study, the baseline foil shape formed by the class function and undeformed by any shape function (Eq. 3) is observed in solo swimming and the diamond arrangement. The cycle-averaged performances are shown in the table below.

	$\overline{C_x}$	$\overline{C_{pw}}$	η
Single	-0.003	0.273	0.441
School	0.069	0.361	0.557

TABLE 6.1: Cycle averaged force, undulating power, and efficiency for a solo swimmer and diamond school with the baseline body shape.

First, the single fish net force in the x direction of (C_x) = -3.3x10^{-3} and in the y direction of C_y = -8.1x10^{-4}, which are very close to zero, proving that the Strouhal number chosen does give a steady swimming condition. The school average experiences significantly more undulating power consumption than the solo swimmer (+32%), however,

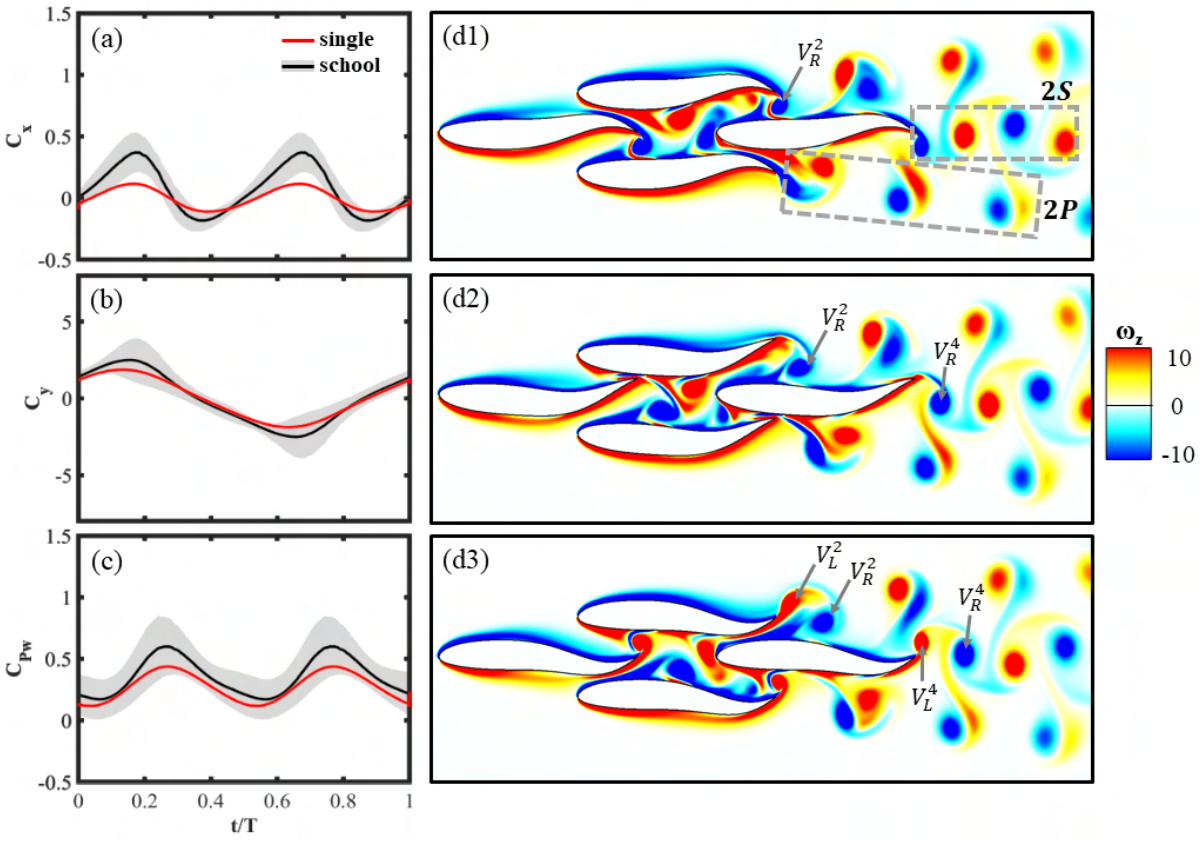

FIGURE 6.4: Time history of hydrodynamic performance for the baseline shape single fish and dense diamond school (a-c). School values are shown using the school average, with the standard deviation shaded. Flow structures for the diamond school at t/T = 0.25 (d1), 0.50 (d2), and 0.75 (d3).

the thrust production is also improved, such that the total efficiency of the school is improved by 26%. To elucidate the variations in hydrodynamic performance between the school and the solo swimmer, time histories of C_x, C_y, and C_pw are shown in Fig. 6.4(a-c), respectively. The overall effect of schooling in a diamond is clear. The lateral forces are increased at the peaks via schooling, and the net forward force produced is increased at similar timesteps as well, around t/T = 0.2 and 0.7. Consequently, the undulating power consumption is increased at the peaks for the school compared to the solo swimmer, around t/T = 0.25 and 0.75.

The vortex structures from the baseline shape dense diamond school are presented in Fig. 6.4(d). Vortices are labeled based on the fish number that they generate from, along with the stroke that they generate from (left vs. right stroke). Fish 4 produces single vortices V_R^4 and V_L^4 through a cycle of motion, giving the center of the wake a 2S von Karman structure. At the edge of the school, V_R^2 rolls up along the body of fish 4, eventually getting pushed along as the tail of fish 2 moves inwards towards the body of fish 4. This creates a combined wake pair with V_R^2 and V_L^2, which moves along the school and outward from the centers. The wake pair creation in the diamond school is indicative of the wall effect, as noted in Pan and Dong [23]. The wall effect occurs when a flapping foil or tail is in close lateral proximity to a wall, resulting in increased thrust production during the flapping motion [97]. In the dense school, the body of another fish acts as a pseudo-wall structure, creating this effect. This vortex pair, occurring on both sides of the school, creates a 2P wake pair along the edges of the wake. The overall wake structure is consistent with that found in a dense synchronous diamond in Pan and Dong [52].

6.1.3.2 Hydrodynamic Performance of Varying Body Shapes

To understand the effect that body shape has on the hydrodynamic interactions within a fish school, simulations are completed using five of each shape parameter value (S_{max}, α, β) with the values defined previously. Each school is formed with all 4 fish maintaining the same shape. For comparison, a single fish with each of the body shapes is also simulated. Figure 6.5 presents the time-averaged hydrodynamic performance of each individual fish in the school, along with the school averaged and single fish

results. School results are grouped by location within the school as front (f_1), edge (f_2 and f_3), and back (f_4).

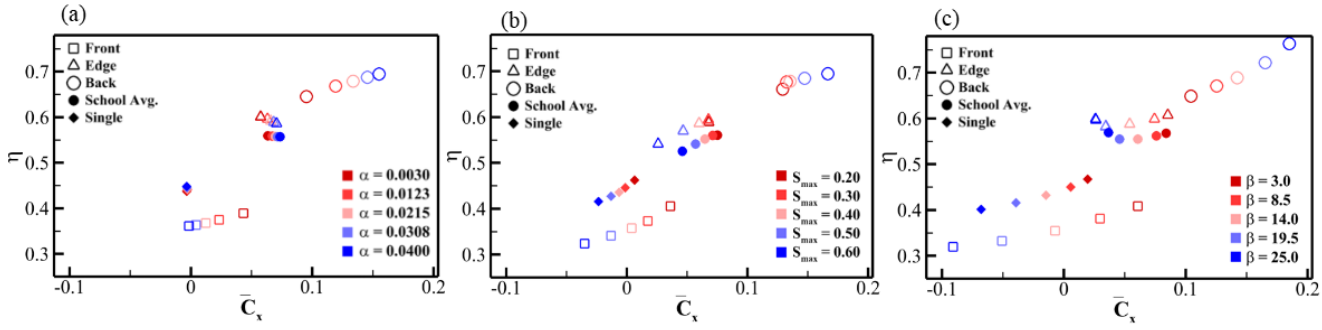

FIGURE 6.5: Cycle averaged force coefficient vs. efficiency for single fish and individual fish within a school with changing leading edge radius α (a), maximum thickness location S_max (b), and boattail angle β (c).

Figure 6.5(a) presents the cycle averaged force and efficiency for changing α. The single fish shows a slight decrease in efficiency as α increases. The school, on the other hand, shows the opposite trend, with the efficiency increasing as the leading edge radius increases. This trend is seen in both the edge and front fish, however, not the back fish. Additionally, the net force of the school increases as the leading edge radius increases. This trend is seen in both the edge and back fish, but not the front.

The results for changing S_max are presented in Fig. 6.5(b). In the single fish, there is a decrease in both efficiency and net force as the maximum thickness location moves closer to the back edge. The school follows similar results, with a more pronounced change for each. The front fish shows the most significant change, following the same trend. The edge fish have little change in performance, with the exception of a steep drop-off for the largest S_max values. The back fish also has little change in performance except the largest S_max values, however, these fish show the opposite trend, with a

maximum thickness location closer to the back of the fish is beneficial to both C_x and η. Finally, Fig. 6.5(c) presents the performance for changing β. The single swimmer experiences a significant decrease in C_x and a slight increase in η as β increases. The school average follows the same trend, along with the front and edge fish. The back fish shows the opposite, with C_x and η increasing as β increases.

6.1.4 Discussion

6.1.4.1 Effect of Leading Edge Radius (α)

To understand the mechanisms of interaction that reverse the trend of changing the leading edge radius from the solo swimmer to the school, an in-depth comparison is presented below. Figure 6.6 presents the time history of the hydrodynamic performance of f_1, f_2, and f_4 for the schools with α = 0.0030, 0.0215, and 0.0400. First, in Fig. 6.6(a), the net force for f_1 is shows a slight decrease at t/T=0.2 to 0.4 as α increases. f_2, on the other hand, has increased C_x from t/T = 0.5 to 0.7, as shown in Fig. 6.6(b). In Fig. 6.6(c), C_x in f_4 is significantly increased as α increases, with the peak value over the cycle 11% higher for α = 0.040 than α = 0.003.

The time history of the power coefficient is presented in Fig. 6.6(d-f). For the front fish, the undulating power consumed is consistently higher for larger α values, with a difference of 18% in the peak values. For the edge fish, a large difference occurs during the inward half stroke when the tail moves toward the center of the school. At the peak undulating power consumption (t/T = 0.25) the thicker leading edge radius

consumes 36% more power. Finally, the back fish shows alternating higher and lower power coefficients for the thicker leading edge radius.

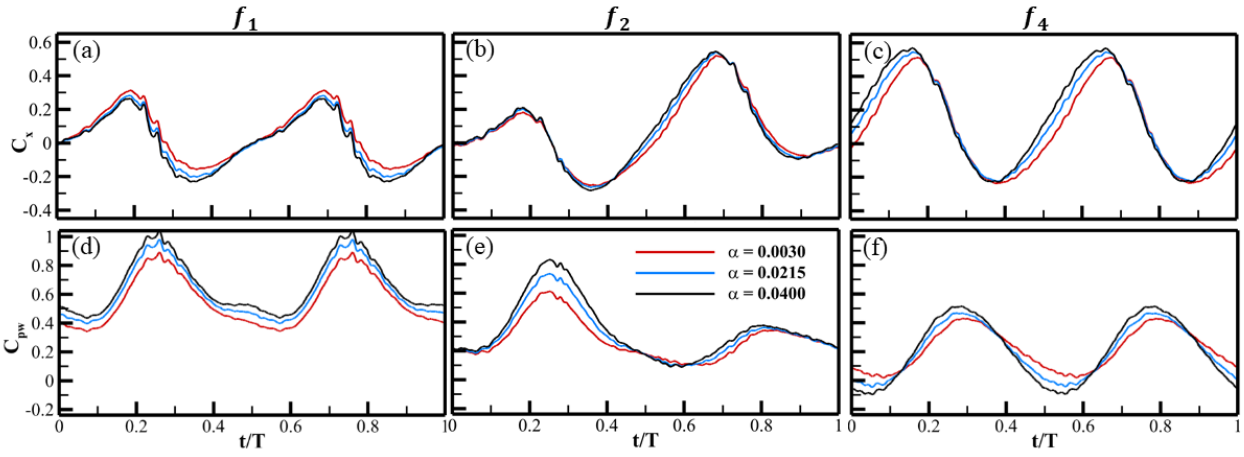

FIGURE 6.6: Time history of hydrodynamic performance for f_1, f_2, and f_4 with α = 0.0030, 0.0215, and 0.0400: (a-c) net force coefficient C_x and (d-f) undulating power consumption C_pw.

To understand the fluid physics behind the performance, the vorticity and instantaneous pressure around the α = 0.003 and α = 0.040 schools are shown in Figs. 6.7 and 6.8 at key times in the cycle identified by Fig. 6.6. The overall wake structure is similar to the baseline case, with 2P pairs generated on the edges of the school and a single vortex street shed behind the back fish. The primary differences come from the increased strength of the vortices coming from the head of the thicker leading edge radius fish, and the increased pressure at the head resulting from the thicker leading edge. This can most easily be seen in Fig. 6.8(b) and 6.8(d), where f_3 has a much larger head pressure. The pressure around the tail of the front and edge fish at t/T=0.25 (Fig. 6.8(a), 6.8(c)) is another significant difference resulting from changes in α. From the circled regions, it is observed that the low-pressure zone is significantly enhanced by a larger leading edge radius. Both of these low-pressure zones also have corresponding

secondary induced vortices, iV_L^{34} and iV_L^{13}. Vortices are named as the induced vortex $iV_{L/R}^{xy}$, generated between the tail of fish x and the head of fish y. These limit the speed of flow out of the channel created by neighboring fish and significantly modify the local pressure gradient.

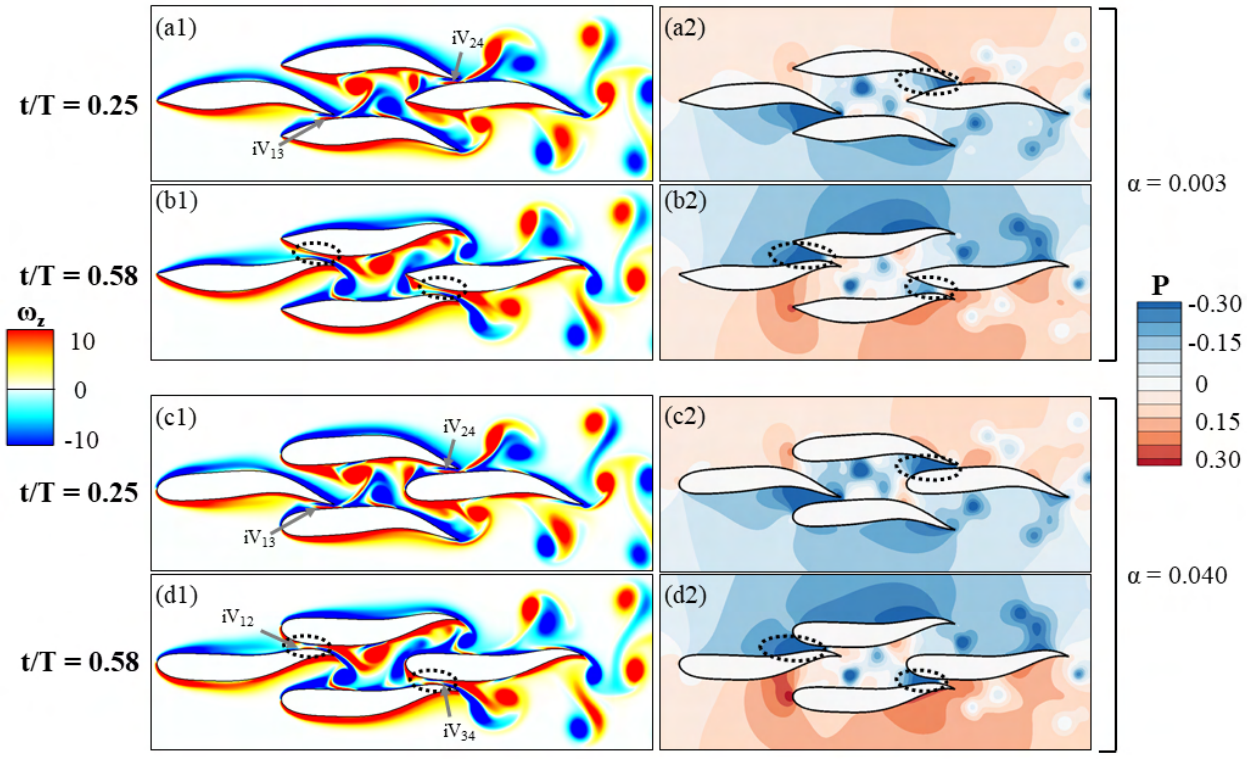

FIGURE 6.7: Vorticity for α = 0.003 and α = 0.040 at t/T=0.25 and 0.58.

An understanding of how the difference in these induced vortices occurs can be gained from observing the flow at t/T=0.58. At this timestep, a similar difference in the low-pressure zone is observed at the tail of f_1 and f_3, with the larger leading edge radius fish experiencing a significantly stronger low-pressure zone. At this time, the induced vortex iV_{12} and iV_{34} are strong in the α = 0.040 case, while they are nonexistent when α = 0.003.

This effect is due to the change in channel shape. Varying the leading edge radius causes a change to the entire front profile of the fish body due to the continuous nature of the shape definition. When the leading edge radius is increased, a long slender channel forms between the fish and the point at which they are in very close proximity extends over the last 15% of the fish's body length. Consequently, the secondary induced vortex occurs at the beginning of this channel and lasts as the undulation moves through to the tail tip. The $\alpha = 0.003$ case, however, has an hourglass-shaped channel, with the closest proximity occurring at only a single point at the tail tip. This results in the secondary induced vortex occurring for only a brief time at the very tip of the tail. These vortices influence the local pressure field and create the enhanced low-pressure zones observed.

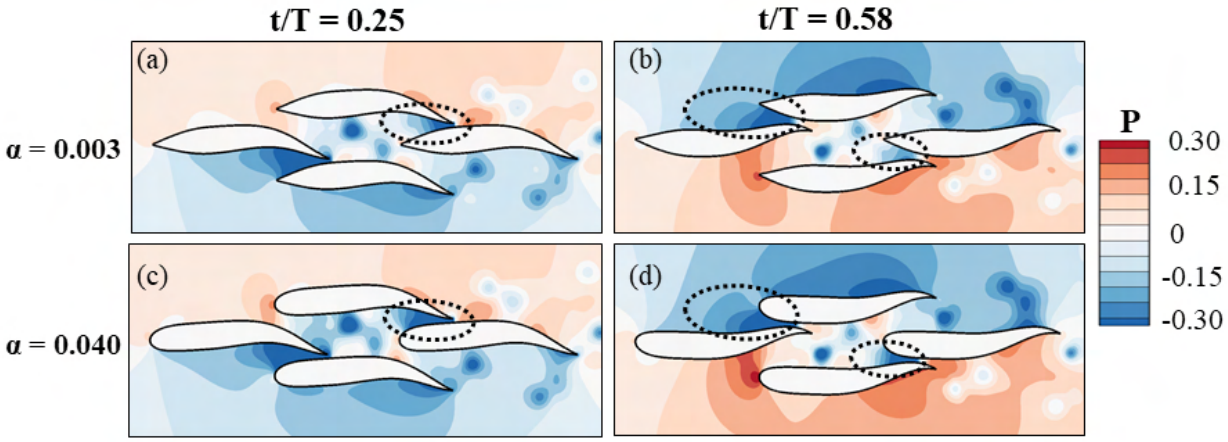

FIGURE 6.8: Pressure field for $\alpha = 0.003$ and $\alpha = 0.040$ at t/T=0.25 and 0.58.

To understand how these pressure field changes affect the performance of the school, the body positions and movement must be considered. With respect to thrust production at the head, many previous studies have indicated the importance of low-pressure suction on the head of later fish in a school to reduce drag in diamond and in-line

schools [15], [52], [126]. Following the definition of the anterior body from Kelly et al. [15], summing over the first 30% of the body length shows the following cycle average net force ($\overline{C_x^a}$):

	Front	Edge	Back
$\alpha = 0.003$	-0.003	0.049	0.062
$\alpha = 0.040$	-0.002	0.058	0.087

TABLE 6.2: Anterior body suction quantified by the cycle average net force on the first 30% of the body ($\overline{C_x^a}$) for each fish in the α = 0.003 and α = 0.040.

In the table, an 18% and 40% increase in the anterior body suction is observed for both the edge and back fish, respectively, when α is increased from 0.003 to 0.040.

Furthermore, to quantitatively compare the performance variations along the body, the cycle averaged net force and undulating power consumption are computed. The results are shown in Fig. 6.9, which displays ($\overline{C_x}$) and ($\overline{C_{pw}}$) along the body summed along 10% increments of the body length for f_1, f_2, and f_4, aligned with the undeformed body shapes along the bottom of the figure. At the first 10% of the body (the first set of bars), a sharp increase in thrust is seen in the edge and back fish as α increases. For the edge fish, a 3.6x increase is seen from α = 0.003 to α = 0.040. The back fish sees an increase of 2.3x for the same shapes. In the next two 10% increments, however, the opposite trend is observed and the smaller α values produce a higher thrust, though the difference is not as large as the first section. In Fig. 6.8(b) and 6.8(d), the back fish demonstrates a clear example of why this occurs. The enhanced low pressure in Fig. 6.8(d) creates a stronger effect, but the region of the body shape with a normal component upstream (i.e. a low-pressure zone would create thrust) is limited to the very front of the body. In Fig. 6.8(b), on the other hand, the weaker low-pressure zone

gives a reduced anterior body suction effect overall, but the shape of the anterior has a component of the surface normal pointing upstream throughout the anterior body, spreading out the total effects of the anterior body suction throughout the first 30% of the body length.

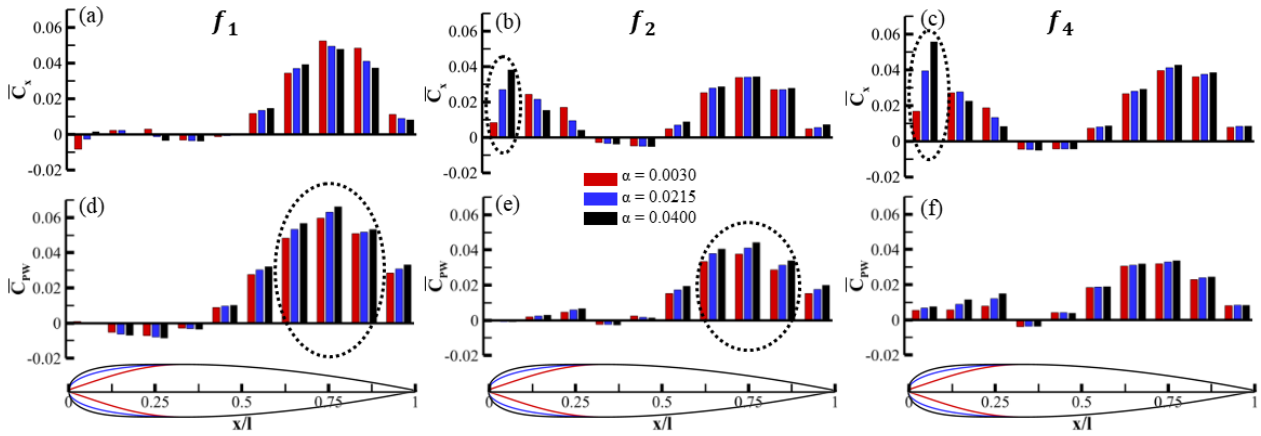

FIGURE 6.9: Cycle averaged net force $\overline{C_x}$(a-c) and power consumed for the undulation motion $\overline{C_{pw}}$(d-f) along each section of the body for α = 0.0030, 0.0215, and 0.0400. Results are shown for the front fish (a,d), edge fish (b,e), and back fish (c,f).

Figure 6.9(d-f) displays the undulating power consumption along the body of each fish. It is evident that f_1 and f_2 experience the most significant change in $\overline{C_{pw}}$, particularly along the back half of the body. In this region, the power coefficient is always higher for the thicker leading edge radius. While the effect of the secondary induced vortex enhanced low-pressure zones are beneficial to $\overline{C_x^a}$ in the α = 0.040 case, the effects of the low-pressure zone on the power consumption is not the same story. The undulating power consumed at the head of each fish, where the anterior body suction occurs, is typically very small, as observed in Fig. 6.9(d-f). At the corresponding tail, however, the tail has significantly more motion, and change to the pressure field has

profound effects on the performance. In these low-pressure regions, the secondary induced vortex increases the size and strength of the low-pressure zone and distributes it further along the fish's tail. When the anterior body suction occurs, the tail is starting to move away from the head of the nearby body, so a lower pressure requires more power for the undulating motion. Given this, it is expected that an increase in power consumption occurs throughout the latter part of both the front and edge fish. This is seen in Fig. 6.7(d-f), where the largest differences occur in the later portions of f_1 and f_2. Throughout this region, more power is consumed for undulating in the larger leading edge radius case. These results show a clear picture that the thicker leading edge radius leads to increased net force around the head of the edge/back fish, at the cost of increased power consumption near the tail of the front/edge fish.

6.1.4.2 Effect of Location of Maximum Thickness Location (S_{max})

To study the change in interaction that occurs due to altering the location of maximum thickness along the foil, a detailed comparison of the continuous hydrodynamic force and power for undulation are shown in Fig. 6.10. The figure presents the time history of the net force coefficient C_x and undulating power consumption C_{pw} for f_1, f_2, and f_4 with S_{max} = 0.20, 0.40, and 0.60. In the figure, the largest hydrodynamic performance differences resulting from changes in S_{max} occur in the front fish f_1. In the net force (Fig. 6.10a) the maximum thickness location closer to the tail shows a significant drop in force production at the peak, with a maximum value of about 1/3 the value for S_{max} = 0.60 compared to S_{max} = 0.20 at t/T = 0.19. At the same time, the undulating power consumption is also increased when the maximum thickness is located closer to the

trailing edge, increasing by 13% at the peak, occurring at t/T = 0.26. The difference between S_{max} = 0.40 and S_{max} = 0.60, however, is minimal. In f_2, similar results are observed as the tail flaps inwards towards the school, in the first half of the stroke. For this half stroke, more thrust is produced when the maximum thickness is closest to the leading edge. The power consumption for undulation also follows the same trend. Finally, f_4 shows an increased power coefficient when S_{max} = 0.20 at the peak of each half stroke.

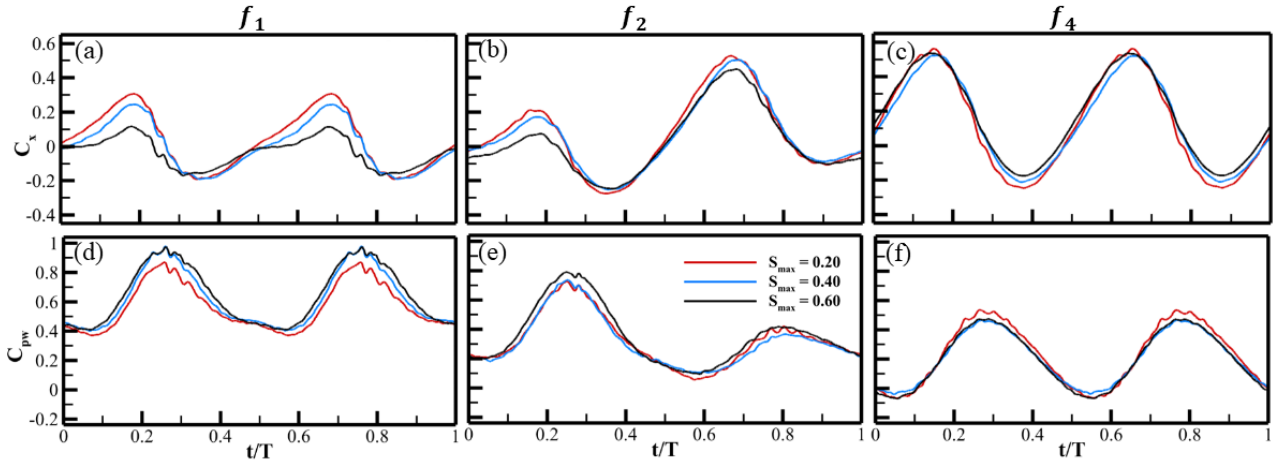

FIGURE 6.10: Time history of hydrodynamic performance for f_1, f_2, and f_4 with S_{max} = 0.20, 0.40, and 0.60: (a-c) net force coefficient C_x and (d-f) power consumption for undulation C_{pw}.

To explore the mechanisms behind this change in hydrodynamic performance due to a varying S_{max}, the vortex structures are shown in Fig. 6.11. The figure shows the vorticity for S_{max} = 0.20 (a-b) and S_{max} = 0.60 (c-d) where the hydrodynamic force (t/T = 0.19, a,c) and undulation power (t/T = 0.35, b,d) vary the most. Overall, the structure of the flow is similar despite changes in S_{max}, with a vortex pair V_L^2 and V_R^2 being generated at the peak force production time instance (t/T = 0.19). The flow close to the body shows increased separation and induced vortex generation in the

undisturbed portions of the top and edge fish for an S_{max} nearer to the leading edge, in agreement with the single fish study of Kelly et al. [71]. Additionally, the change in S_{max} significantly changes the shape of the active channel in the school. At S_{max} = 0.20, there is more space for the wake from f_1 to expand laterally within the channel, allowing the individual vortices to advect to one side of the leading edge of f_4, creating the circled vortex pair (Fig. 6.11(b)). At S_{max} = 0.60, on the other hand, the wider mid-body prevents significant lateral expansion of the wake from f_1, causing the head of f_4 to split the vortices preventing any similar vortex pair from forming.

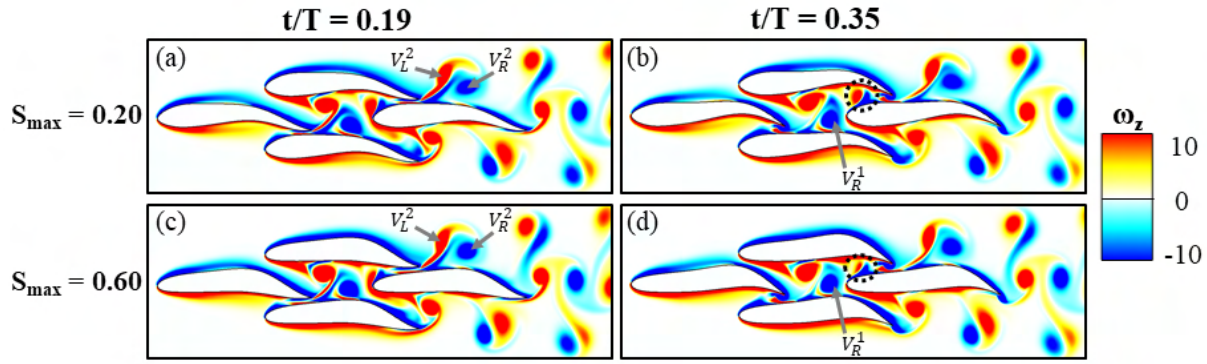

FIGURE 6.11: Vorticity at t/T = 0.19 and 0.35 for S_{max} = 0.20 and 0.60. Key vortices are noted.

Previous studies of dense diamond schooling formations have identified the creation of the 2P pair at the edge of the school, as is shown in V_L^2 and V_R^2 to be indicative of the performance-enhancing wall effect. This phenomenon occurs when a flapping foil is in close lateral proximity to a wall, directing momentum downstream and increasing thrust production [97], [98]. In a diamond school, this effect has also been shown, where the body of the next fish in the school acts as a wall near the tail of the swimmer [15], [23]. To fully demonstrate the difference in wall effect between the body shapes, the instantaneous x-velocity is shown in Fig. 6.12(a-b), along with the total momentum

produced by the instantaneous jet created during the wall effect in Fig. 6.12(c). The increased strength in this vortex pair is shown to create a stronger jet at the tail of fish 1 and 2, and the total momentum transfer downstream is seen in Fig.6.12(c). The figure shows a slight increase in momentum from S_{max} = 0.20 to S_{max} = 0.30, then a sharp decrease at each subsequent step. The case S_{max} = 0.30 corresponds the location of maximum thickness in the back fish to the exact furthest position along the tail of fish 2. The effect of this is seen in the overall performance of the school, which has an efficiency peak at S_{max} = 0.30 and an overall increase in the net force generated as S_{max} is reduced.

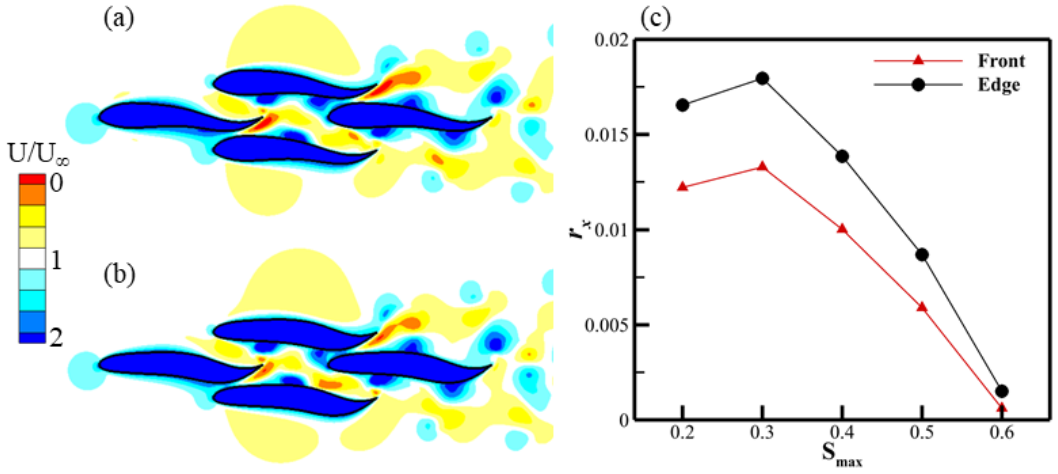

FIGURE 6.12: Instantaneous x-velocity at t/T = 0.1 for S_{max} = 0.2 (a) and 0.6 (b). Total momentum in the instantaneous velocity jet for each maximum thickness location, measured behind the front and edge fish (c).

Finally, a quantitative comparison of the forces and power consumption for undulation along the body is presented in Figure 6.13. The body is segmented into 10% increments along its length, and the force and power coefficients are summed within each segment and compared across S_{max} = 0.20, 0.40, and 0.60 for f_1, f_2, and f_4. The undeformed fish body shapes are given along the x-axis as a reference. Immediately the differences due

to the wall effect are apparent in the figure. The net force at x/l = 0.7 to 0.9 shows a significant increase as the maximum thickness moves closer to the leading edge, corresponding with the trend shown in Fig. 6.12(c). Subsequently, the power consumption by undulation for these regions is increased by a very small amount. These results clearly show that moving the maximum thickness closer to the leading edge provides an enhanced wall effect, increasing thrust production and efficiency in the school.

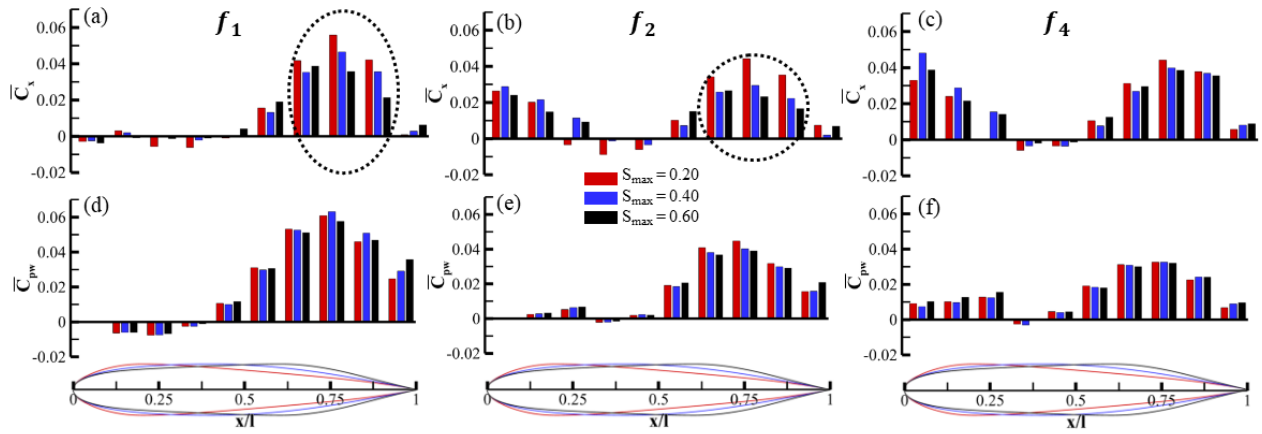

FIGURE 6.13: Cycle averaged net force $\overline{C_x}$(a-c) and power consumed by undulation $\overline{C_{pw}}$(d-f) along each section of the body for S_{max} = 0.20, 0.40, and 0.60. Results are shown for the front fish (a,d), edge fish (b,e), and back fish (c,f).

6.1.4.3 Effect of Boattail Angle (β)

Finally, to understand changes in the fish-fish interactions when changing the boattail angle in the diamond school, an in-depth comparison is presented below. Figure 6.14 presents the time history of the hydrodynamic performance of f_1, f_2, and f_4 for the schools with β = 3.0, 14.0, and 25.0. First, in Fig. 6.14(a/d), the net force for f_1 is shows a significant decrease at t/T=0.2 to 0.45 as β increases, with an increase in C_{pw} accompanying the decrease in net force. f_2 shows a similar decreased C_x from t/T =

0.2 to 0.5, along with an increased C_{pw}, as shown in Fig. 6.14(b/e). In Fig. 6.14(c/f) however, C_x in f_4 is increased as β increases, primarily around t/T = 0.05 to 0.2. The C_{pw} plot shows an increase in the peak undulation power consumption as β increases, but a subsequent decrease through the rest of the stroke.

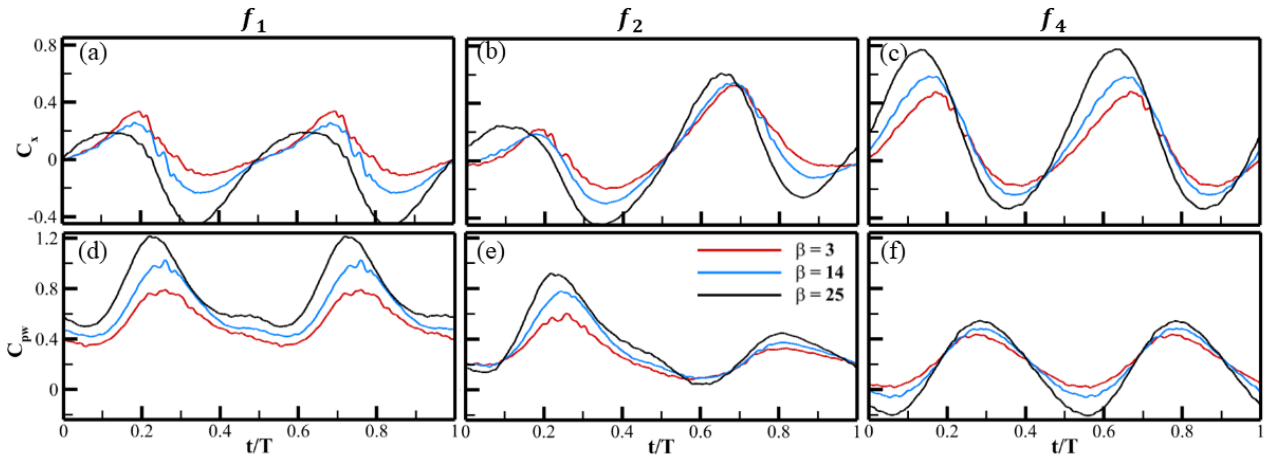

FIGURE 6.14: Time history of hydrodynamic performance for f_1, f_2, and f_4 with β = 3.0, 14.0, and 25.0: (a-c) net force coefficient C_x and (d-f) power consumption by undulation C_{pw}.

To better understand the flow physics involved in these performance changes, the vortices are visualized at key time frames by plotting the vorticity in Fig. 6.15. A few key features are noted. By changing the boattail angle, the shape of the channel between fish is significantly changed. In the thinner boattail angle, the closest that the tail of one fish gets to the body of the nearest subsequent fish in the school occurs only for a brief instant at the end of the stroke, and at a single point at the trailing edge of the fish. For a larger boattail angle, however, the larger aft body makes this closest interaction occur over a longer period of time and the close proximity occurs throughout the last 10% of the tail length. This severely restricts the amount of flow coming from the active channels between the fish as this is occurring, and disrupts some of the typical vortex

patterns expected in the schools. First, the interception of the wake of f_1 on f_4 in the channel is slowed, with V_L^1 being redirected at t/T = 0.09 to the bottom channel rather than the top. As this progresses along the body of the fish, the paired vortex noted at t/T = 0.25 on top of f_4 does not appear for the larger boattail angle.

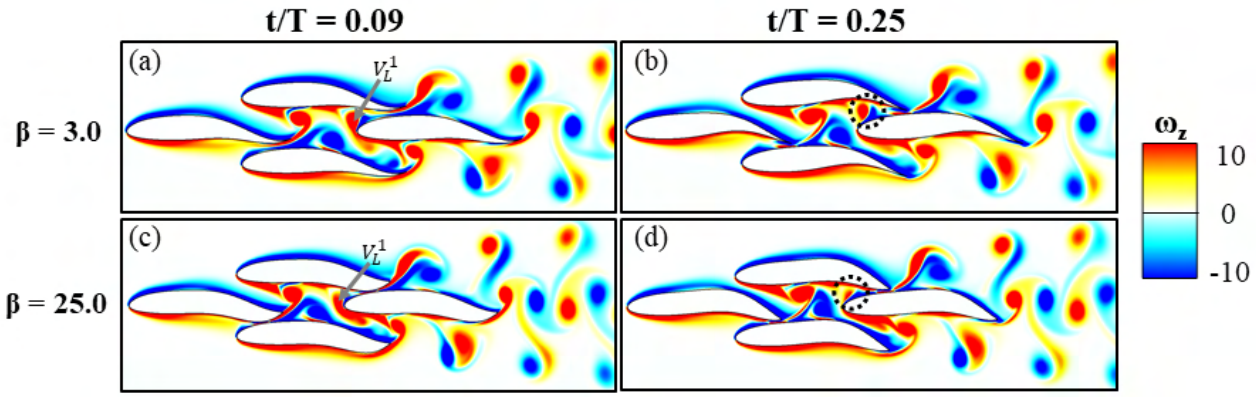

FIGURE 6.15: Vorticity at t/T = 0.09 and 0.25 for β = 3.0 and 25.0. Key vortices are noted.

In addition to these near-body flow changes, the wake is also significantly changed from changes in the boattail angle. The vortex wake and cycle averaged velocities are shown in Fig. 6.16. Instantly a significant difference in the streamwise spacing of the 2S wake core can be seen. When β = 3.0, a similar wake to the baseline case is seen, with a 2S core where there is approximately one 2P pair on each edge for every two 2S vortices in the center. This makes sense, as 2 pairs are generated for every 2 single, and they advect out of the domain at about the same speed. When β = 25.0, on the other hand, the constriction of the active channel outlet significantly reduces the flow velocity around the posterior portion of f_4. This results in significantly more 2S single vortices occurring than 2P pairs. The reduced flow velocity in the channels causes the single vortices in the center of the wake to advect downstream much slower than

the pairs on the edge of the school. Additionally, at about 1.5l downstream from the school, the 2S wake transitions from a BvK wake to a parallel wake [52]. The effect is clear when comparing the cycle-averaged velocity between the cases. The jets coming from the edges of the school, shown previously to correspond with the high thrust production occurring from the wall effect and the 2P pairs it generates, are significantly weakened at β = 25.0 (Fig. 6.16d), owing to the extended near-closing of the active channel leading to reduced velocities in this region. In the flow behind f_4, the space that the 2S wake occupies, the cycle averaged flow velocity is significantly reduced compared to β = 3.0. The reduced velocities confirm that the smaller active channel outlet does hinder flow output from the channels, and has a profound effect on the wake produced by the school.

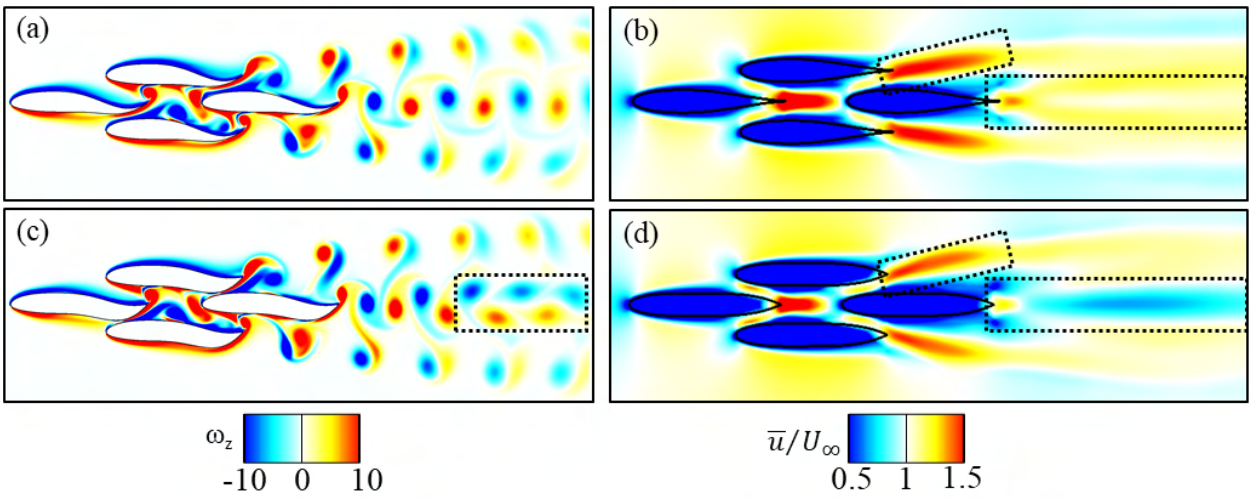

FIGURE 6.16: Vortex wake at t/T = 1.0 and cycle averaged velocity for β = 3.0 and 25.0.

Finally, to quantitatively compare the performance variations along the body, the cycle-averaged net force and undulating power consumption are computed. The results are shown in Fig. 6.17, which displays $\overline{C_x}$ and $\overline{C_{pw}}$ along the body in 10% increments

for f_1, f_2, and f_4, aligned with the undeformed body shapes along the bottom of the figure. The overall higher thrust for smaller boattail angles is observed throughout the posterior half of f_1 and f_2, corresponding with the overall performance trend observed in Fig. 6.5(c). Also seen is an enhanced anterior body suction on f_4 in the larger β cases. This also correlates with the cycle-averaged performance trend for the back fish. It can be attributed to a close proximity of the anterior body to the tail occurring throughout a longer length of tail rather than just the tail tip, allowing for more low-pressure suction on the head. Additionally, the interception of the single vortex V_L^1 shown in Fig. 6.15(c) provides additional low-pressure interaction at the head of f_4.

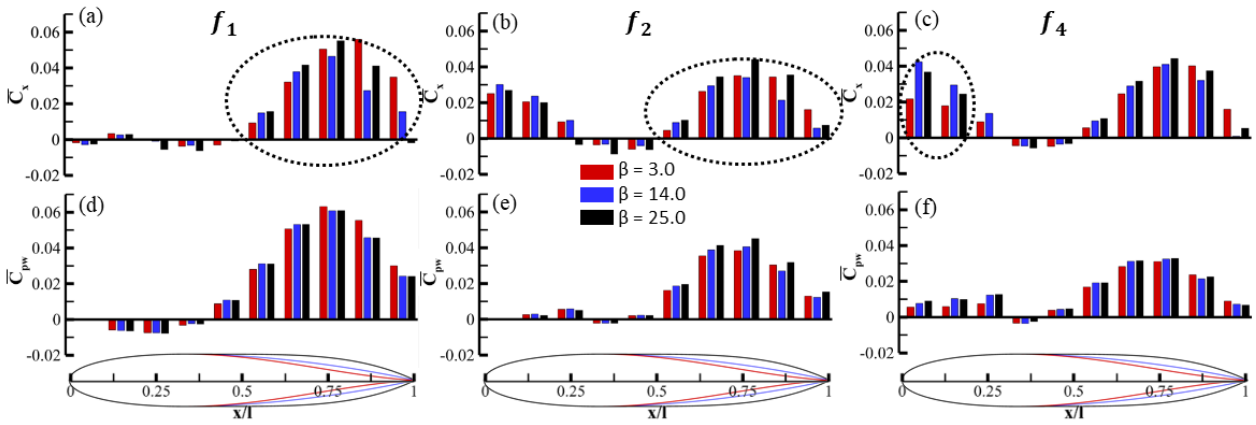

FIGURE 6.17: Cycle averaged net force $\overline{C_x}$(a-c) and power consumed by undulation $\overline{C_{pw}}$(d-f) along each section of the body for S_{max} = 0.20, 0.40, and 0.60. Results are shown for the front fish (a,d), edge fish (b,e), and back fish (c,f).

6.1.5 Section Summary

The effects of body shape on the hydrodynamic performance and interactions in a dense diamond fish school have been numerically studied at a Reynolds number of 1000. The leading edge radius, boattail angle, and maximum thickness location along

the foil are considered. Our results agree with the single fish body shape study of Kelly et al. [71] that the boattail angle has the most dominant effect on performance, followed by maximum thickness location along the foil, and finally the leading edge radius. Changes in the boattail angle show that the thinner boattail angle provides the best performance benefit, particularly for the front and edge fish, in agreement with single fish studies. Variations in maximum thickness location revealed that the closer the maximum thickness is to the head the better, until the point of maximum thickness moves in front of the point along the body that is equivalent to the streamwise position of the tail tip of the neighboring fish, largely due to variation in the wall effect. Leading edge radius changes show that a rounder leading edge provides slightly increased thrust production and undulation power consumption, owing to an increase in low-pressure zone interaction that enhances anterior body suction but also consumes more power. The shape of the active channel, critical in the anterior body suction, wall effect, and vortex-body interaction within the channel, is shown to change by manipulating each of these shape parameters, affecting the interactions between the fish and the performance of the school.

Overall, body shape was found to be an important factor in the hydrodynamics within a 2D fish school, strongly influencing the mechanisms of interaction and performance of the school. The body shape parameters affect the net force generated and the efficiency in the school in a fixed diamond formation. Therefore, we can conclude that in order to reach a more unified view of hydrodynamics in fish schooling, the effects of body shape must be considered. Further, discussions of beneficial hydrodynamic

mechanisms for efficiency should be considered in the context of the body shapes utilized in the study. This knowledge will give better insight when comparing schooling studies, improving our understanding of biological fish schools, and informing the next generation of bio-inspired underwater robotic platforms.

6.2 Body Shape Effects in 3D Fish-like Swimmers

In this section, the study of undulating swimmers of varying body shapes is extended into 3D swimmers. A novel method for fish-like body shape generation based on the CST is developed, allowing for variation in boattail angle, leading-edge radius, maximum thickness, and maximum thickness location along the foil. CT scan data from biological fish are used to establish baseline parameters and testing ranges for solo and staggered swimming simulations. The results reveal that parameters controlling the posterior portion of the body are critical for single-fish performance. Both the top and side profile boattail angles are the most critical factor in determining body drag. In the staggered arrangement, variation in interactions around the narrow channel dictates much of the performance change due to body shape. Because of this, the top profile of the fish is critical to changes in body drag from this schooling interaction.

6.2.1 Problem Statement

6.2.1.1 Class Shape Transformation for 3D Fish Body

To begin the study, a methodology is required for parameterizing fish-like body shapes. For this, a class shape transformation (CST) method is selected. The CST methodology

is shown in previous sections to be a powerful tool for generating a large variety of foil shapes using only a few parameters while maintaining the characteristics of a foil: a rounded leading edge and sharp trailing edge in a continuous curve. In this method, a class function is used to define the basic geometric foil shape. It is then multiplied by the shape function that allows the modification of the basic foil shape and generates a wide variety of geometries. The CST-based foils are generated with the following equations:

$$y(x) = x^{N_1} \cdot (1-x)^{N_2} \cdot \sum_{j=1}^{N} a_j \cdot K_j^N \cdot x^{j-1} \cdot (1-x)^{N-j} = \sum_{j=1}^{N} a_j \cdot B_j^N, \tag{6.4}$$

$$B_j^N = K_j^N \cdot x^{j+N_1-1} \cdot (1-x)^{N+N_2-j} \tag{6.5}$$

$$K_j^N = \frac{(N-1)!}{(j-1)!(N-j)!} \tag{6.6}$$

where $x^{N_1} \cdot (1-x)^{N_2}$ is the class function, $K_j^N \cdot x^{j-1} \cdot (1-x)^{N-j}$ is the shape function, B_j^N are the basis functions, and a_j are the CST coefficients. First, in order to give the general foil shape of a round leading-edge and pointed trailing-edge, we define $N_1 = 0.5$ and $N_2 = 1.0$. Shown in Fig. 6.18(a) are the basis functions for the CST with $N_1 = 0.5$, $N_2 = 1.0$ and $N = 6$. It can be observed that each function corresponds to different locations of peak values along the chord. This particular feature enables the manipulation of thickness in each region. It is made possible by increasing or decreasing the value of a coefficient with the basis function that peaks in the corresponding region. Fig. 6.18(c) illustrates this process through an example, where each coefficient

is increased by about 10% from the NACA0012 value to vary the foil shape. We notice that using larger coefficient values make the resulting foil thicker in the regions where its basis function is the largest. Additionally, the CST-generated NACA0012 foil, the values of which are given in Han et al. [110], is shown alongside the actual NACA0012 foil. This confirms that the CST method accurately portrays this foil shape.

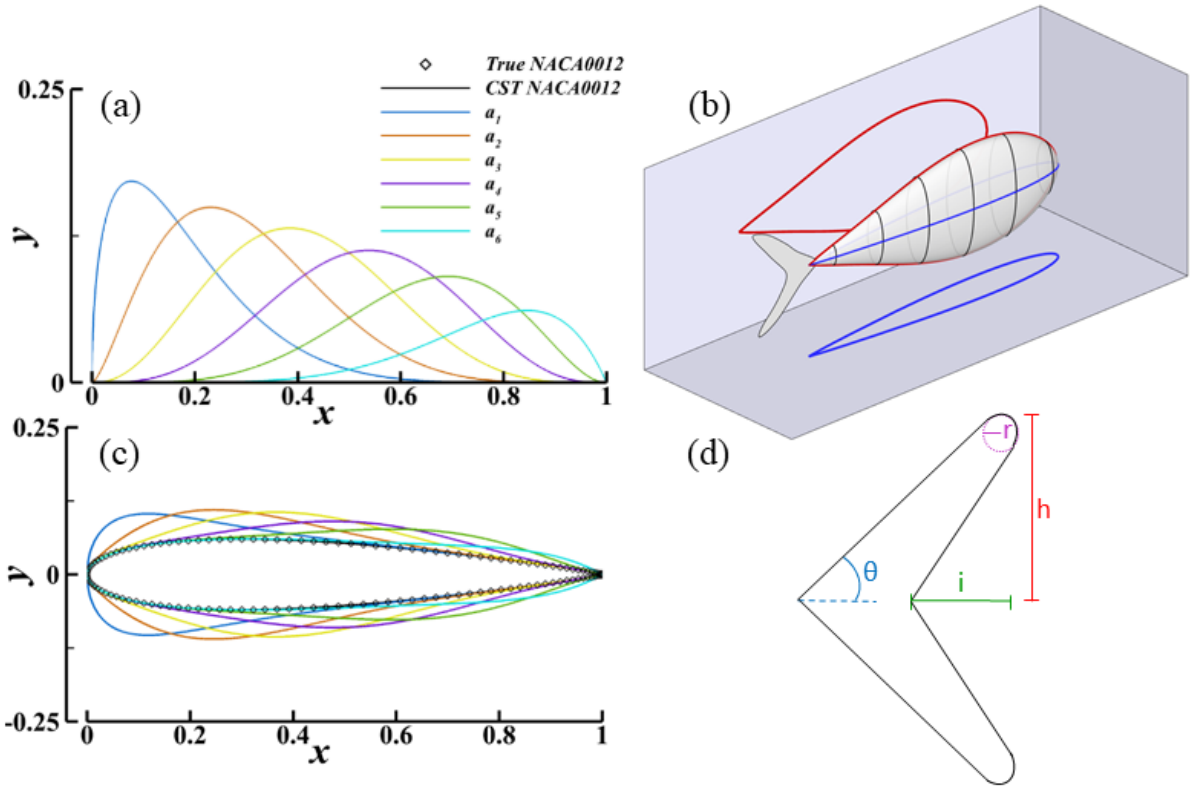

FIGURE 6.18: (a) Basis functions for the CST along the chord and (c) sample foil shapes generated by increasing each parameter individually along with the CST-generated [23] and true [105] NACA0012 Foil. (b) Three-dimensional fish body generated using the CST method. (d) Parametrization of a caudal fin-like tail.

With this method, two-dimensional foil shapes can be made, capable of closely approximating the top (dorsal) or side (lateral) views of biological fish. To create a three-dimensional body, an ellipse is used to connect the two foil shapes. The elliptical equation is defined as $\frac{x^2}{a^2} + \frac{y^2}{b^2} = 1$. To create the fish shape, the body is split lengthwise into 100 segments, where the position along the body for each segment is input into the CST functions for the top and side views to obtain a and b. An ellipse is then generated for the segment. The net result is a fish body where the top and side views are determined by the CST functions and a frontal cut of the body is always an ellipse. This is demonstrated in Fig. 6.18(b), where the top (blue) and side (red) foil shapes are used to define the fish body. In this study, the top and bottom halves of each CST function are kept the same, such that the top and side views of the fish body will always be symmetric.

Finally, to create a realistic fish-like body, a parametrization method is required for the caudal fin. The method for this is demonstrated in Fig. 6.18(d). The upper half of the caudal fin is defined by the leading edge angle (θ), the height (h), the indent (i), and the radius of curvature at the tip (r). In this study, the caudal fin is fixed at a shape based on the jackfish study of Liu et al. [84]. The parameters chosen are provided in Table 6.3 and create the tail shown in Fig. 6.20.

θ	h	i	r
40°	$0.16l$	$0.1l$	$0.005l$

TABLE 6.3: Shape parameters in the jackfish tail used in this study.

6.2.1.2 Biologically Driven Shape Selection

To inform the shape selection in this study, the biological body shapes of carangiform and thunniform schooling swimmers are used. This begins with a search on Morphosource for CT scans of fish bodies. Excluding multiple repeats of the same species, this gave 13 viable body shapes for digitization. An example side view of a bullet tuna (Auxis rochei) is given in Fig. 6.19(a). To reproduce this shape, the outer edge is digitized by selecting 30-40 individual points on each surface (upper and lower). A curve fit is then completed to select CST parameter values to create a matching curve for both the top and bottom profiles from the digitization. To capture some of the more complex peduncle geometries, the number of Bernstein polynomial functions used is increased to N = 12. The two CST parameter value sets are then averaged to create a symmetric foil shape. The resulting CST generated foil shape is shown in Fig. 6.19(a) in blue. With this method, the top and side view of the biological swimmers is converted into CST generated foils.

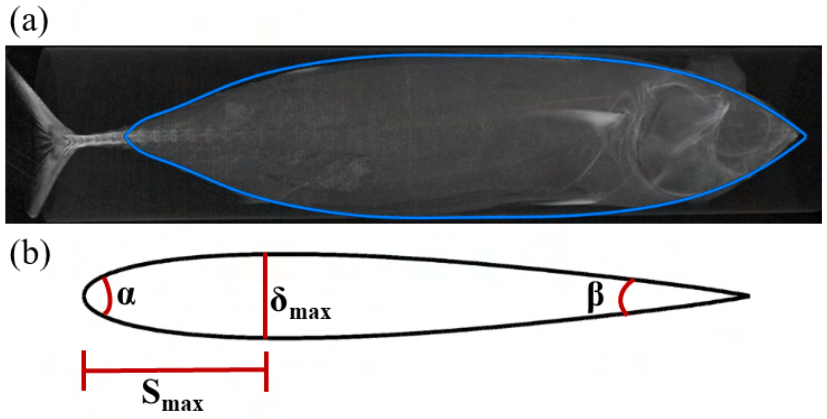

FIGURE 6.19: Side view of a bullet tuna (Auxis rochei) along with the CST reconstructed side profile shown in blue.

To develop an understanding of the body shapes found in nature and to define a range of shapes for this study, fundamental geometric shape parameters are observed for each biological swimmer. These parameters, shown in Fig. 6.19(b) are the leading edge radius (α), boattail angle (β), maximum thickness (δ_{max}), and maximum thickness location (S_{max}). Each of these parameters is given for the top and side views of each fish in Table 6.4.

Fish	View	α	β	δ_{max}	S_{max}
Caranx hippos [127]	Top	39.6	0.00278	0.146	0.222
	Side	36.4	0.0196	0.361	0.404
Oncorhynchus mykiss [128]	Top	53.0	0.00985	0.152	0.407
	Side	67.5	0.00935	0.235	0.347
Danio rerio [129]	Top	44.2	0.0275	0.162	0.332
	Side	65.6	0.00127	0.235	0.430
Auxis rochei [130]	Top	54.9	0.000932	0.174	0.383
	Side	54.9	0.00248	0.229	0.565
Devario anomalus [131]	Top	42.7	0.00682	0.191	0.351
	Side	79.7	0.00186	0.29	0.409
Devario regina [132]	Top	60.9	0.00519	0.156	0.362
	Side	73.5	0.00539	0.286	0.436
Selaroides leptolepis [133]	Top	66.1	0.0146	0.184	0.689
	Side	58.8	0.00490	0.344	0.469
Scomberomorus regalis [134]	Top	50.1	0.000716	0.115	0.258
	Side	66.0	0.0126	0.225	0.388
Hemicaranx bicolor [135]	Top	49.1	0.00557	0.140	0.182
	Side	56.1	0.0251	0.463	0.510
Decapterus macarellus [136]	Top	52.8	0.00345	0.153	0.455
	Side	48.1	0.00207	0.221	0.517
Alepes melanoptera [137]	Top	45.3	0.00302	0.159	0.291
	Side	64.5	0.00365	0.448	0.542
Seriolina nigrofasciata [138]	Top	59.9	0.00907	0.180	0.285
	Side	65.1	0.0118	0.309	0.502
Salmo salar [139]	Top	59.9	0.00907	0.180	0.285
	Side	65.1	0.0118	0.309	0.502

TABLE 6.4: Fundamental shape parameters of biological fish shapes from digitization.

From the biological data, the minimum and maximum of each shape parameter is determined. This range is used for the present study. Additionally, an average of all CST coefficients for the top and side view provides an "average" schooling fish body shape. This shape is shown in Fig. 6.20(a) and is used as the baseline shape for the present study.

6.2.1.3 Arrangement and Body Shapes for Present Study

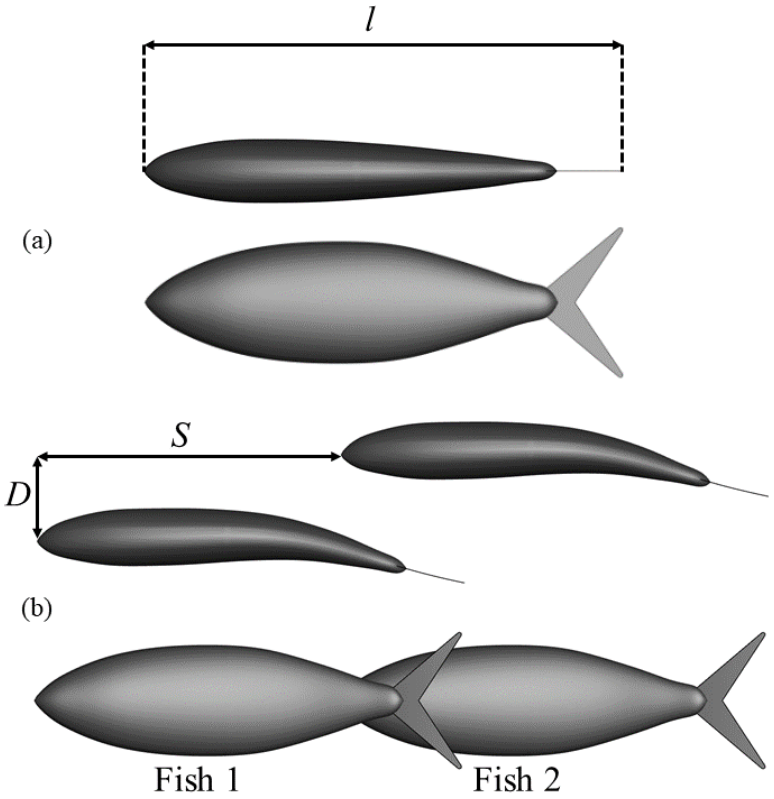

FIGURE 6.20: (a) Top and side view of the baseline shape solo swimmer. (b) Top and side view of the staggered arrangement.

In the present study, the solo and stagger arrangement swimmer is considered. The stagger is arranged as in Fig. 6.20, which shows the baseline fish body (a) and staggered arrangement used in this study. The top and side views of the fish are shown. The body length l is indicated, and the stagger spacing S and D. Fish bodies in the

stagger are labeled for future discussion. The spacing of the stagger is set to mimic the basic 2 fish unit from the diamond studies used previously in this dissertation. This equates to S = 0.7l and D = 0.2l.

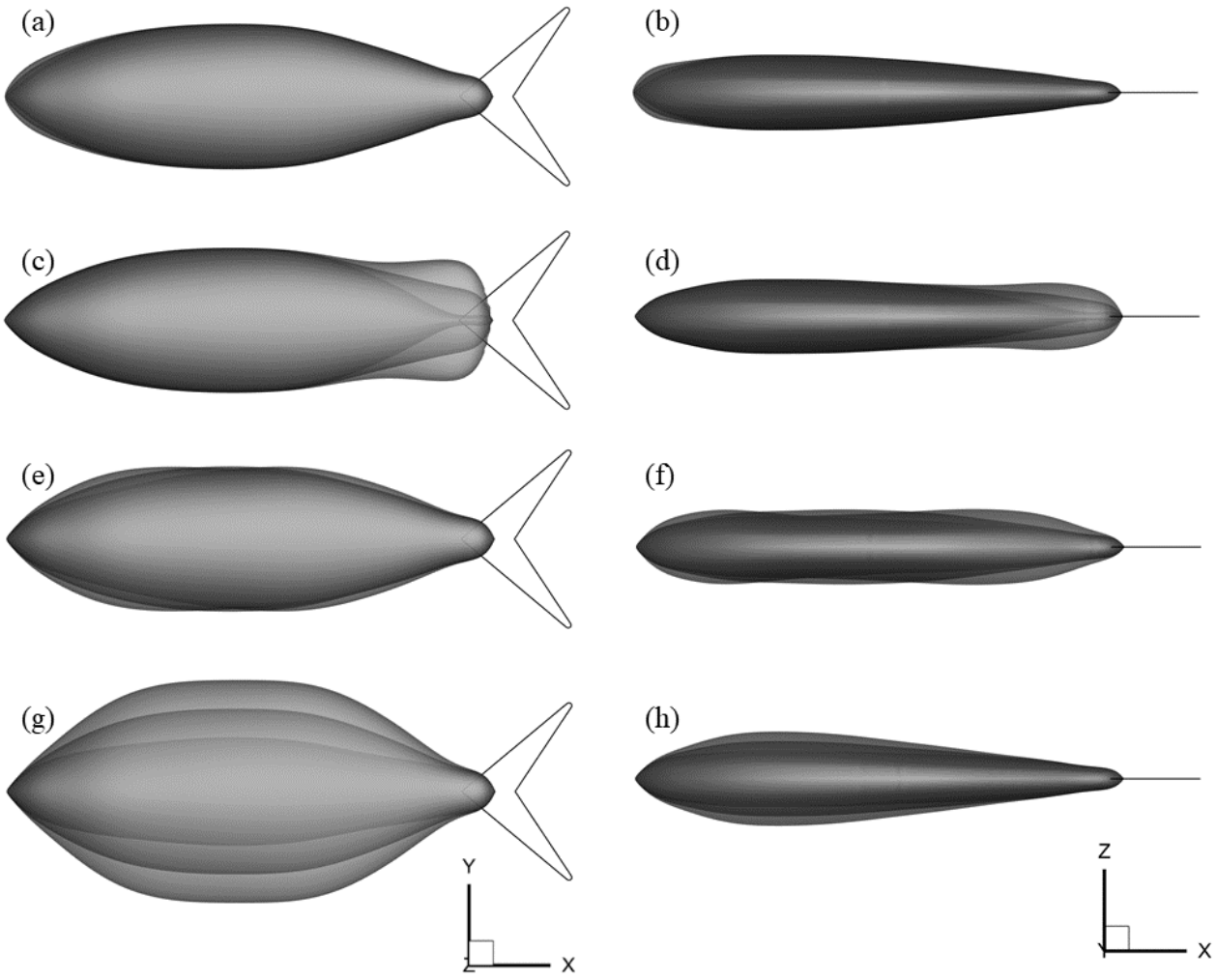

FIGURE 6.21: Body shapes used in this study, changing α (a-b), β (c-d), δ_{max} (e-f), and S_{max} (g-h) of the top (a, c, e, g) and side (b, d, f, h) profiles from the biologically-determined baseline body shape.

The shapes used in this study are defined by the biological shapes shown in section 6.2.1.2. The baseline shape created from averaging each of the biological swimmers is then manipulated by changing the CST coefficients to individually adjust each shape parameter from the top and side views. Each parameter minimum and maximum

is set to the biological minimum and maximum, and three values are evenly spaced in between, creating five total shapes for each of the four shape parameters for both views, creating a total of 40 body shapes. The shapes used are shown in Fig. 6.21. In the figure, three representative shapes from each set of five are shown from the top and side views for changes to the top and side profiles, respectively.

Undulation is prescribed to the body via a traveling wave equation, matching the kinematics discussed in section 6.1.1.2.

6.2.2 Simulation Setup

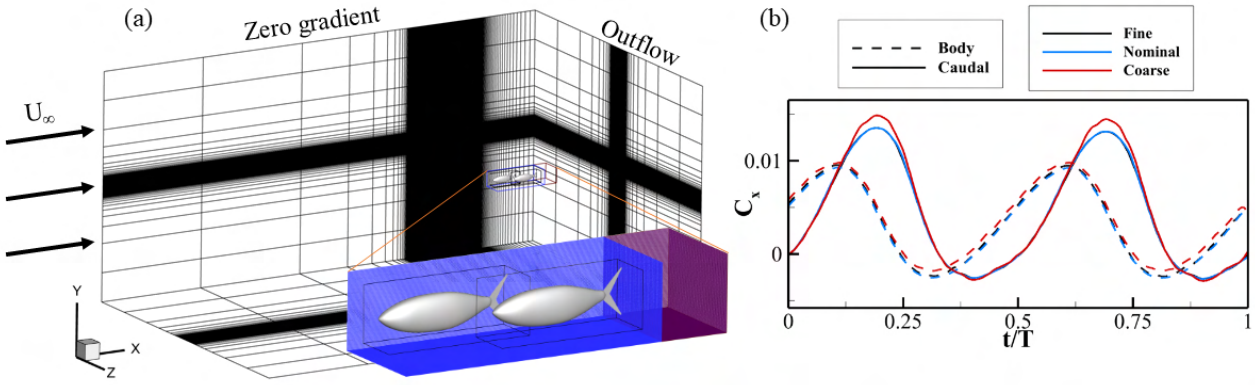

FIGURE 6.22: (a) Schematic of the computational domain, grid, mesh refinement blocks, and boundary conditions. (b) Comparison of the instantaneous forces on the body and caudal fin with a coarse ($\Delta_{min} = 0.004l$), nominal ($\Delta_{min} = 0.003l$), and fine ($\Delta_{min} = 0.0025l$) grid.

A schematic of the non-uniform Cartesian grid and boundary conditions used in this simulation are presented in Fig. 6.22(a). The computational domain size is chosen to be $13l$ x $6l$ x $8l$ with a total grid count of approximately 19 million. The grid spacing around the bodies of the fish is $3.0\text{x}10^{-3}l$. The fish are swimming to the left, with a

constant incoming flow of U_∞ at the left-hand boundary. An outflow boundary condition is assigned to the right-hand side, and each of the top, bottom, front, and back boundaries are set to zero gradient boundary conditions. All boundaries are treated with a homogeneous Neumann boundary condition for pressure. To ensure the accuracy of the grid, a mesh dependence study is shown in Fig. 6.22(b). In the figure, coarse ($\Delta_{min} = 0.004l$), nominal ($\Delta_{min} = 0.003l$), and fine ($\Delta_{min} = 0.0025l$) grid spacings are tested with the baseline body shown in Fig. 6.20. The continuous force and drag coefficients are shown. The difference in peak thrust between the coarse and fine mesh is 9.8% while the difference between the nominal and fine mesh is 0.1%. This demonstrates that results on the nominal grid are grid-independent.

The flow conditions for this study are described using two dimensionless parameters, the Reynolds number (Re) and the Strouhal number (St), given by the following equations:

$$Re = U_\infty l / \nu \tag{6.7}$$

In our current study, we set the Reynolds number to $Re = 5{,}000$. The Strouhal number is defined as

$$St = f A / U_\infty \tag{6.8}$$

It is selected to fulfill a steady swimming condition, where the net force on the body

and caudal fin are made to equal zero when summed over a cycle of motion. For the baseline body shape shown in Fig. 6.20, the steady swimming condition is achieved when $St = 0.56$.

6.2.3 Results and Discussion

6.2.3.1 Baseline Swimmer

An analysis of the baseline body shape swimming in solo and stagger arrangements is completed as a reference for studying the effects of body shape. Fig. 6.23 shows the resulting flow and body forces. In the figure, two rows of vortices (V1-V3) are shed, interconnected by vortex rings (R1-R3). The vortices advect downstream, expanding laterally and compressing in height. This interconnecting vortex ring wake pattern is typical of three-dimensional fish swimming [79], [140]. The body and caudal fin forces over a cycle of motion are provided in Fig. 6.23(c). The thrust and drag demonstrate a typical 2-peaks per cycle of undulation.

The staggered swimming results are shown in Fig. 6.24. In the figure, the flow around the body is visualized from both the top and side views. From this, the primary wake interactions are indicated in the figure. First, the vortex shed from the previous half cycle of flapping motion from fish 1 impacts the body of fish 2. The same vortex travels down the body of fish 2 through the motion, and a cycle later it is seen in part (b) as it is intercepted by the caudal fin. This interception has been noted in previous studies of staggered swimming and can be beneficial or detrimental to the caudal fin thrust

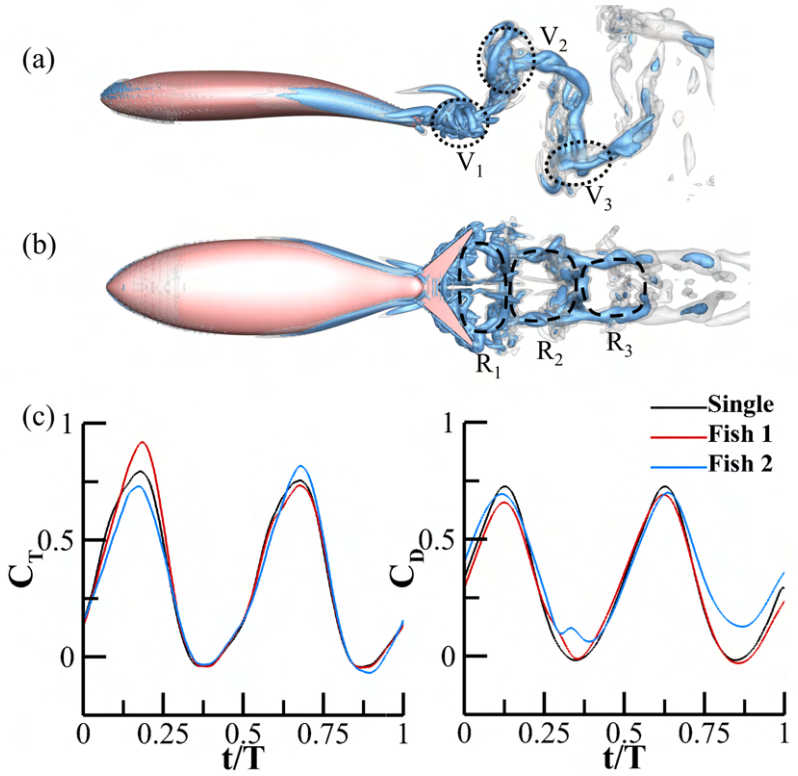

FIGURE 6.23: Top (a) and side (b) views of flow visualized by isosurfaces of the Q criterion at Q = 10 and 50 for the baseline body shape at t/T = 1.0. Key vortices are indicated. (c) Body and caudal forces for the solo and staggered swimmers at the baseline shape.

production based on the distance between swimmers, phase, and incoming flow speed [22].

The continuous coefficients of thrust and drag are shown alongside the solo swimmer in Fig. 6.23(c). In it, the impact of the caudal fin vortex interaction is seen around t/T = 0.1 to 0.25 in fish 2, causing a lower thrust. The thrust of fish 1 is also improved around this time window. To investigate the differences for fish 1 further, isosurfaces of the pressure are plotted in Fig. 6.24(d) at t/T = 0.30. In the figure, the channel between the two fish is closing to a minimum, and the presence of fish 2 has enhanced the high-pressure buildup around the posterior and caudal fin of fish 1. This enhanced pressure

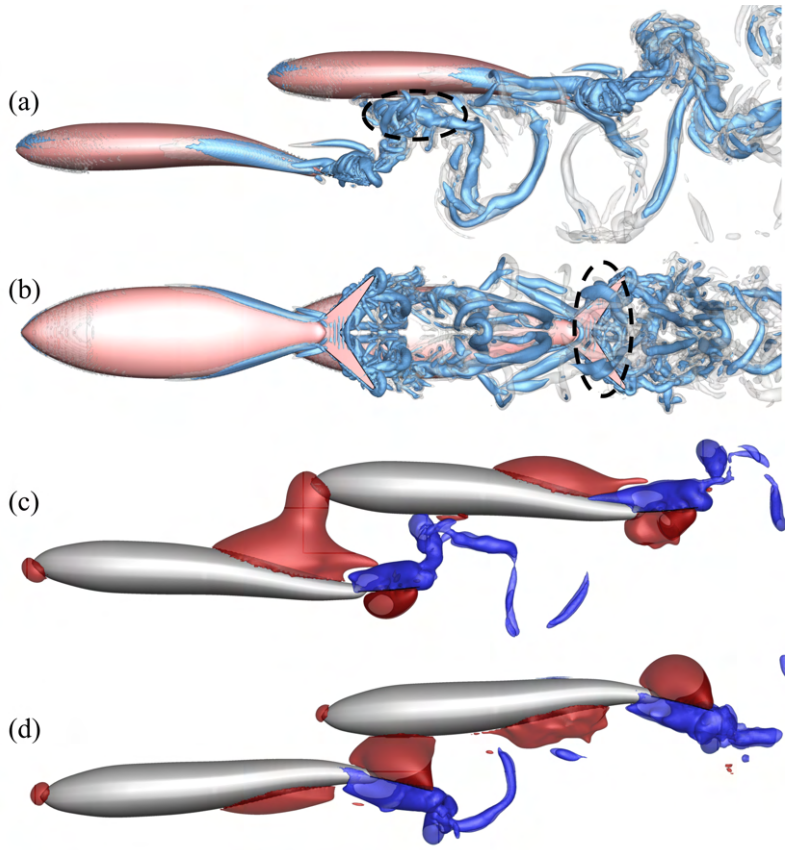

FIGURE 6.24: Top (a) and side (b) views of flow visualized by isosurfaces of the Q criterion at Q = 10 and 50 for the baseline body shape in the staggered arrangement at t/T = 1.0. Key vortices are indicated. (c) Pressure isosurfaces at t/T = 0.82 (c) and 0.30 (d), with the positive pressure (P=0.03) colored red and the negative pressure (P=0.05) colored blue.

and more provides an increase in the caudal fin thrust generation for fish 1 at the cost of increasing the body drag of fish 2. The impacts to the body drag are even greater than the caudal fin. The body drag of fish 2 is increased by an interaction with the same high-pressure region that enhances the caudal fin pressure on fish 1. Additionally, as the head of fish 2 is closest to the body of fish 1, the high pressure generated along the body of fish 1 from the undulation motion impacts the head of fish 2. This significantly increases body drag in fish 2 from t/T = 0.7 to t/T = 1.0. This pressure interaction is shown in the pressure isosurfaces of Fig. 6.24(c).

6.2.3.2 Varying body shape results

Solo Swimmer

The results of the solo swimmer undulating for each body shape are compared to the baseline shape. The results are presented in Fig. 6.25. In the figure, each parameter is varied based on the biological swimmer range as demonstrated in Fig. 6.21. The results are shown in plots where the x-axis represents the shape parameter range in the study and the y-axis represents the percentage change compared to the baseline shape solo swimmer. Note that to see the effects for each shape, the axis limits of the percentage change are scaled for each shape change individually.

In the figure, it is immediately apparent that the body shape has the lowest overall impact on the thrust performance of the caudal fin. The largest change is within 1% of the baseline value. The least significant parameters are the leading edge radius from both the top and side profiles. They both provide no performance changes greater than 1%. Similarly, the maximum thickness location of the side profile has no performance changes greater than a few percent, at the greatest values. The maximum thickness location of the top profile does show a significant body drag increase as the maximum thickness of the profile moves into the later half of the body. The boattail angle shows large performance changes of almost 100% total range in both the side and top profiles, with the lower body drag resulting from a large side profile boattail angle and a small top profile boattail angle. Increasing the maximum thickness of each profile corresponds with an increase in the body drag for both body profiles. This is consistent

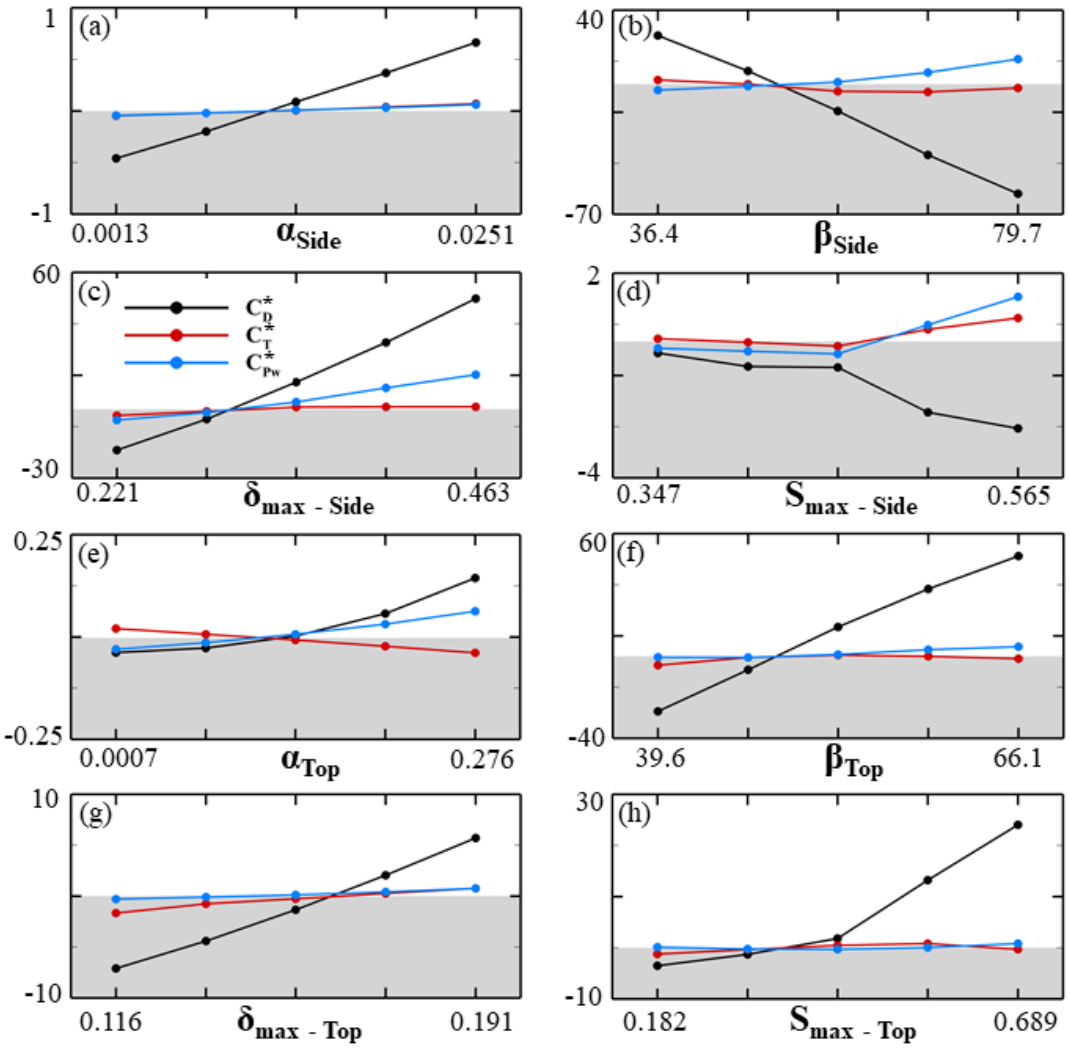

FIGURE 6.25: Solo swimmer percent change in body drag, caudal thrust, and total power consumption for each body shape compared to the baseline shape.

with the Tunabot body shape results presented previously.

Figure 6.26 shows the pressure isosurfaces for solo swimming of the smallest and largest side profile boattail angle fish models. The tall peduncle region of the $\beta = 79.7$ body shape provides a surface area that acts as an extension of the tail. In this time instance, the body undulation creates significant low-pressure suction on the tail to generate thrust. Due to the position of the body from undulation, low pressure on

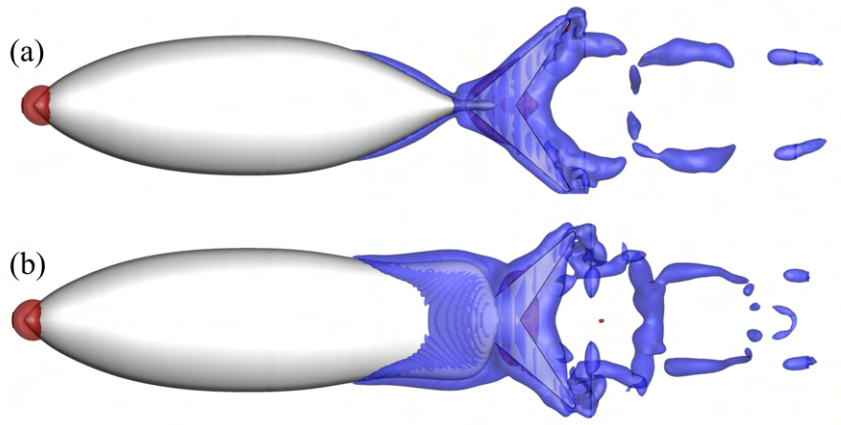

FIGURE 6.26: Pressure isosurfaces for side $\beta = 36.4$ (a) and $\beta = 79.7$ (b) at t/T = 0.08.

the posterior body surface at this timestep provides significant thrust to the body. The taller body also helps to prevent the flow from each side of the posterior region from mixing, allowing separate negative and positive pressure regions to form. Using median fins, similar results have been found [84], [85], including the median fin study in this dissertation. In this instance, the tall body acts as a pseudo-median fin in its function. Because of this, the body produces less than a third of the drag from the baseline body shape.

Figure 6.27 presents the vorticity, pressure isosurface, and surface pressure on the body for the small and large top profile boattail angle. In the vorticity, better flow attachment to the body around the peduncle is seen for the smaller boattail angle. This corresponds with a more cohesive wake and stronger high and low-pressure attachment around the peduncle region of the body. The angle of the body allows these pressure regions to alleviate some of the drag suffered by the body. The smaller boattail angle also increases this by providing a surface normal and more in line with the forward direction. The

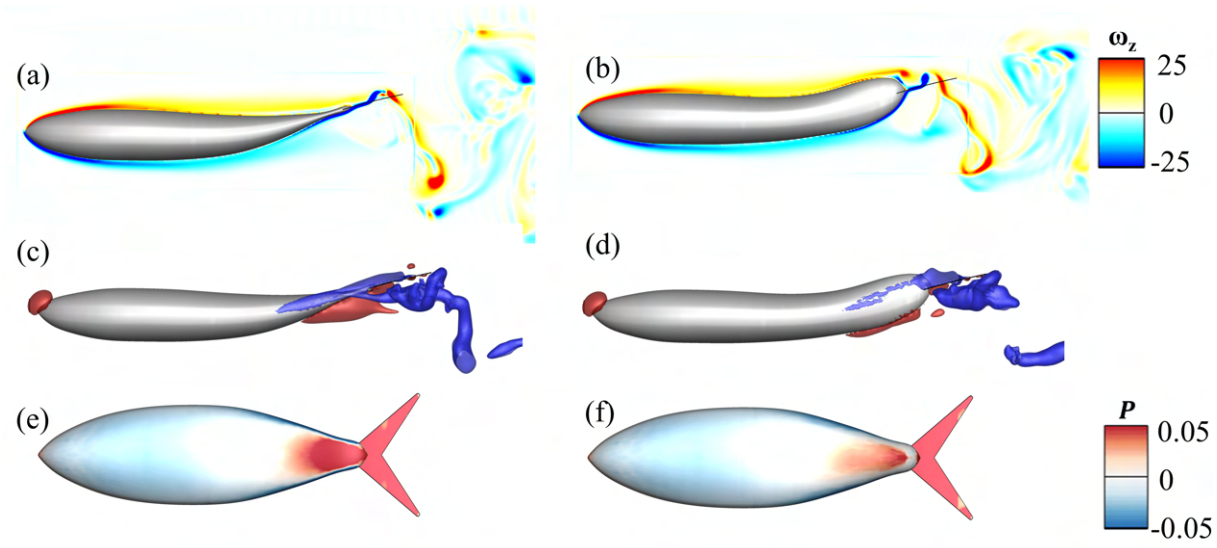

FIGURE 6.27: Vorticity (a,b), pressure isosurfaces (c,d) and body surface pressure (e,f) for top $\beta = 39.6$ (a, c, e) and $\beta = 66.1$ (b, d, f) at t/T = 0.50.

increased pressure on the lower surface of the body is best demonstrated in Fig. 6.27(e-f), where the posterior body region has clear increased pressure in the posterior region contributing to the reduction in drag.

Staggered Swimmers

The results of the staggered swimmers undulating for each body shape are compared to the baseline shape in Fig. 6.28. In the figure, each parameter is varied based on the biological swimmer range as demonstrated in Fig. 6.21. The results are shown in plots where the x-axis represents the shape parameter range in the study and the y-axis represents the percentage change compared to the same fish in the staggered baseline, i.e. the fish 1 results are a percentage comparison to fish 1 of the baseline staggered case, and the fish 2 results are a percentage comparison to the fish 2 results of the baseline staggered case. Note that to see the effects for each shape, the axis limits of the percentage change are scaled for each shape change individually.

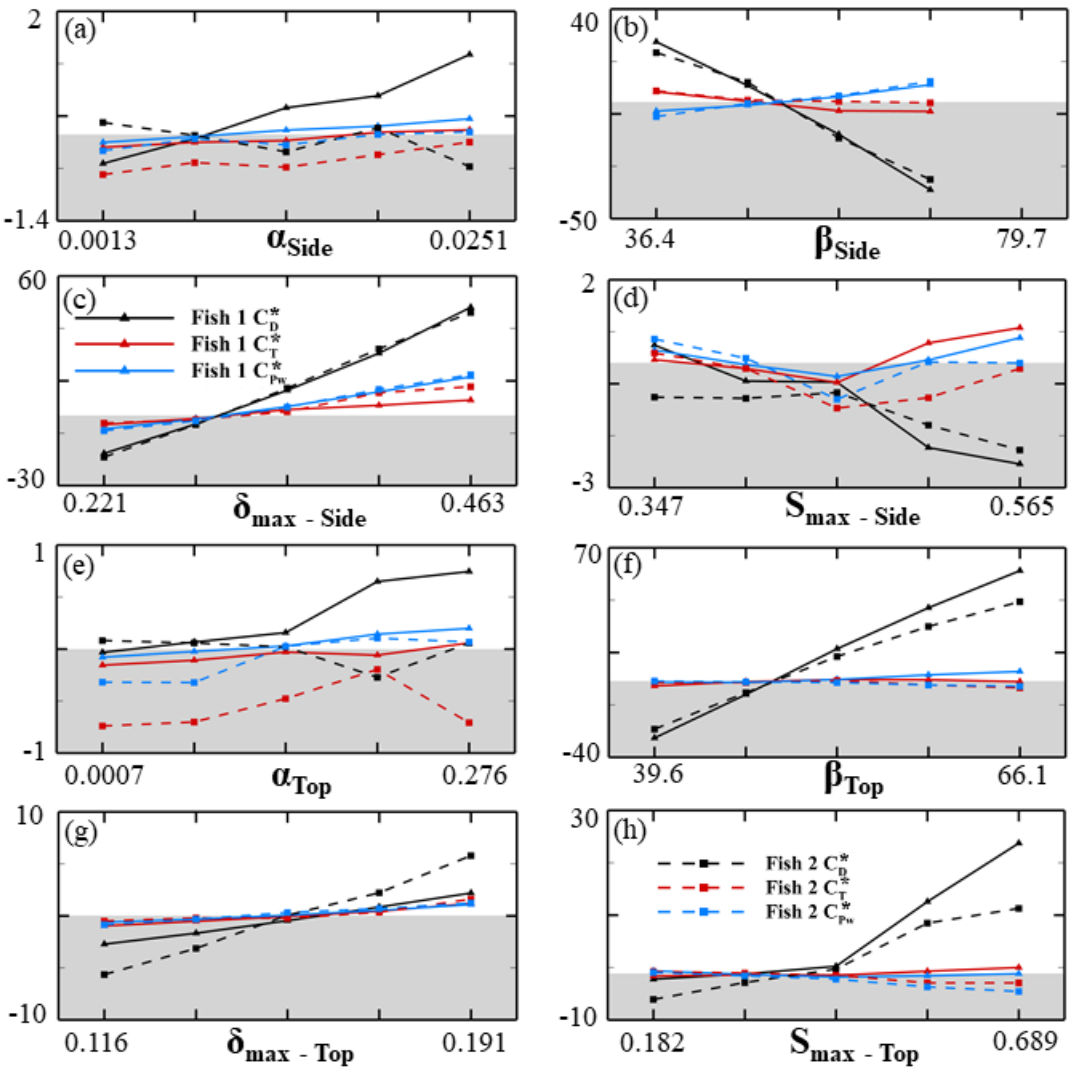

FIGURE 6.28: Percent change in body drag, caudal thrust, and total power consumption for each body shape compared to the baseline shape for each fish in the staggered formation.

From the ranges of performance occupied by each parameter for the figure, a few things are immediately apparent. Once again, the leading-edge radius of the top profile, maximum thickness of the side profile, and leading-edge radius of the side profile had a very small impact on the total performance. Furthermore, the remaining side profile parameters, boattail angle, and maximum thickness have two identical lines that match the single fish data in Fig. 6.25. This suggests that while body shape

changes do impact their performance, there is no additional change from the schooling interaction. In the remaining parameters, the top profile maximum thickness sees a reduced effect in Fish 1 - both the body drag improvement at the thinner body and the body drag detriment at the thicker body are dampened for fish 1. The top profile of the boattail angle has an increased effect in fish 1, particularly in the drag increase of the thicker boattail angle values. Finally, the top profile location of maximum thickness drag increase at high S_{max} values is dampened significantly in fish 2.

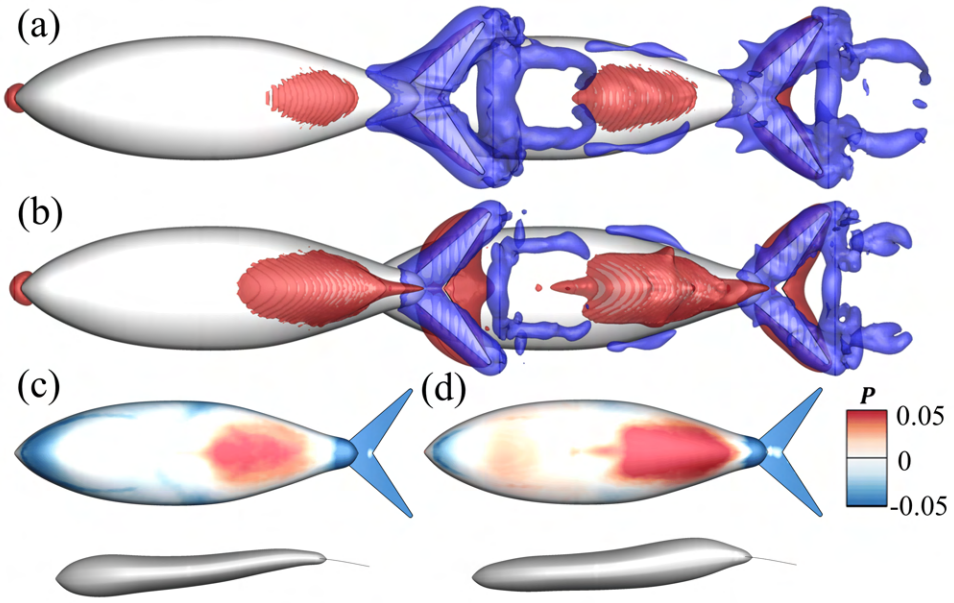

FIGURE 6.29: Pressure isosurfaces (a-b) and fish 2 surface pressure (c-d) for $S_{max} = 0.182$ (a,c) and $S_{max} = 0.689$ (b,d) at t/T = 0.30. Body shape and position are shown at the bottom of the figure.

Figure 6.29 shows pressure isosurfaces and fish 2 body surface pressure for the top profile $S_{max} = 0.182$ and $S_{max} = 0.689$. In the figure, the pressure enhancement on the posterior surface of fish 2, shown in the baseline body shape in Fig. 6.24(d), is occurring for each case. The high-pressure region is much greater around the bottom posterior portion of fish 2 in the case of $S_{max} = 0.689$. This results in a higher pressure on the

surface of the fish, visible in part (d). In addition to these, the body at this position has a normal pointing more downstream due to the maximum thickness location shift. This results in some forward force that alleviates body drag occurring in the $S_{max} = 0.689$ due to the interaction that is not present for a maximum thickness closer to the head. This reduction in drag alleviates some of the body drag detriment of a large S_{max}, as shown in Fig. 6.28.

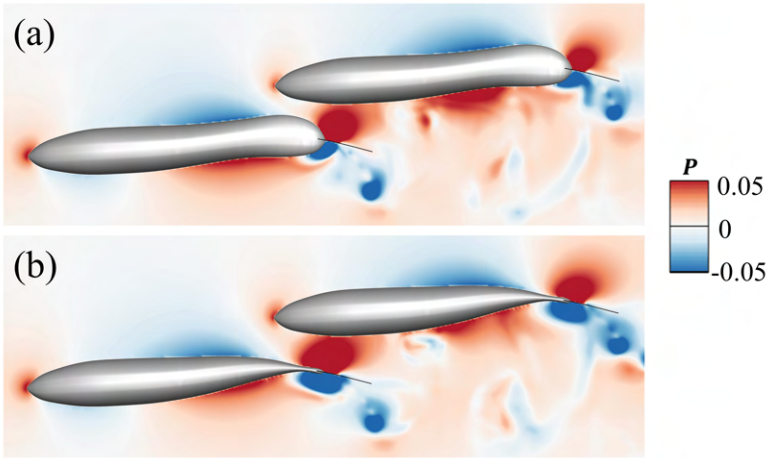

FIGURE 6.30: Pressure slice cuts through the mid-body plane for top profile $\beta = 66.1$ (a) and $\beta = 39.6$.

Figure 6.30 presents a slice cut of the pressure through the mid-plane of the body for top profile $\beta = 39.6$ and $\beta = 66.1$ at t/T = 0.30. The figure shows the time instance where the channel between bodies is constricted the most, and the baseline body shape case demonstrated a decrease in the drag of fish 1 due to a positive pressure region constructive interaction within the narrow channel (Fig. 6.24). The solo swimmer increase of the top profile boattail angle saw less attachment in this same positive pressure region to the body as it moves along the peduncle. In the stagger case, the peduncle region of the larger boattail angle case fails to take advantage of the stagger formation

benefit for a long due to the detaching of this high-pressure region from the peduncle. The region is not significantly captured by the caudal fin due to its concentration near the mid-plane and the gap in the midpoint of the caudal fin. This effect is seen in Fig. 6.30 where the positive pressure region in the channel between fish is weaker and less attached to the body of fish 1 in part (a) compared with part (b).

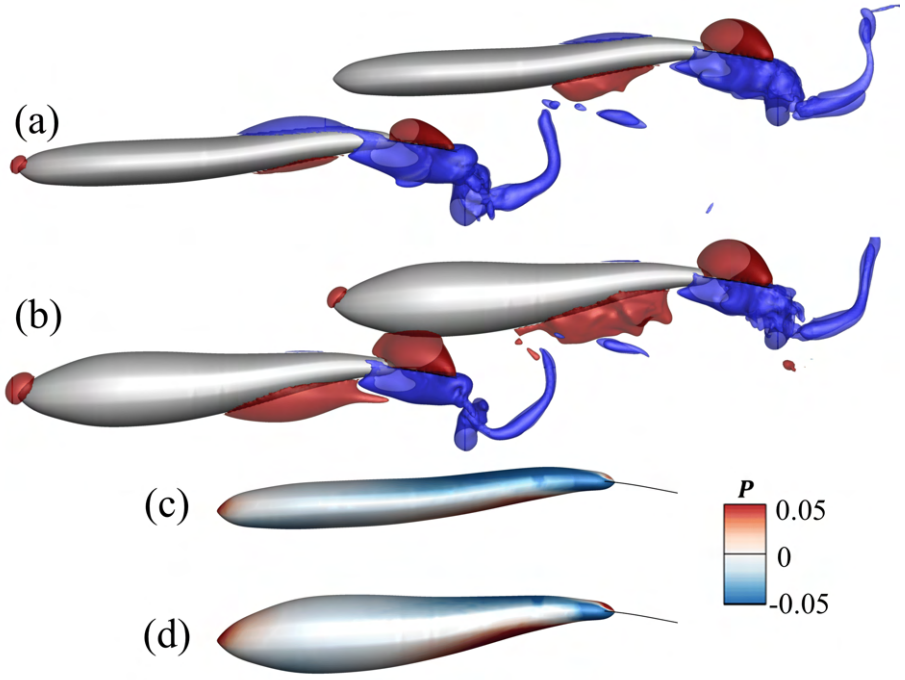

FIGURE 6.31: Pressure isosurfaces (a-b) and fish 1 surface pressure (c-d) for $\delta_{max} = 0.116$ and $\delta_{max} = 0.191$ at t/T = 0.30.

Finally, Figure 6.31 shows pressure isosurfaces and the body surface pressure of fish 1 for $\delta_{max} = 0.116$ and 0.191 at t/T = 0.30. In the thinner body, the positive pressure enhancement that occurs across the channel between the fish bodies does not occur. The smaller body creates weaker high-pressure zones, and fish 1's caudal fin proximity to the body of fish 2 is lessened by the body thickness change. The combination of these results in no enhancement, evident in the body surface pressure. In the thicker fish body, the last 5% of the body length has some positive pressure on the top, reducing

some of the total body drag. The thin body, however, does not have this effect, and the body drag does not benefit. This enhanced high pressure from the closer caudal fin proximity also results in a slight increase of 2.5% in the thrust production from the caudal fin not seen in the solo swimmer.

6.2.4 Section Summary

In this section, the effects of body shape on fish-like undulating swimmers are studied numerically. A novel body shape generation method based on a class shape transformation of the top and side profiles of the body is used to generate body shapes to enable a variety of body shapes and control fundamental shape parameters. Digitization and reconstruction of biological fish body shapes are completed to establish a baseline for this study and establish a range of parameters to be tested. Our results find that body shape has the largest impact on drag, and altering body shape can provide body drag reduction, including further reduction via schooling interactions. Changes to the side profile of the fish had very little impact on the stagger interactions, but it did significantly change the solo swimmer performance. The side profile boattail angle, determining the height of the fish near the peduncle region, offers thrust-producing mechanisms by acting as an extension of the caudal fin, relieving much of the total drag production on the body. The boattail angle of the top view, in agreement with the two-dimensional results, is a significant variable in both solo and stagger swimming, offering better performance and enhancing interaction benefits when the angle is smaller. Consistent with the diamond school results in two-dimensional swimming,

most of the stagger performance changes due to body shape occur at the narrow channels between the fish. The maximum thickness and maximum thickness location along the body alter the shape of the channel and the ability to benefit from body-body interactions across it.

7 Conclusions

The work presented in this dissertation has investigated the hydrodynamic performance and flow dynamics in two and three-dimensional fish schools, with a focus on the impacts of morphology and large school effects. The study uses undulating fish models and bioinspired robotic fish models in high-fidelity numerical simulations. The studies identify key hydrodynamic mechanisms for performance enhancement, offering insight into the biological understanding of fish swimming and schooling and informing the next generation of fish-like robotic platforms.

7.1 Summary of Contributions

In Chapter 3, canonical models of planar fish schools are studied. It is found that wide schools provide the most power savings, long schools provide the most thrust enhancement, and diamond schools balance the two for the most efficiency benefit. All large school formations, however, significantly improve on the efficiency compared to a solo or diamond school swimmer. Furthermore, the diamond school offers balanced benefits, where all fish in the school gain from the interactions, whereas the other arrangements are more predatory, where some fish suffer for others to gain significantly.

The wall, block, and anterior body suction from the larger schools of Kelly et al. [15] continue to take place, allowing similar classification to previous studies. As the school grows much larger, body-body pressure interactions are found to be the driving force of performance change as the school and the synchrony of the school align all the high and low-pressure regions to the same sides of the fish. This issue is not solved by moving to arrangements in varying phases, however, as any phase lag introduced only decreases the efficiency of the school.

In Chapter 4, canonical models are used to study the hydrodynamic interactions in dense subgroups. The addition of the second subgroup is found to be beneficial both for the force production in the front group and the efficiency in the back group. Simulations reveal constructive interaction with the wake in the back subgroup allowing enhanced performance and is dependent on the spacing between the groups. Capturing the wider lateral wake allows for similar efficiency benefits in the back subgroup to swimming densely, but the net force does drop as the dense interactions are dampened. In the second subgroup, interacting with the wake of a fish school is found to offer many regions of potential benefit, with the note that there is a possibility for a decrease in performance via subschooling as well.

In Chapter 5, morphology in a robotic tuna-like platform is studied. A flapping foil models is used to study the propulsor, observing the effects of cross-sectional propulsor shape. The results find that a thicker leading edge on the foil leads to more favorable pressure gradients, but too thick leads to a lack of adhesion of the leading edge vortex and a premature body vortex separation. With the full reconstructed model of

the Tunabot, the body flexibility is found to reduce the caudal fin power consumption and increase efficiency. Increasing the body thickness does increase body drag, but the amount is minor until a critical point where the thickness is 23% of the body length. The changes in body flexion reveal that some body joints can be reduced while improving system efficiency. Finally, the addition of rigid median fin is found to provide significant thrust and efficiency benefits to the system, and a smaller fin band in the posterior region helps to alleviate body drag.

In Chapter 6, canonical models of varying shapes are undulated in 2D and 3D to understand the impact that fish shape has on schooling interactions. A diamond formation is used in the 2D study, finding body shape to be a significant factor for both solo swimming and schooling. A study of the mechanisms reveals how the body shape alters the previously known wall, block, and anterior body suction effects as well as wake interception that occurs within a diamond school. Expanding on these results, a three-dimensional fish body shape construction method is developed. This method facilitates a parametric study of body shapes, which shows an even larger impact of the morphology on performance in three dimensions due to the higher body drag. The top profile is most important for altering schooling interactions, and the posterior region of the body is found to have the most significant impact on the performance of solo and schooling swimmers.

7.2 Future Work

The work presented in this dissertation advances knowledge of fish-like swimmer hydrodynamics. However, some limitations to the study are present and offer many opportunities for future study.

One significant limitation in this dissertation that can be extended into future work is the free swimming models of fish schools. The current work relies on prescribed schooling arrangements with fish occupying fixed positions in space, despite unbalanced forces occurring on the bodies of individual fish within the school. Understanding how the dynamics of a school are impacted by these forces is critical to future understanding of fish schools, however, the technical and practical limitations of these models have led to little use overall in studies of fundamental hydrodynamics of fish schooling. By studying these free swimming effects, some of the parameters that are found in nature to not be the most beneficial for efficiency or thrust in prescribed arrangement simulations may be found to better stabilize a fish position within a school. Furthermore, methods for stabilizing fish into optimal formations found in these prescribed arrangement studies are a critical step towards taking advantage of optimal physics in bio-inspired robotic applications.

The subschooling interactions have many avenues of future study, including the interaction between large schools, non-diamond formations, and differing sizes of each subgroup. At the arrangement in this study, a selection is required to either have a

sparser back subgroup to capture the edges of the wake or maintain a denser formation to take advantage of maximum dense schooling interaction benefits. By increasing the size of each subsequent school, this shortcoming can be avoided, and provides an interesting direction for future study.

The investigations into the large fish schools should be expanded to use predictive scaling laws as school size continues to grow. Conclusive trends using scaling laws can more definitively inform placement of additional fish in a school depending on the more important performance metrics. Also, these scaling laws can provide a simple tool for estimating large school performance with more consideration for hydrodynamic interactions than dipole methods.

Additionally, this study presents a framework for understanding the effect that body shape has in carangiform-like undulating with a single tail shape. Chapter 6 outlines an effective methodology for generating body and tail shapes for study, and research that focuses on the impact of the tail may better explain some of the wide range of body shapes seen in solo swimmers and schooling fish in nature. Many extensions of this study can be pursued, including extending beyond carangiform motion, asymmetrical fish body shapes, the use of median fins in place of body thickness increases, and the combination of parameter changes occurring simultaneously. Finally, the use of body shape to enable maneuverability, rather than speed or efficiency, should be investigated to garner a more complete understanding of body shape effects in fish swimming.

Bibliography

[1] V Brock and R Riffenburgh, "Fish schooling: A possible factor in reducing predation," *ICES Journal of Marine Science*, vol. 25, pp. 307–317, 1960.

[2] J Cech and P Moyle, "Fishes: An introduction to ichthyology," *Pearson/B. Cummings*, 2004.

[3] T Pitcher, "Functions of shoaling behaviour in teleosts, in: The behaviour of teleost fishes," *Springer*, pp. 294–337, 1986.

[4] E Shaw, "Schooling fishes: The school, a truly egalitarian form of organization in which all members of the group are alike in influence, offers substantial benefits to its participants," *American Scientist*, vol. 66, pp. 166–175, 1978.

[5] C White, "Tuna-inspired experimental platforms exploring high-performance fish swimming," *Dissertation*, 2022.

[6] F Berlinger, M Gauci, and R Nagpal, "Implicit coordination for 3d underwater collective behaviors in a fish-inspired robot swarm," *Science Robotics*, vol. 6, 2021.

[7] S Berg, R Sharff, Z Rusak, and J Wu, "Openfish: Biomimetic design of a soft robotic fish for high speed locomotion," *HardwareX*, vol. 12, 2022.

[8] F Fish and G Lauder, "Passive and active flow control by swimming fishes and mammals," *Annual Review of Fluid Mechanics*, vol. 38, no. 1, pp. 193–224, 2005.

[9] F. Gibouin, C. Raufaste, Y. Bouret, and M. Argentina, "Study of the thrust-drag balance with a swimming robotic fish," *Physics of Fluids*, vol. 30, no. 9, 2018.

[10] C. H. White, G. V. Lauder, and H. Bart-Smith, "Tunabot flex: A tuna-inspired robot with body flexibility improves high-performance swimming," *Bioinspiration and Biomimetics*, vol. 16, 2 Mar. 2021.

[11] M. Narasimhan, H. Dong, R. Mittal, and S. N. Singh, "Optimal yaw regulation and trajectory control of biorobotic AUV using mechanical fins based on CFD parametrization," *Journal of Fluids Engineering, Transactions of the ASME*, vol. 128, no. 4, pp. 687–698, 2006.

[12] G. V. Lauder, P. Madden, I. Hunter, *et al.*, "Design and performance of a fish fin-like propulsor for AUVs," *Proceedings of 14th International Symposium on Unmanned Untethered Submersible Technology (UUST)*, pp. 1–13, 2005.

[13] *Courtesy of the lauder lab*.

[14] *Courtesy of nature picture library*.

[15] J. Kelly, Y. Pan, A. Menzer, and H. Dong, "Hydrodynamics of body–body interactions in dense synchronous elongated fish schools," *Physics of Fluids*, vol. 35, no. 041906, 2023.

[16] B. Muller, V. D. Heuvel, E Stamhuis, and J Videler, "Fish foot prints: Morphology and energetics of the wake behind a continuously swimming mullet (chelon labrosus risso)," *Journal of Exeperimental Biology*, vol. 200, pp. 2893–2906, 1997.

[17] H Liu and K Kawachi, "A numerical study of undulatory swimming," *Journal of Computational Physics*, vol. 155, pp. 223–247, 1999.

[18] G Lauder, "Function of the caudal fin during locomotion in fishes: Kinematics, flow visualization, and evolutionary patterns," *American Zoologist*, vol. 40, pp. 101–122, 2000.

[19] J Birch and M Dickinson, "Spanwise flow and the attachment of the leading-edge vortex on insect wings," *Nature*, vol. 412, no. 729, 2001.

[20] C Ellington, C. V. D. Berg, A Willmott, and A Thomas, "Leading-edge vortices in insect flight," *Nature*, vol. 384, no. 626, 1996.

[21] I Borazjani and M Daghooghi, "Leading-edge vortices in insect flight," *Proceedings of Royal Society B*, vol. 280, no. 20122071, 2013.

[22] J Seo and R Mittal, "Improved swimming performance in schooling via leading-edge vortex enhancement," *Bioinspiration and Biomimetics*, vol. 17, no. 066020, 2022.

[23] Y. Pan and H. Dong, "Computational analysis of hydrodynamic interactions in a high-density fish school," *Physics of Fluids*, vol. 32, no. 12, 2020.

[24] U Muller and J van Leeuwen, "Undulatory fish swimming: From muscles to flow," *Fish and Fisheries*, vol. 7, pp. 84–103, 2006.

[25] D. Pavlov and A. Kasumyan, "Patterns and mechanisms of schooling behavior in fish: A review," *Journal of Ichthyology*, vol. 40, no. 2, pp. 163–231, 2000.

[26] D. Weihs, "Hydromechanics of fish schooling," *Nature*, vol. 241, pp. 290–291, 1973.

[27] Y Zhang and G Lauder, "Energy conservation by collective movement in schooling fish," *eLife*, vol. 12, no. RP90352, 2023.

[28] J Johansen, R Vaknin, J Steffensen, and P Domenici, "Kinematics and energetic benefits of schooling in the labriform fish, striped surfperch embiotoca lateralis," *Marine Ecology Progress Series*, vol. 420, pp. 221–229, 2010.

[29] J. Herskin and J. F. Steffensen, "Energy savings in sea bass swimming in a school: Measurements of tail beat frequency and oxygen consumption at different swimming speeds," *Journal of Fish Biology*, vol. 53, no. 2, pp. 366–376, 1998.

[30] S. S. Killen, S. Marras, J. F. Steffensen, and D. J. Mckenzie, "Aerobic capacity influences the spatial position of individuals within fish schools," *Proceedings of the Royal Society B: Biological Sciences*, vol. 279, no. 1727, pp. 357–364, 2012.

[31] H. Kim and D. Kim, "Stability and coupled dynamics of three-dimensional dual inverted flags," *Journal of Fluids and Structures*, vol. 84, pp. 18–35, 2019.

[32] D. Deb, P. Shetty, K. Poddar, and S. Kumar, "Flow induced oscillation of two rigid rectangular plates in a side-by-side configuration," *Journal of Fluids and Structures*, vol. 99, p. 103 133, 2020.

[33] T. M. Broering, Y. Lian, and W. Henshaw, "Numerical investigation of energy extraction in a tandem flapping wing configuration," *AIAA Journal*, vol. 50, no. 11, pp. 2295–2307, 2012.

[34] L. E. Muscutt, G. D. Weymouth, and B. Ganapathisubramani, "Performance augmentation mechanism of in-line tandem flapping foils," *Journal of Fluid Mechanics*, vol. 827, pp. 484–505, 2017.

[35] I. Akhtar, R. Mittal, G. V. Lauder, and E. Drucker, "Hydrodynamics of a biologically inspired tandem flapping foil configuration," *Theoretical and Computational Fluid Dynamics*, vol. 21, no. 3, pp. 155–170, 2007.

[36] L. Cong, B. Teng, and L. Cheng, "Hydrodynamic behavior of two-dimensional tandem-arranged flapping flexible foils in uniform flow," *Physics of Fluids*, vol. 32, no. 2, 2020.

[37] S. Ramananarivo, F. Fang, A. Oza, J. Zhang, and L. Ristroph, "Flow interactions lead to orderly formations of flapping wings in forward flight," *Physical Review Fluids*, vol. 1, no. 7, pp. 1–9, 2016.

[38] G. D. Xu, W. Y. Duan, and W. H. Xu, "The propulsion of two flapping foils with tandem configuration and vortex interactions," *Physics of Fluids*, vol. 29, no. 9, p. 097 102, 2017.

[39] X. Zhu, G. He, and X. Zhang, "Flow-Mediated Interactions between Two Self-Propelled Flapping Filaments in Tandem Configuration," *Physical Review Letters*, vol. 113, no. 23, pp. 1–5, 2014.

[40] G. J. Dong and X. Y. Lu, "Characteristics of flow over traveling wavy foils in a side-by-side arrangement," *Physics of Fluids*, vol. 19, no. 5, 2007.

[41] L. Kang, Z. R. Peng, H. Huang, X. Y. Lu, and W. Cui, "Active external control effect on the collective locomotion of two tandem self-propelled flapping plates," *Physics of Fluids*, vol. 33, no. 10, 2021.

[42] H. Yu, X. Y. Lu, and H. Huang, "Collective locomotion of two uncoordinated undulatory self-propelled foils," *Physics of Fluids*, vol. 33, no. 1, 2021.

[43] M. Khalid, I. Akhtar, and H. Dong, "Effect of Formation Pattern on Schooling Energetics in Fish-Like Swimming," *Journal of Fluids and Structures*, vol. 66, pp. 19–35, 2016.

[44] L. Kang, W. Cui, X. Y. Lu, and H. Huang, "Hydrodynamic force induced by vortex–body interactions in orderly formations of flapping tandem flexible plates," *Physics of Fluids*, vol. 34, no. 2, 2022.

[45] J. Deng, X. M. Shao, and Z. S. Yu, "Hydrodynamic studies on two traveling wavy foils in tandem arrangement," *Physics of Fluids*, vol. 19, no. 11, 2007.

[46] A. P. Maertens, A. Gao, and M. S. Triantafyllou, "Optimal undulatory swimming for a single fish-like body and for a pair of interacting swimmers," *Journal of Fluid Mechanics*, vol. 813, pp. 301–345, 2017.

[47] M. Saadat, F. Berlinger, A. Sheshmani, R. Nagpal, G. V. Lauder, and H. Haj-Hariri, "Hydrodynamic advantages of in-line schooling," *Bioinspiration and Biomimetics*, vol. 16, no. 4, 2021.

[48] A. U. Oza, L. Ristroph, and M. J. Shelley, "Lattices of Hydrodynamically Interacting Flapping Swimmers," *Physical Review X*, vol. 9, no. 4, p. 41 024, 2019.

[49] S. Alben, "Collective locomotion of two-dimensional lattices of flapping plates. Part 2. Lattice flows and propulsive efficiency," *Journal of Fluid Mechanics*, vol. 915, 2021.

[50] A. D. Becker, H. Masoud, J. W. Newbolt, M. Shelley, and L. Ristroph, "Hydrodynamic schooling of flapping swimmers," *Nature Communications*, vol. 6, no. May, pp. 1–8, 2015.

[51] L. Dai, G. He, X. Zhang, and X. Zhang, "Stable formations of self-propelled fishlike swimmers induced by hydrodynamic interactions," *Journal of the Royal Society Interface*, vol. 15, no. 147, 2018.

[52] Y. Pan and H. Dong, "Effects of phase difference on hydrodynamic interactions and wake patterns in high-density fish schools," *Physics of Fluids*, vol. 34, no. 111902, pp. 1–25, 2022.

[53] J. Deng and X. Shao, "Hydrodynamics in a diamond-shaped fish school," *Journal of Hydrodynamics, Ser. B*, vol. 18, pp. 438–442, 2006.

[54] S. Y. Chen, Y. H. J. Fei, Y. C. Chen, K. J. Chi, and J. T. Yang, "The swimming patterns and energy-saving mechanism revealed from three fish in a school," *Ocean Engineering*, vol. 122, pp. 22–31, 2016.

[55] X. Lin, J. Wu, T. Zhang, and L. Yang, "Self-organization of multiple self-propelling flapping foils: Energy saving and increased speed," *Journal of Fluid Mechanics*, vol. 884, pp. 1–14, 2019.

[56] Z. R. Peng, H. Huang, and X. Y. Lu, "Hydrodynamic schooling of multiple self-propelled flapping plates," *Journal of Fluid Mechanics*, vol. 853, pp. 587–600, 2018.

[57] S. G. Park and H. J. Sung, "Hydrodynamics of flexible fins propelled in tandem, diagonal, triangular and diamond configurations," *Journal of Fluid Mechanics*, vol. 840, pp. 154–189, 2018.

[58] M. Gazzola, A. A. Tchieu, D. Alexeev, A. De Brauer, and P. Koumoutsakos, "Learning to school in the presence of hydrodynamic interactions," *Journal of Fluid Mechanics*, vol. 789, pp. 726–749, 2016.

[59] A. Filella, F. Nadal, C. Sire, E. Kanso, and C. Eloy, "Model of Collective Fish Behavior with Hydrodynamic Interactions," *Physical Review Letters*, vol. 120, no. 19, 2018.

[60] H Reuter and B Breckling, "Self organization of fish schools: An object-oriented model," *Ecological Modeling*, no. 147-59, 1994.

[61] X Chang, Z Pan, and L Luo, "Community detection based on fish school effect," *IEEE Access*, vol. 10, no. 48523, 2022.

[62] B Partridge, "Internal dynamics and the interrelations of fish in schools," *Journal of Computational Physiology*, vol. 144, pp. 313–325, 1981.

[63] Y Zhang, H Ko, M Calicchia, R Ni, and G Lauder, "Collective movement of schooling fish reduces the costs of locomotion in turbulent conditions," *PLOS Biology*, vol. 22, no. 6, e3002501, 1981.

[64] M. A. Ashraf, J. Young, and J. C. Lai, "Reynolds number, thickness and camber effects on flapping airfoil propulsion," *Journal of Fluids and Structures*, vol. 27, no. 2, pp. 145–160, 2011.

[65] K. Fard, V. Ngo, D. Pence, and J. Liburdy, "Energy Harvesting Performance of Thick Oscillating Airfoils Using a Discrete Vortex Model," *Journal of Fluids Engineering*, vol. 145, no. March, pp. 1–10, 2023.

[66] Y. Wang, X. Sun, D. Huang, and Z. Zheng, "Numerical investigation on energy extraction of flapping hydrofoils with different series foil shapes," *Energy*, vol. 112, pp. 1153–1168, 2016.

[67] M. Yu, Z. J. Wang, and H. Hu, "High fidelity numerical simulation of airfoil thickness and kinematics effects on flapping airfoil propulsion," *Journal of Fluids and Structures*, vol. 42, pp. 166–186, 2013.

[68] T. Van Buren, D. Floryan, A. J. Smits, P. Han, A. T. Bode-Oke, and H. Dong, "Optimizing foil shape for efficient unsteady propulsion," *AIAA Scitech 2019 Forum*, 2019(a).

[69] P. Han, G. V. Lauder, and H. Dong, "Hydrodynamics of median-fin interactions in fish-like locomotion: Effects of fin shape and movement," *Physics of Fluids*, vol. 32, no. 1, 2020.

[70] J. Kelly, H. Pan, H. Dong, and T. Van Buren, "Wake Structures and Effect of Hydrofoil Shapes in Efficient Flapping Propulsion," *FEDSM2021-65655*, pp. 1–7, 2021.

[71] J. Kelly, Y. Pan, and H. Dong, "Body Shape Effects on the Hydrodynamic Performance of Bio-Inspired Undulating Swimmers," *FEDSM2022*, pp. 1–6, 2022.

[72] F. S. I. Borazjani, "On the role of form and kinematics on the hydrodynamics of self-propelled body/caudal fin swimming," *Journal of Experimental Biology*, vol. 213, pp. 89–107, 2010.

[73] E. Tytell, I. Borazjani, F. Sotiropoulos, T. Baker, E. Anderson, and G. Lauder, "Disentangling the functional roles of morphology and motion in the swimming of fish," *Integrative and Comparative Biology*, vol. 50, no. 6, 2010.

[74] W. V. Rees, M. Gazzola, and P. Koumoutsakos, "Optimal shapes for anguilliform swimmers at intermediate reynolds numbers," *Journal of Fluid Mechanics*, vol. 722: R3, 2013.

[75] S. Gupta, A. Agrawal, K. Hourigan, M. Thomson, and A. Sharma, "Anguilliform and carangiform fish-inspired hydrodynamic study for an undulating hydrofoil: Effect of shape and adaptive kinematics," *Physical Review Fluids*, vol. 7, no. 094102, 2022.

[76] B. Boschitsch, P. Dewey, and A. Smits, "Propulsive performance of unsteady tandem hydrofoils in an in-line configuration," *Physics of Fluids*, vol. 26, no. 051901, 2014.

[77] M. S. U. Khalid, J. Wang, H. Dong, and M. Liu, "Flow transitions and mapping for undulating swimmers," *Physical Review Fluids*, vol. 5, no. 6, p. 63 104, 2020.

[78] W. Xu, G. Xu, M. Li, and C. Yang, "Bio-inspired wake tracking and phase matching of two diagonal flapping swimmers," *Physics of Fluids*, vol. 35, no. 031902, 2023.

[79] Y. Pan, W. Zhang, J. Kelly, and H. Dong, "Unraveling hydrodynamic interactions in fish schools: A three-dimensional computational study of in-line and side-by-side configurations," *Physics of Fluids*, vol. 36, no. 081909, 2024.

[80] Y. Pan and H. Dong, "Hydrodynamic performance and wake topology of schooling fish in three-dimensional formations," *Journal of Fluids Engineering*, vol. 145, no. 060905, 2023.

[81] G. Novati, S. Verma, D. Alexeev, D. Rossinelli, W. M. Van Rees, and P. Koumoutsakos, "Synchronisation through learning for two self-propelled swimmers," *Bioinspiration and Biomimetics*, vol. 12, no. 3, 2017.

[82] X Li, J Gu, Z Su, and Z Yao, "Hydrodynamic analysis of fish schools arranged in the vertical plane," *Physics of Fluids*, vol. 33, no. 121905, 2021.

[83] A. Menzer, Y. Gong, F. E. Fish, and H. Dong, "Bio-Inspired Propulsion : Towards Understanding the Role of Pectoral Fin Kinematics in Manta-like Swimming," *Biomimetics*, vol. 7, no. 45, 2022.

[84] G Liu, Y Ren, H Dong, O Akanyeti, J Liao, and G Lauder, "Computational analysis of vortex dynamics and performance enhancement due to body–fin and fin–fin interactions in fish-like locomotion," *Journal of Fluid Mechanics*, vol. 829, pp. 65–88, 2017.

[85] J. Wang, D. K. Wainwright, R. E. Lindengren, G. V. Lauder, and H. Dong, "Tuna locomotion: A computational hydrodynamic analysis of finlet function," *Journal of the Royal Society Interface*, vol. 17, no. 165, 2020.

[86] P. Han, G. Liu, Y. Ren, and H. Dong, "Computational Analysis of 3D Fin-Fin Interaction In Fish's Steady Swimming," *FEDSM2016*, pp. 1–6, 2016.

[87] P. Han, Y. Pan, G. Liu, and H. Dong, "Propulsive performance and vortex wakes of multiple tandem foils pitching in-line," *Journal of Fluids and Structures*, vol. 108, p. 103 422, 2022.

[88] C. Li, H. Dong, and G. Liu, "Effects of a dynamic trailing-edge flap on the aerodynamic performance and flow structures in hovering flight," *Journal of Fluids and Structures*, vol. 58, pp. 49–65, 2015.

[89] M. Bozkurttas, H. Dong, V. Seshadri, R. Mittal, and F. Najjar, "Towards numerical simulation of flapping foils on fixed cartesian grids," *43rd AIAA Aerospace Sciences Meeting and Exhibit - Meeting Papers*, no. December 2014, pp. 15 801–15 809, 2005.

[90] R. Mittal, H. Dong, M. Bozkurttas, F. M. Najjar, A. Vargas, and A. von Loebbecke, "A versatile sharp interface immersed boundary method for incompressible flows with complex boundaries," *Journal of Computational Physics*, vol. 227, no. 10, pp. 4825–4852, 2008.

[91] W Zhang, Y Pan, J Wang, V. D. Santo, G Lauder, and H Dong, "An efficient tree-topological local mesh refinement on cartesian grids for multiple moving objects in incompressible flow," *Journal of Computational Physics*, vol. 479, no. 111983, 2023.

[92] P. A. Dewey, D. B. Quinn, B. M. Boschitsch, and A. J. Smits, "Propulsive performance of unsteady tandem hydrofoils in a side-by-side configuration," *Physics of Fluids*, vol. 26, no. 4, 2014.

[93] C. K. Hemelrijk, D. A. Reid, H. Hildenbrandt, and J. T. Padding, "The increased efficiency of fish swimming in a school," *Fish and Fisheries*, vol. 16, no. 3, pp. 511–521, 2015.

[94] M. Daghooghi and I. Borazjani, "The hydrodynamic advantages of synchronized swimming in a rectangular pattern," *Bioinspiration and Biomimetics*, vol. 10, no. 5, 2015.

[95] J. J. VIDELER and F. HESS, "Fast Continuous Swimming of Two Pelagic Predators, Saithe (Pollachius Virens) and Mackerel (Scomber Scombrus): a Kinematic Analysis," *Journal of Experimental Biology*, vol. 109, no. 1, pp. 209–228, 1984.

[96] J Kelly, "Hydrodynamic analysis and classification of large dense planar synchronous fish schools," *Masters Thesis*, 2022.

[97] D. B. Quinn, K. W. Moored, P. A. Dewey, and A. J. Smits, "Unsteady propulsion near a solid boundary," *Journal of Fluid Mechanics*, vol. 742, pp. 152–170, 2014.

[98] D. B. Quinn, G. V. Lauder, and A. J. Smits, "Flexible propulsors in ground effect," *Bioinspiration and Biomimetics*, vol. 9, no. 3, 2014.

[99] Y. Bao, D. Zhou, J. J. Tao, *et al.*, "Dynamic interference of two anti-phase flapping foils in side-by-side arrangement in an incompressible flow," *Physics of Fluids*, vol. 29, no. 3, 2017.

[100] V. Di Santo, E. Goerig, D. K. Wainwright, *et al.*, "Convergence of undulatory swimming kinematics across a diversity of fishes.," *Proceedings of the National Academy of Sciences of the United States of America*, vol. 118, no. 49, pp. 1–9, 2021.

[101] Y. Pan, P. Han, J. Huang, and H. Dong, "Effect of Formation Pattern on Schooling Energetics in Fish-Like Swimming," *FEDSM2020*, pp. 1–8, 2020.

[102] L Ristroph and J Zhang, "Anomalous hydrodynamic drafting of interacting flapping flags.," *Physical Review Letters*, vol. 101, no. 19, 2008.

[103] D. Lane, M. Sfakiotakis, and J. Davies, "Review of Fish Swimming Modes for Aquatic Locomotion," *IEEE Journal of Oceanic Engineering*, 1998.

[104] T. Van Buren, D. Floryan, and A. J. Smits, "Scaling and performance of simultaneously heaving and pitching foils," *AIAA Journal*, vol. 57, pp. 3666–3677, 9 2019(b).

[105] M. S. Selig, *Uiuc airfoil data site*, Urbana, Ill. :Deptartment of Aeronautical and Astronautical Engineering University of Illinois at Urbana-Champaign, 1996.

[106] D. J. Poole, C. B. Allen, and T. C. Rendall, "Metric-based mathematical derivation of efficient airfoil design variables," *AIAA Journal*, vol. 53, no. 5, pp. 1349–1361, 2015.

[107] D. A. Masters, N. J. Taylor, T. C. Rendall, C. B. Allen, and D. J. Poole, "Geometric comparison of aerofoil shape parameterization methods," *AIAA Journal*, vol. 55, no. 5, pp. 1575–1589, 2017.

[108] B. M. Kulfan and J. E. Bussoletti, ""Fundamental" parametric geometry representations for aircraft component shapes," *Collection of Technical Papers - 11th AIAA/ISSMO Multidisciplinary Analysis and Optimization Conference*, vol. 1, pp. 547–591, 2006.

[109] B. M. Kulfan, "Universal parametric geometry representation method," *Journal of Aircraft*, vol. 45, no. 1, pp. 142–158, 2008.

[110] P. Han, A. T. Bode-Oke, H. Dong, T. Van Buren, D. Floryan, and A. J. Smits, "Comparison of Geometric Parameterization Methods for Optimal Shape Design in Efficient Flapping Propulsion," *AIAA AVIATION Forum*, no. June, pp. 1–8, 2019.

[111] Graham K. Taylor, Robert L. Nudds, and Adrian L. R. Thomas, "Flying and swimming animals cruise at a Strouhal number tuned for high power efficiency," *Nature*, vol. 425, no. 6959, pp. 705–707, 2003.

[112] H. Dong, A. T. Bode-Oke, and C. Li, "Learning from Nature: Unsteady Flow Physics in Bioinspired Flapping Flight," *Flight Physics-Models, Techniques and Technologies, IntechOpen.*, pp. 1–18, 2018.

[113] J. M. Anderson, K. Streitlien, D. S. Barrett, and M. S. Triantafyllou, "Oscillating foils of high propulsive efficiency," *Journal of Fluid Mechanics*, vol. 360, pp. 41–72, 1998.

[114] Z. C. Zheng and Z. Wei, "Study of mechanisms and factors that influence the formation of vortical wake of a heaving airfoil," *Physics of Fluids*, vol. 24, no. 10, 2012.

[115] D. J. Cleaver, Z. Wang, and I. Gursul, "Bifurcating flows of plunging aerofoils at high Strouhal numbers," *Journal of Fluid Mechanics*, vol. 708, pp. 349–376, 2012.

[116] J. Deng, L. Sun, Lubao Teng, D. Pan, and X. Shao, "The correlation between wake transition and propulsive efficiency of a flapping foil: A numerical study," *Physics of Fluids*, vol. 28, no. 9, 2016.

[117] R. Gopalkrishnan, M. S. Triantafyllou, G. S. Triantafyllou, and D. Barrett, "Active vorticity control in a shear flow using a flapping foil," *Journal of Fluid Mechanics*, vol. 274, pp. 1–21, 1994.

[118] J Guo, W Zhang, P Han, F Fish, and H Dong, "Thrust generation and propulsive efficiency in dolphin-like swimming propulsion," *Bioinspiration and Biomimetics*, vol. 18, no. 056001, 2023.

[119] Z. Liu, K. S. Bhattacharjee, F. B. Tian, J. Young, T. Ray, and J. C. Lai, "Kinematic optimization of a flapping foil power generator using a multi-fidelity evolutionary algorithm," *Renewable Energy*, vol. 132, pp. 543–557, 2019.

[120] J Wang, H Tran, M Christino, *et al.*, "An image-guided computational approach to inversely determine in vivo material properties and model flow-structure interactions of fish fins," *AJK Fluids*, no. 5472, 2019.

[121] G Liu, Y Ren, J Zhu, H Bart-Smith, and H Dong, "Thrust producing mechanisms in ray-inspired underwater vehicle propulsion," *Theoretical and Applied Mechanics Letters*, vol. 5, pp. 54–57, 2015.

[122] J. Hunt, A. Wray, and P. Moin, "Eddies, streams, and convergence zones in turbulent flows, studying turbulence using numerical simulation databases," *Center for Turbulence Research Proceedings of the 1988 summer program*, no. 073101, pp. 193–208, 1988.

[123] J Zhan, Y Li, W Wai, and W Hu, "Comparison between the q criterion and rortex in the application of an in-stream structure," *Physics of Fluids*, vol. 31, no. 121701, 2019.

[124] J Guo, P Han, W Zhang, *et al.*, "Vortex dynamics and fin-fin interactions resulting in performance enhancement in fish-like propulsion," *Physical Review Fluids*, vol. 8, no. 073101, 2023.

[125] J. Kelly, M. S. U. Khalid, P. Han, and H. Dong, "Geometric characteristics of flapping foils for enhanced propulsive efficiency," *Journal of Fluids Engineering*, vol. 145, no. 061104, 2023.

[126] K. Lucas, G. Lauder, and E. Tytell, "Airfoil-like mechanics generate thrust on the anterior body of swimming fishes," *PNAS*, vol. 19, no. 117, pp. 10 585–10 592, 2020.

[127] J. Gray, *Florida Museum of Natural History*, 2022, Morphosource.

[128] J. Gray, *Florida Museum of Natural History*, 2023, Morphosource.

[129] S. Nguyen, *Stacy Nguyen*, 2021, Morphosource.

[130] B. Frable, *University of California-San Diego Scripps Inst of Oceanography*, 2022, Morphosource.

[131] S. Ruiz-Escobar, *Florida Museum of Natural History*, 2022, Morphosource.

[132] B. Ray, *Florida Museum of Natural History*, 2019, Morphosource.

[133] J. Gardner, *University of Washington Fish Collection*, 2019, Morphosource.

[134] M. Shepard, *University of Kansas Biodiversity Institute Ichthyology Collection*, 2022, Morphosource.

[135] G. Somarriba, *Florida Museum of Natural History*, 2019, Morphosource.

[136] G. Somarriba, *Florida Museum of Natural History*, 2019, Morphosource.

[137] E. Stanley, *Florida Museum of Natural History*, 2018, Morphosource.

[138] E. Stanley, *Florida Museum of Natural History*, 2018, Morphosource.

[139] Z. Randall, *Yale University*, 2020, Morphosource.

[140] J Nauen and G Lauder, "Hydrodynamics of caudal fin locomotion by chub mackerel, scomber japonicus (scombridae)," *Journal of Experimental Biology*, vol. 205, no. 12, pp. 1709–1724, 2002.